

# Mathematical modelling of membrane separation

**Vinther, Frank**

*Publication date:*
2015

*Document Version*
Publisher's PDF, also known as Version of record

# Mathematical modelling of membrane separation

Frank Vinther

Supervisor: Morten Brøns

Co-supervisor: Anne S. Meyer

Kongens Lyngby 2013
DTU-Compute-PHD-2013-320

Technical University of Denmark
Compute
Building 303, DK-2800 Kongens Lyngby, Denmark
Phone +45 45253031, Fax +45 45881399
reception@compute.dtu.dk
www.compute.dtu.dk

DTU-Compute-PHD: ISSN 0909-3192

# Summary

This thesis concerns mathematical modelling of membrane separation. The thesis consists of introductory theory on membrane separation, equations of motion, and properties of dextran, which will be the solute species throughout the thesis. Furthermore, the thesis consist of three separate mathematical models, each with a different approach to membrane separation.

The first model is a statistical model investigating the interplay between solute shape and the probability of entering the membrane. More specific the transition of solute particles from being spherical to becoming more elongated as prolate ellipsoids with the same volume. The porous membrane is assumed isotropic such that the model reduces to a two dimensional model. With this assumption ellipsoids with the same volume reduces to ellipses with the same area. The model finds the probability of entering the pore of the membrane. It is found that the probability of entering the pore is highest when the largest of the radii in the ellipse is equal to half the radius of the pore, in case of molecules with circular radius less than the pore radius. The results are directly related to the macroscopic distribution coefficient and the rejection coefficient.

The second model is a stationary model for the flux of solvent and solute in a hollow fibre membrane. In the model we solve the time independent equations for transport of solvent and solute within the hollow fibre. Furthermore, the flux of solute and solvent through the membrane is coupled through the boundary conditions. The model investigates how the true and observed rejection coefficient depends on the transmembrane pressure, the average inlet velocity, and the molecular weight. Furthermore, the effect of concentration dependent viscosity on the rejection coefficients is investigated. The results show that the true rejection

coefficient is increasing as a function of increasing transmembrane pressure, increasing inlet velocity, and decreasing molecular weight. Furthermore, it is found that a concentration dependent viscosity decreases the true rejection. The observed rejection is increasing for decreasing molecular weight and increasing inlet velocities. The observed rejection can be either increasing or decreasing as a function of increasing transmembrane pressure. Moreover, the observed rejection is reduced when the viscosity depends on the concentration.

The study is a time dependent model of back-shocking. During back-shocking the pressure difference across the membrane is reversed for a given time. This implies that the concentration polarization at the membrane surface is flushed away. When the pressure is reversed back to normal the membrane performs better resulting in an increased average flux. Two models models of the problem was made.

In a two dimensional model, limited to capture the dynamics close to the membrane, a positive effect was observed on both the observed rejection and the average solvent flux. Furthermore, an analytical upper estimate for the optimal back-shock time is given. In a three dimensional model, where the flow within the entire hollow fibre is modelled, the mentioned upper estimate is used to obtain a positive effect on both the observed rejection and the average solvent flux. Moreover, the effect of a concentration dependent viscosity was investigated. It was found that the average flux compared to the steady-state solution increased when the viscosity depends on the concentration.

# Resumé

Denne afhandling omhandler matematisk modellering af membranseparation. Afhandlingen består af indledende teori omhandlende membranseparation, ligninger fra fluiddynamik og egenskaber for dextran, som er det stof der ønskes separeret. Ydermere består den af tre separate matematiske modeller, med hver deres tilgang til membranseparation.

Den første model er en statistisk model, som undersøger sammenhængen mellem molekyleform og sandsynligheden for at det givne molekyle penetrerer ind i membranen. Mere specifikt modelleres molekylers overgang fra sfæriske til aflange af form som prolate ellipsoider med samme rumfang. Den porøse membran overflade tænkes at være isotrop, hvorved modellen reduceres til et to dimensionelt problem med ellipser med samme areal frem for ellipsoider med samme rumfang. I modellen findes det at sandsynligheden for at penetrere membranen er størst når den største af radierne er lig halvdelen af poreradius, for molekyler med mindre cirkuler radius end poreradius. Disse resultater relateres direkte til absorbtionskoefficienten og sekundært til tilbageholdelseskoefficienten.

Anden model er en stationær model for fluxen af solvent og solut i en hul fiber membran. I modellen løses de stationære ligninger for solventets og solutets bevægelse igennem den hule fiber, samtidig med at fluxen igennem membranen beskrives ved randbetingelserne. I modellen undersøges det, hvorledes både den sande og den observerede tilbageholdelseskoefficient afhænger af det transmembrane tryk, den gennemsnitlige indløbshastighed, molekyle størrelsen, samt en undersøgelse af hvorledes disse koefficienter ændrer sig når væskens viskocitet afhænger af koncentrationen. Resultaterne viser at den sande tilbageholdelseskoefficient er stigende med stigende transmembrant tryk, stigende indløbshastighed og faldende molekylestørrelse. Ydermere vil en koncentra-

tionsafhængig viskocitet sænke den sande tilbageholdelse. Den observerede tilbageholdelse er stigende for faldende molekylestørrelser og stigende indløbshastighed. Den observerede tilbageholdelse kan være både stigende og aftagende som funktion af det transmembrane tryk. Ydermere reduceres den observerede tilbageholdelse når viskociteten er afhængig af koncentrationen.

Den sidste model er en tidsafhængig model af tilbagetryk (back-shocking). Under denne proces vendes trykforskellen over membranen i en given tid, hvorved grænselaget ved membranoverfladen skylles væk. Herefter vendes trykket igen med det resultat at en højere gennemsnitsflux opnås over en periode. To forskellige modeller er lavet over problemet.

I den to dimensionale model, der afgrænser sig til at se på dynamikken i grænselaget, opnås en positiv effekt for både den gennemsnitlige solvent flux og den observerede tilbageholdelse. Ydermere opstilles analytisk en øvre grænse for tilbagetrykstiden, der optimerer gennemsnitsfluxen. Dette udtryk afhænger af de operative paramtre benyttet i en sådan proces. I den tre-dimensionelle model, hvor hele strømningen i den hule fiber modelleres og antages at være aksesymmetrisk, benyttes netop det førnævnte overslag til at opnå positiv effekt for både den gennemnitlige flux og den observerede tilbage holdelse. Ydermere tillades det viskociteten at afhænge af koncentrationen, hvorved effekten på både den gennemsnitlige flux og den observerede tilbageholdelse forøges.

# Preface

This thesis has been done from April 2010 to ultimo November 2013. The work was supported by:
The Danish Council for Independent Research, Technology and Production Sciences
The Technical University of Denmark:
-Department of Chemical Engineering
-Department of Applied Mathematics and Computer Science.

I would like to thank Kerry Hourigan for hosting me during my six months stay at the Department of Mechanical Engineering, Monash University, Melbourne, Australia.

A special thanks to my supervisor Professor Morten Brøns, without whom this thesis would not have been.
Also, I would like to thank, Manuel Pinelo, Gunnar Jonsson, and Anne S. Meyer, for talks on almost every subject in the thesis. These three have given me an understanding of 'the art of membrane separation' that I could not have obtained on my own.

Furthermore, I would like to thank Mads Peter Sørensen for discussions on different mathematical topics that have been used in the thesis.

# Papers included in the thesis

[3] Frank Vinther, Manuel Pinelo, Morten Brøns, Gunnar Jonsson Anne S. Meyer. Statistical modelling of the interplay between solute shape and rejection in porous membranes. *Separation and Purification Technology* , 89, 261-269, 2012.

[4] Frank Vinther, Manuel Pinelo, Morten Brøns, Gunnar Jonsson Anne S. Meyer. Mathematical modelling of dextran filtration through hollow fibre membranes. *Separation and Purification Technology*, 2013. Under revision.

# Contents

Chapter 1

# Introduction

Membrane separation is a process where a solution is forced through a membrane by a driving force. The membrane divides two distinct domains known as the retentate and the permeate side of the membrane. The feed solution enters on the retentate side of the membrane and the driving force forces part of the solution through the membrane and into the permeate. Membrane separation, however, differ in various ways and can be subdivided in many ways.

Firstly, a subdivision depending on the phase of the retentate and the permeate. In gas separation the phase in the retentate and the permeate is in a gaseous state. In pervaporation the solution on the retentate side is in a liquid state, whereas the solution on the permeate is in a gaseous state. Other processes have liquid state on both the retentate and the permeate side of the membrane [45].

Secondly, a subdivision can be made depending of the driving force. In dialysis the driving force is the concentration gradient across the membrane. In electrodialysis the driving force is the gradient in electrical potential. In other processes the driving force is the pressure gradient [45].

The focus in this thesis will be processes with a liquid state on both sides of the membrane and a pressure gradient as the driving force.

These processes can be further subdivided depending on the characteristics of

the membrane. The membrane can be considered as a dense material with pores going through it. The subdivision is usually done by looking at the pore diameter of the membrane.

In conventional filtration the pore diameter is roughly in the interval 10-100 $\mu$m, for microfiltration the pore diameter lies roughly in interval 1000 Å-10 $\mu$m, in ultrafiltration the pore diameter lies roughly in the interval 30 Å- 1000 Å, for pore diameters smaller that 30 Å, the process is termed reverse osmosis[15]. It should, however, be noted that for reverse osmosis the membrane is so dense that speaking of pores makes little sense.

The feed solution, entering the retentate side, is a solvent containing one or more solute species. The membrane is capable of retaining some of the solute species which is essentially how the separation takes place. The pore diameter that subdivide the membrane processes can also be made in terms of solute molecules, since the membrane is capable of retaining molecules of size that is comparable to the pore diameter. Hence, microfiltration is used for separation of larger solutes such as yeast. Whereas reverse osmosis is used for smaller solutes such as in desalination.

The focus of this thesis will be on ultrafiltration. The characteristics of solute and solvent transport through the membrane will be elaborated in the following section

## 1.1 Models of flux through the membrane

Mathematical models used for better understanding membrane separation has been of interest since the very beginning of membrane separation.

The models that describe the flux through the membrane differ as the membrane considered changes from being very dense to becoming more porous.

Although there is an overlap the models used for very porous membranes are called pore flow models, whereas the models are used for very dense membranes are called diffusion models.

The simplest interpretation of the flux through membranes are the pore flow models. In the simplest pore flow description the solute particles are all circular and the pores go through the membrane as straight cylinders. Assuming that the solute particles all have the same radius $R_s$ and assuming different pore radii, $r_i$, the flux of solvent $J_v$ and the flux of suloute $J_s$, through the membrane

is given by Poiseuille's equation [26]. Hence,

$$J_v = k_1 \Delta p + k_2 \Delta p \tag{1.1}$$

$$J_s = k_2 c_m J_v \,, \tag{1.2}$$

where $c_m$ is the concentration on the membrane surface and $k_1$ and $k_2$ is defined below. Since the transport through the membrane is directly proportional to pore area on the membrane surface

$$k_1 + k_2 = \sum_i \frac{\epsilon r_i^2}{8\eta \Delta x} \,, \tag{1.3}$$

where $\eta$ is the viscosity, $\Delta x$ is the thickness of the membrane and $\epsilon$ is the fractional pore area. The solute flux only happens through pores larger than the size of the molecule. Hence, $k_2$ is given by

$$k_2 = \sum_{j, r_j > R} \frac{\epsilon r_i^2}{8\eta \Delta x} \,. \tag{1.4}$$

In chapter 3 a statistical model is presented that relates the shape of the molecule to the probability of entering the pores. Surely, pore flow models with a higher degree of complexity than presented here are available. Information on pore flow models is widely found in the literature, see e.g. [9, 12, 25, 37, 39, 55, 61, 26].

In the models that assume diffusion through the membrane there are different approaches, the most widely used is the the approach of irreversible thermodynamics. Information on irreversible thermodynamics can be found in [6, 4, 5]. Among the models explaining the transport through the membrane using irreversible thermodynamics we mention the famous Spiegler-Kedem model [58] and others [29, 24, 28]. This approach have been used for mathematical modelling determination of intrinsic membrane characteristics, see e.g. [1, 13, 21]. In the Spiegler-Kedem model the following expression is derived for the flux through the membrane

$$J_v = L_p \left( \Delta p - \sigma \Delta \pi \right) \,, \tag{1.5}$$

$$J_s = \omega \Delta c + (1 - \sigma) \bar{c} J_v \,. \tag{1.6}$$

Here, $J_v$ is the solvent flux, $J_s$ is the solute flux, $L_p$ is the pure solvent permeability, $\Delta p$ is pressure difference across the membrane, $\Delta \pi$ is the difference in osmotic pressure, $\bar{c}$ is the average concentration on both sides of the membrane, $\omega$ is the solute permeability coefficient, and $\sigma$ is the reflection coefficient. In [26] it has been shown that in the case where $\sigma \approx 0$ the expressions for the flux in equation (1.6) reduces to the expression for pore flow models. In the other

limit $\sigma \to 1$ the model reduce to the solution diffusion model used for very dense membranes [63]. I.e.,

$$J_v = A(\Delta p - \Delta \pi)\,, \tag{1.7}$$
$$J_v = B\Delta c\,. \tag{1.8}$$

In a given membrane process the flux through the membrane is often a measure for the efficiency. There are, however, other measures for efficiency. Among these are the rejection coefficients. The true, or intrinsic, rejection is a measure of the membranes ability to retain solute particles and is defined as

$$R_{true} = \left(1 - \frac{c_p}{c_m}\right) 100\%\,, \tag{1.9}$$

where $c_p$ is the concentration on the permeate side of the membrane, and $c_m$ is the concentration on the permeate side of the membrane. Hence, a high true rejection corresponds to a membrane that is good at retaining the solute.

Another measure that will be widely used in the thesis is the observed rejection, defined as

$$R_{obs} = \left(1 - \frac{c_p}{c_b}\right) 100\%\,, \tag{1.10}$$

where $c_b$ is the bulk concentration. Whereas the true rejection is a measure on the membrane the observed rejection is a measure of the process as a whole. Although the two rejection coefficients are the same in the limits, i.e., if one is zero so is the other, part of this thesis will concern how one can observed rejection vary while the true rejection is nearly constant.

## 1.2 Flux decline in ultrafiltration

As a given membrane process is used a flux decline is observed as a function of time. The causes can be subdivided into two distinct categories; internal fouling and concentration polarization.

Internal fouling covers pore blocking, adsorption and deposition of solidified solutes on the membrane surface. This type of fouling decreases the flux as a function of time and is usually considered more or less irreversible.

Concentration polarization is the build up of solute on the membrane surface. This also decreases the flux over time, but is considered a reversible process.

The build up of concentration on the membrane surface can be described either according to the cake theory or the thin film theory [62].

In the cake theory a constant concentration on the membrane surface as assumed. The width of the cake layer grows as a function of increasing permeate volume. The cake layer adds an additional resistance to the flux through the membrane. Hence, as the cake layer grows the flux through the membrane decreases.

The models build upon the thin film theory all start with the continuity equation for the solute

$$\boldsymbol{v} \cdot \nabla c = D\nabla^2 c\,. \tag{1.11}$$

The continuity equation will be derived in section 1.4.1. When looking only at the direction normal to the membrane surface (let this be the $x$-direction) one gets

$$v_x \frac{dc}{dx} - D\frac{d^2c}{dx^2} = 0\,. \tag{1.12}$$

When steady state is reached the velocity component perpendicular to the membrane surface will be constant and equal to the volumetric flux, $J$, through the membrane. Hence,

$$\frac{d}{dx}\left(Jc - D\frac{dc}{dx}\right) = 0\,. \tag{1.13}$$

Or

$$Jc - D\frac{dc}{dx} = const \tag{1.14}$$

A boundary condition for the solute flux is

$$Jc_m - D\left.\frac{dc}{dx}\right|_0 = Jc_p\,. \tag{1.15}$$

Hence, a differential equation from equation (1.14) is obtained

$$Jc - D\frac{dc}{dx} = Jc_p\,. \tag{1.16}$$

Or

$$\frac{d}{dx}\ln\left(c - c_p\right) = \frac{J}{D}\,. \tag{1.17}$$

Integrating equation (1.17) from $-\delta$ to 0 with the boundary conditions $c(-\delta) = c_b$ and $c(0) = c_m$ gives

$$\ln\left(\frac{c_m - c_p}{c_b - c_p}\right) = \frac{J}{D}\delta = \frac{J}{k}\,, \tag{1.18}$$

where $k$ is the mass transfer coefficient, $k = {}^{D}/_{\delta}$. The solution is illustrated in figure 1.1.

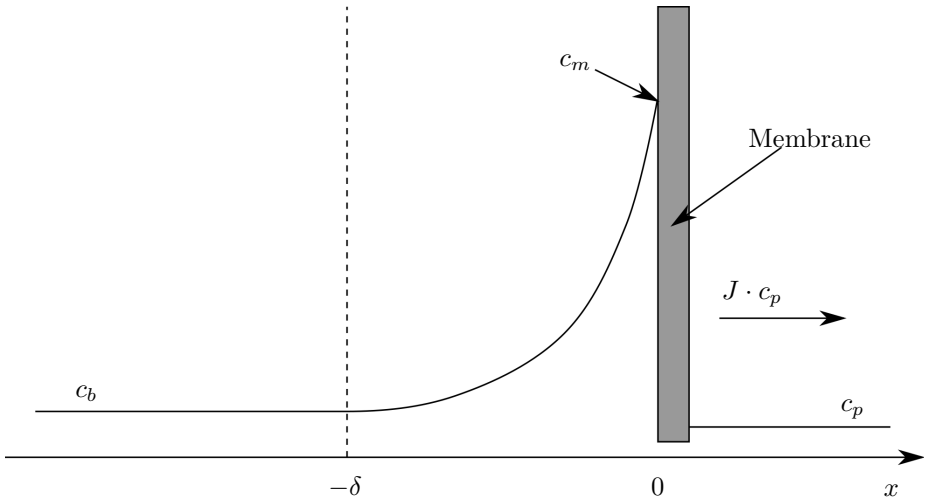


Figure 1.1: Illustration of concentration polarization

Therefore, the mass transfer coefficient is a measure of the back diffusion and the boundary layer thickness. At a constant volumetric flux, a large value of $k$ means that either the back diffusion is large or the boundary layer thickness is small. Hence, concentration polarization will be a minor problem in a mixture with large diffusion constants, compared to a mixture with small diffusion constants.

Three dominant mathematical models exist to describe the flux decline during concentration polarization. These will briefly be explained below.

Firstly, there is the resistance models. Here the flux is described as the driving force divided by the total resistance times the viscosity. I.e.,

$$J_v = \frac{\Delta p}{\eta R_{total}} \tag{1.19}$$

The total resistance is then the sum of of the membrane resistance and the resistance of the boundary layer. As the boundary layer offers an additional resistance $R_{total}$ increases with time and as a result the flux decreases.

$$J_v = \frac{\Delta p}{\eta \left(R_{bl} + R_m\right)} \tag{1.20}$$

Secondly, there are gel polarization models. Here the concentration builds up on the membrane until a certain concentration called the gel concentration. When the gel concentration is reached a gel layer builds up with constant concentration

$c_g$. The reduction in flux can now be explained by the resistance of the membrane and the resistance of the gel layer[46].

$$J_v = \frac{\Delta p}{\eta \left(R_g + R_m\right)} \tag{1.21}$$

Thirdly, there is the osmotic pressure models which will be used throughout the thesis. As seen from equation (1.6) the solvent flux is decreasing when the osmotic pressure is increasing. In the next section it is shown how the osmotic pressure can be expressed through the solute concentration at membrane surface. Hence, an increase in solute concentration at the membrane surface will cause a decrease in solvent flux and an increase in solute. Thus, reducing the efficiency of the membrane.

### 1.2.1 Osmotic pressure

Consider a semipermeable membrane permeable to solvent but partially impermeable to solute. In order for the two sides of the membrane to be in equilibrium one considers the equilibrium of the chemical potential between the two solutions, that is

$$\mu(P_1, T_1) = \mu(P_2, T_2)\,, \tag{1.22}$$

where subscripts 1 and 2 denote the feed side and the permeate side of the membrane respectively. Assuming that the temperature on both sides of the membrane is the same this reduces to

$$\mu(P_1, T) = \mu(P_2, T)\,. \tag{1.23}$$

In order for the solution to be in equilibrium across the membrane the chemical potential of the solvent needs to be in equilibrium. The chemical potential of the solvent is given by [35]

$$\mu(P, T) = \mu_0(P, T) - k_B T c_s\,. \tag{1.24}$$

Thus it is needed that

$$\mu_0(P_1, T) - k_B T c_{s,1} = \mu_0(P_2, T) - k_B T c_{s,2} \tag{1.25}$$

Assuming that the pressure difference is not too large a first order Taylor-expansion of $\mu_0(P_2, T)$ gives

$$\mu_0(P_2, T) = \mu_0(P_1, T) + \frac{\partial \mu_0}{\partial P} \Delta P\,. \tag{1.26}$$

Combining equation (1.25) and equation (1.26) one gets

$$\frac{\partial \mu_0}{\partial P} \Delta P = k_B T \Delta c_s \,. \tag{1.27}$$

Now $\Delta P$ is the osmotic pressure usually denoted by $\Delta\pi$ and $\partial\mu_0/\partial P$ is the molecular volume of pure solvent, $v$. Therefore we end up with an expression of the osmotic pressure as a function of the concentration difference of solute across the membrane, that is

$$\Delta\pi = \frac{k_B T}{v} \Delta c_s = RT \Delta c_s \,. \tag{1.28}$$

### 1.2.2 Virial expression of the osmotic pressure

It has, however, been proposed that the solute concentration at the membrane surface is so high, that a virial expression for the osmotic pressure would be a better approximation than the one written above [27].

Let us consider the pressure difference across the membrane to be caused by the concentration difference in solute across the membrane.

Let us further assume that the pressure in the bulk solution caused by the solute molecules is given by ideal gas law

$$P_{s,b} = \frac{n_{s,b} RT}{V} = RT c_{s,b} \,, \tag{1.29}$$

where subscript $b$ denotes that we are looking at the bulk solution. The osmotic pressure is then the difference in pressure across the membrane caused by the difference in solute concentration. Letting subscript $f$ denote that we are looking at the filtered solution, we get

$$\Delta\pi = P_{s,f} - P_{s,b} \,. \tag{1.30}$$

If we again assume that we can express the pressure on the filtered side of the membrane by a Taylor-expansion in $c_s$, we get an approximation to the order $K$

$$P_{s,f} = P_{s,b} + \sum_{k=1}^{K} \frac{1}{k!} \frac{\partial^k P}{\partial c^k} \left(\Delta c_s\right)^k \,. \tag{1.31}$$

Inserting this into equation (1.30) we get that

$$\Delta\pi = RT \Delta c_s + \sum_{k=2}^{k} \frac{1}{k!} \frac{\partial^k P}{\partial c^k} \left(\Delta c_s\right)^k \,. \tag{1.32}$$

Notice that to first order equation (1.28) and equation (1.32) are identical.

An expression of this form is presented in section 2.3 for the osmotic pressure of dextran.

## 1.3 Techniques to avoid concentration polarization

There exist techniques to reduce concentration polarization. Of these the present thesis investigate cross flow and back-flushing.

- Cross flow is widely used in membrane separation, see e.g. [22, 64, 65]. The main reason for this is the ability to reduce the concentration polarization. This is done in two ways. The first and most important is that the fluid as a whole is moving tangential to the membrane. This implies that there will be a tangential velocity component very close to the membrane. The tangential velocity component will contribute to the convection in such a way that it pushes the boundary layer towards the outlet of the membrane. However, the diffusion will have a component towards the inlet because of the gradient in concentration tangential to the membrane. Therefore, it is not clear how large a effect there is extremely close to the membrane surface. The second reason for its efficiency is that the feed solution is continuously been refreshed. Hence, compared to dead end filtration one does not have a concentration polarization growing in time.

- Back-shocking[1] is also a technique that has been used extensively, see e.g. [57, 59, 20, 17, 54, 11]. Back-shocking is a technique that most certainly changes the concentration at the membrane surface. In normal filtration a constant pressure difference is applied across the membrane, this lead to a pressure gradient with a time independent direction. When back-shocking is used the pressure is changed at a given frequency, amplitude and time interval. This leads to a change in the direction of the pressure gradient such that permeate flows from the permeate into the retentate.

  On the retentate side this process instantly changes the boundary layer close to the membrane. This is in such a way that the concentration at the membrane surface is comparable with the concentration in the permeate. After a short time interval the pressure gradient is changed back into

[1] Back-shocking, back-pulsing, back-flushing, or flow reversal essentially covers the same process. It is, however, common to refer to back-pulsing and back-shocking as shorter periods of flow reversal, as compared to back-flushing.

the original direction and separation proceeds. So this method removes the concentration polarization when the pressure is reversed. When the pressure is changed back to normal the concentration polarization will develop again. However, even with the cost of injection of permeate into the feed stream, the efficiency of the separation process is enhanced.

As explained there are many different things that can reduce the performance of a given membrane, e.g. pore blocking, etc. [62]. The overall decrease in membrane efficiency as a function of time is most probably an effect of all fouling types combined. Nevertheless, in chapter 4 a mathematical model of the interplay between physical properties of the solute and the effect of crossflow will be modelled. In chapter 5 the effect of back-shocking will be modelled. In both chapters, the equations of motion of the fluid will be solved numerically on the retentate side of the membrane, and the osmotic pressure will determine the flux decline. Therefore, we proceed to explain the equations of motion for the solute and the solvent.

## 1.4 The equations of motion in a fluid

The equation of motion of a fluid is well known and is denoted the Navier-Stokes equation. A thorough derivation of the equation can be found in any standard textbook on fluid dynamics (see e.g., [8, 34, 19],Gersten). An in-depth derivation is beyond the scope of this thesis. It will, however, be presented here along with the continuity equation for a fluid containing solute particles.

The Navier-Stokes equation is essentially Newtons second law on an infinitely small fluid parcel. In the case of an incompressible fluid, as considered in this thesis, the Navier-Stokes equation in vector notation is given by

$$\rho \frac{\partial \boldsymbol{v}}{\partial t} + \rho \boldsymbol{v} \cdot \nabla \boldsymbol{v} = -\nabla p + \eta \nabla^2 \boldsymbol{v}\,, \tag{1.33}$$

where $\boldsymbol{v}$ is the velocity vector, $p$ is the pressure $\rho$ is the density of the fluid parcel and $\eta$ is the shear viscosity. Here the left hand side of the equation represents the mass times the acceleration and the right hand side represents the forces acting on the fluid parcel.

To indicate that it is newtons second law the equation is sometimes written as

$$\rho \frac{D\boldsymbol{v}}{Dt} = \nabla \cdot \boldsymbol{\Pi}\,, \tag{1.34}$$

where

$$\frac{DX}{Dt} = \frac{\partial X}{\partial t} + \boldsymbol{v} \cdot X \,, \tag{1.35}$$

is the material derivative of any variable $X$ and $\boldsymbol{\Pi}$ is the total stress tensor

$$\boldsymbol{\Pi} = p\boldsymbol{I} + \eta \left( \nabla \boldsymbol{v} + (\nabla \boldsymbol{v})^T \right) . \tag{1.36}$$

Here $\boldsymbol{I}$ is the identity matrix. This is the definition of a Newtonian fluid.

The change of mass into a given fixed volume $V$ can be written as

$$\frac{d}{dt} \int_V \rho dV = - \int_S (\boldsymbol{n} \cdot \rho \boldsymbol{v}) dS \tag{1.37}$$

which indicates that the mass of a given volume changes according to the mass flux into the volume. Using Gauss's divergence theorem this can be rewritten as

$$\frac{d}{dt} \int_V \rho dV = - \int_V \nabla \cdot (\rho \boldsymbol{v}) dV \,. \tag{1.38}$$

Differentiating under the integral, and since the volume was chosen arbitrary we have

$$\frac{\partial \rho}{\partial t} + \nabla \cdot (\rho \boldsymbol{v}) \,, \tag{1.39}$$

which is the continuity equation for the fluid. In case the density is constant

$$\nabla \cdot \boldsymbol{v} = 0 \,. \tag{1.40}$$

### 1.4.1 Continuity equation for the solute

In absence of diffusion the concentration of each fluid element remains unchanged this means that

$$\frac{dc}{dt} = \frac{\partial c}{\partial t} + \boldsymbol{v} \cdot \nabla c = 0 \,. \tag{1.41}$$

Combining equation (1.39) and equation (1.41) one gets

$$\begin{aligned} 0 &= c \left( \frac{\partial \rho}{\partial t} + \nabla \cdot (\rho \boldsymbol{v}) \right) + \rho \left( \frac{\partial c}{\partial t} + \boldsymbol{v} \cdot \nabla c \right) \Leftrightarrow \\ 0 &= c \frac{\partial \rho}{\partial t} + \rho \frac{\partial c}{\partial t} + c \nabla \cdot (\rho \boldsymbol{v}) + \rho \boldsymbol{v} \cdot \nabla c \Leftrightarrow \\ 0 &= \frac{\partial (c\rho)}{\partial t} + \nabla \cdot (c \rho \boldsymbol{v}) \,. \end{aligned} \tag{1.42}$$

Here equation (1.42) is a continuity equation of one of the components of the mixture. In integral form equation (1.42) can be written as

$$\frac{\partial}{\partial t}\int_V \rho c dV = -\int_S (\boldsymbol{n}\cdot\rho c\boldsymbol{v})\cdot dS\,. \tag{1.43}$$

Similar as in equation 1.37 it shows that the rate of change of that component in any given volume element is equal to the amount of that component transported through the surface of the volume by the movement of the fluid.

When diffusion is taken into account an additional term accounting for the flux that occurs from the diffusion must be included in equation (1.43). Denoting the density of the diffusion flux by $\boldsymbol{i}$, i.e., $\boldsymbol{i}$ denotes the amount of the component transported through unit area in unit time, one get

$$\frac{\partial}{\partial t}\int_V \rho c dV = -\int_S \rho c\boldsymbol{v}\cdot\boldsymbol{dS} - \int_S \boldsymbol{i}\cdot\boldsymbol{dS}\,, \tag{1.44}$$

or in differential form

$$\frac{\partial c\rho}{\partial t} = -\nabla\cdot(c\rho\boldsymbol{v}) - \nabla\cdot\boldsymbol{i}\,. \tag{1.45}$$

Equation (1.45) can be written as

$$\begin{aligned} -\nabla\boldsymbol{i} &= c\frac{\partial\rho}{\partial t} + \rho\frac{\partial c}{\partial t} + \rho\boldsymbol{v}\cdot\nabla c + c\nabla\cdot(\rho\boldsymbol{v}) \Leftrightarrow \\ -\nabla\boldsymbol{i} &= c\left(\frac{\partial\rho}{\partial t} + \nabla\cdot(\rho\boldsymbol{v})\right) + \rho\left(\frac{\partial c}{\partial t} + \boldsymbol{v}\cdot\nabla c\right)\,, \end{aligned} \tag{1.46}$$

using equation (1.42) one gets another continuity equation in the form of

$$\rho\left(\frac{\partial c}{\partial t} + \boldsymbol{v}\cdot\nabla c\right) = -\nabla\boldsymbol{i}\,. \tag{1.47}$$

Neglecting thermal diffusion and barodiffusion $\boldsymbol{i} = -\rho D\nabla c$ where $D$ is the diffusion coefficient[34]. Thus equation (1.47) can be written as

$$\frac{\partial c}{\partial t} + \boldsymbol{v}\cdot\nabla c = \nabla\cdot(D\nabla c)\,. \tag{1.48}$$

If the diffusion coefficient is independent of the coordinates, equation (1.48) reduces to

$$\frac{\partial c}{\partial t} + \boldsymbol{v}\cdot\nabla c = D\nabla\cdot\nabla c \tag{1.49}$$

The continuity equation for the solute, equation (1.49), the continuity equation for the solvent 1.40, and the Navier-Stokes equation, equation (1.33), along

with appropriate boundary conditions, are essentially the equations that solve the movement of the fluid and the transport of the solute particles in the bulk solution.

These are often made non dimensional by scaling the equations. This can be found in appendix A.

Chapter 2

# Physical properties of dextran

in the mathematical models presented in chapter 4 and chapter 5 the Navier-Stokes equation is solved along with the continuity equation for both solvent and solute.

As seen from equation equation (1.33) the viscosity enters the momentum equation. Furthermore, as seen in equation equation (1.49) the diffusion coefficient enters in the continuity equation for the solute.

In the models presented in chapter 4 and chapter 5 the viscosity will be allowed to depend on the concentration. Therefore, the expressions for this dependency and the data found in the literature is presented in section 2.1.

## 2.1 Viscosity

The viscosity enters the Navier-Stokes equation and determines the fluids resistance to shearing. Hence, for high viscosities a larger force is needed to shear the fluid. It is well known that the viscosity depends on the concentration. The aim of this section is to describe this dependency.

### 2.1.1 Intrinsic viscosity

The relative viscosity, $\eta_r$, of a solution is defined as

$$\eta_r = \frac{\eta}{\eta_s}\,, \tag{2.1}$$

where $\eta$ is the measured viscosity of the solution and $\eta_s$ is the viscosity of the solvent.

The viscosity may be expanded in a Taylor series in the concentration, such that

$$\eta_r = 1 + [\eta]\, c + k_H\, [\eta]^2\, c^2 + \cdots\,. \tag{2.2}$$

Here, the intrinsic viscosity, $[\eta]$, and the Huggins coefficient, $k_H$, is independent of the concentration.

Rearranging equation (2.2) and taking the limit as $c \to 0$ gives the definition of the intrinsic viscosity.

$$[\eta] = \lim_{c\to 0} \frac{\eta_r - 1}{c} = \lim_{c\to 0} \frac{\eta - \eta_s}{\eta_s c}\,. \tag{2.3}$$

The intrinsic viscosity will in general depend on the shear rate, $\dot{\gamma}$. At very low shear rates however, the intrinsic viscosity will approach a limiting value $[\eta]_0$ known as the zero-shear-rate intrinsic viscosity.

It is found that the the relation between $[\eta]_0$ and the molecular weight can be given by[8]:

$$[\eta]_0 = K' M^a\,, \tag{2.4}$$

where $K'$ and $a$ will depend on the specific solute and solvent. The parameter $a$ is known as the Mark-Houwink exponent.

Hence, a simple dependence on the viscosity of concentration and molecular weight can made by combining equation (2.1), equation (2.2), and equation (2.4).

$$\eta = \eta_s \left(1 + K' M^a c + k' \left(K' M^a\right)^2 c^2\right)\,. \tag{2.5}$$

### 2.1.2 Viscosity of dextran

In this section the viscosity of dextran in water will be determined using data from the literature.

As explained in the previous section, the viscosity of a solution depends on the molecular weight of the solute. However, it also depends on other parameters such as temperature and chemical properties of the solvent. Therefore, the data presented here are all approximately at room temperature. Furthermore, the chemical properties of the solvent can make the solute molecules take different shapes, from curled up (spherical) to more elongated (rod shaped). In this case the solution with the elongated molecules will tend to have the highest viscosity [60]. Therefore, the data presented here will all be with water as solvent.

The data presented here are from [2, 48, 23, 53]. According to equation (2.4) a double logarithmic plot of the intrinsic viscosity and the molecular weight should give a straight line. On figure 2.1 a double logarithmic plot of the collected data and the molecular weight are plotted along with the best fitted line.

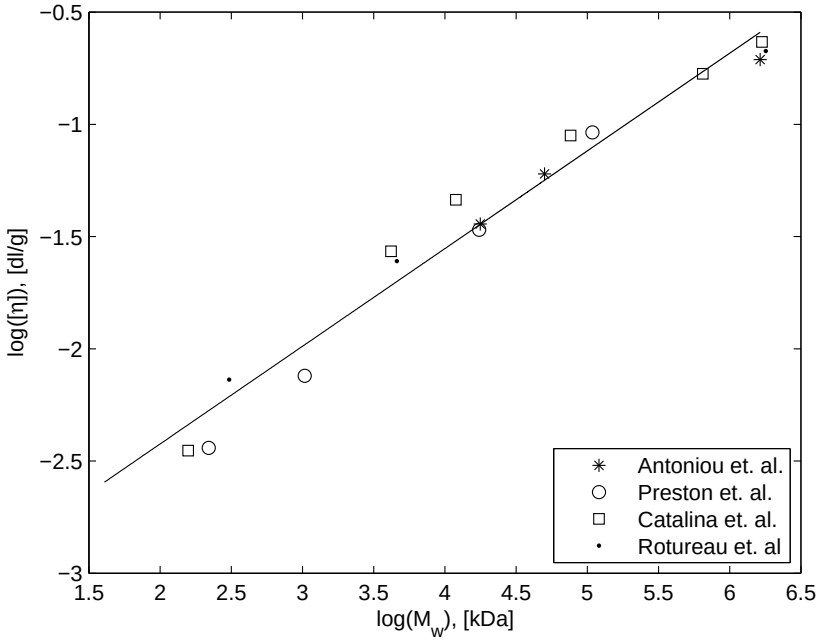


Figure 2.1: Double logarithmic plot of the intrinsic viscosity as a function of molecular weight along with the best fit through the data.

The values that gives the best fit according to equation (2.4) fit are $K' = 0.0371$ and $a = 0.4352$.

On figure 2.2 equation (2.4) with the parameter values given above, and the

data from the literature are plotted.

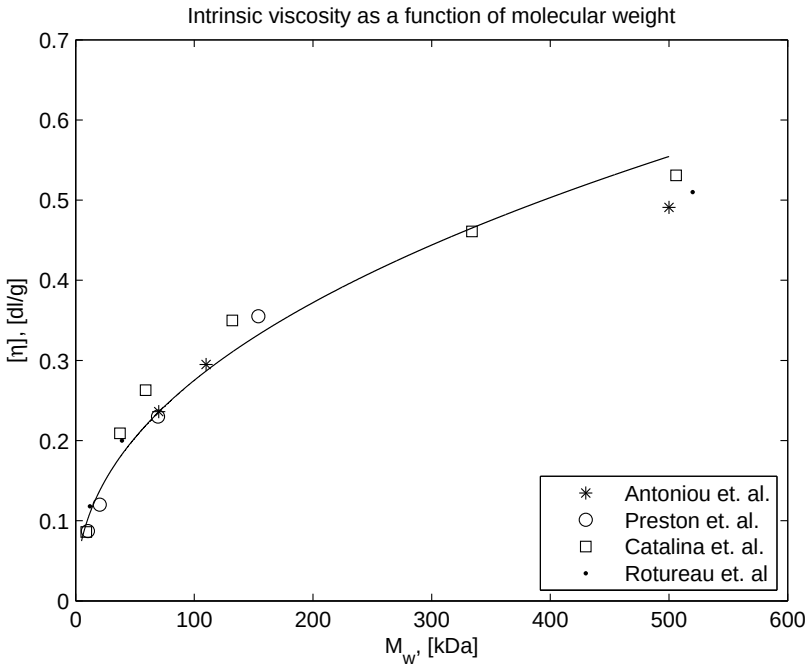


Figure 2.2: The intrinsic viscosity as a function of molecular weight along with the best fit through the data.

In [2, 53] the Huggins coefficient for dextran in water is given to be between 0.495 and 0.58 for molecular weight in the range 10-500 kDa. Using the approximation that $1\text{wt}\% \approx 1\text{g/dl}$ and choosing the Huggins coefficient to be 0.5 the viscosity plotted as a function of concentration can found. This is shown on figure 2.3.

As expected the viscosity increases more rapidly for larger molecules.

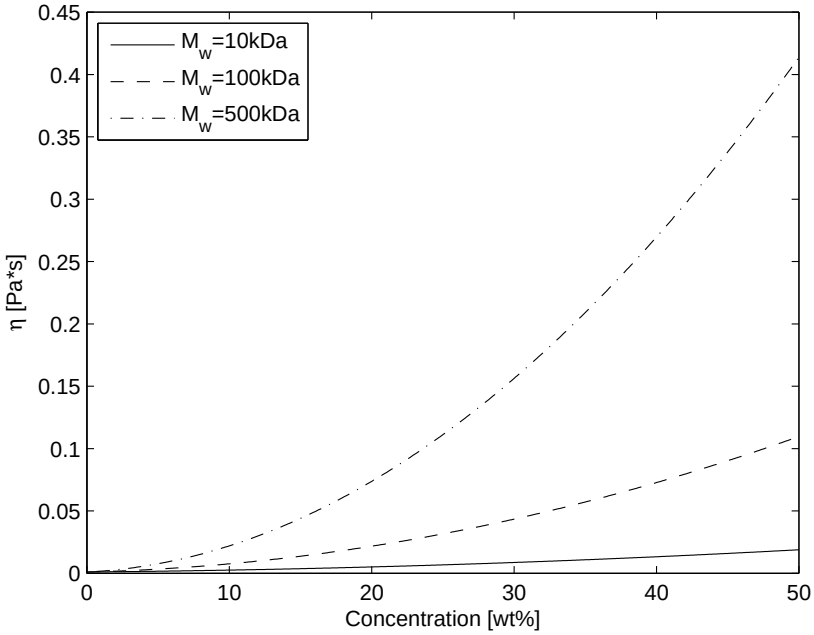


Figure 2.3: The concentration dependence of the viscosity for different molecular weights.

## 2.2 Diffusion coefficient

The diffusion coefficient depends on the size of the molecules in the solution. Using the Stokes-Einstein relation [34] the diffusion coefficient can be given by

$$D = \frac{k_B T}{6\pi\eta_s R_H}\,, \tag{2.6}$$

where $k_B$ is Boltzmann's constant, $T$ is the temperature, $\eta_s$ is the viscosity of the solvent, and $R_H$ is the hydraulic radius.

### 2.2.1 Diffusion coefficient of dextran

Here measurements of $R_H$ as a function of average molecular weight for dextran have been collected from the literature [36, 16, 18, 3, 47]. The diffusion coefficient

has been calculated from equation (2.6), using the temperature of 293.15 Kelvin and the viscosity of water.

On figure 2.4 a log-log plot of the diffusion coefficient as a function of molecular weight, in the range 9.5-2000 kDa, is shown.

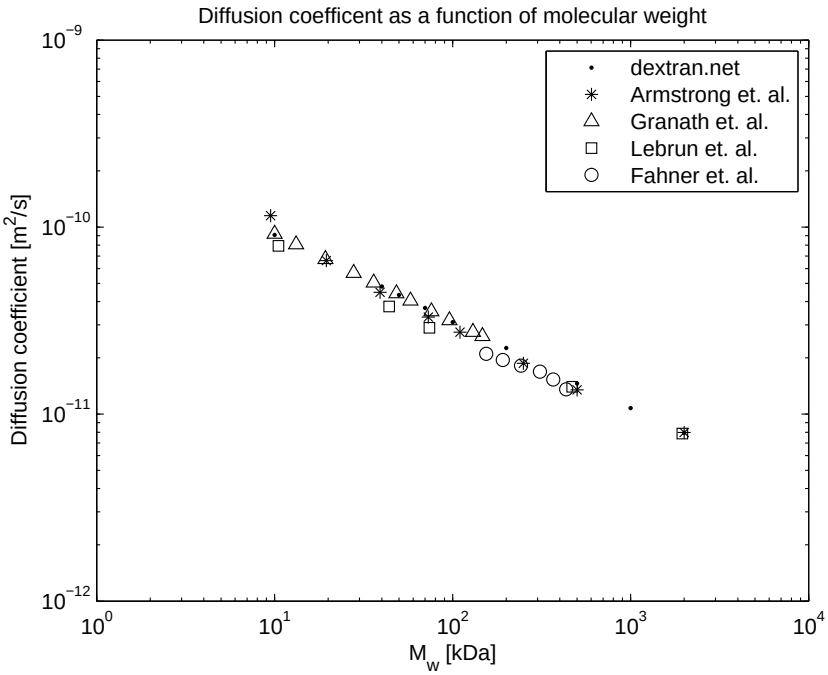


Figure 2.4: Double logarithmic plot of the diffusion coefficient, calculated using equation (2.6) and using data of the hydraulic radius found in the litereature [36, 16, 18, 3, 47], and the molecular weight.

It seems that the points lie approximately on a straight line, suggesting that there is a relationship between the diffusion coefficient and the average molecular weight given by

$$D = k_1 M_w^{k_2} \tag{2.7}$$

Fitting a straight line to the data points in figure 2.4 gives the following values for $k_1$ and $k_2$.

$$k_1 = 2.6804 \cdot 10^{-10}\,, \quad k_2 = -0.4754 \tag{2.8}$$

On figure 2.5 the diffusion coefficients from the literature and a plot of equation (2.7) is shown.

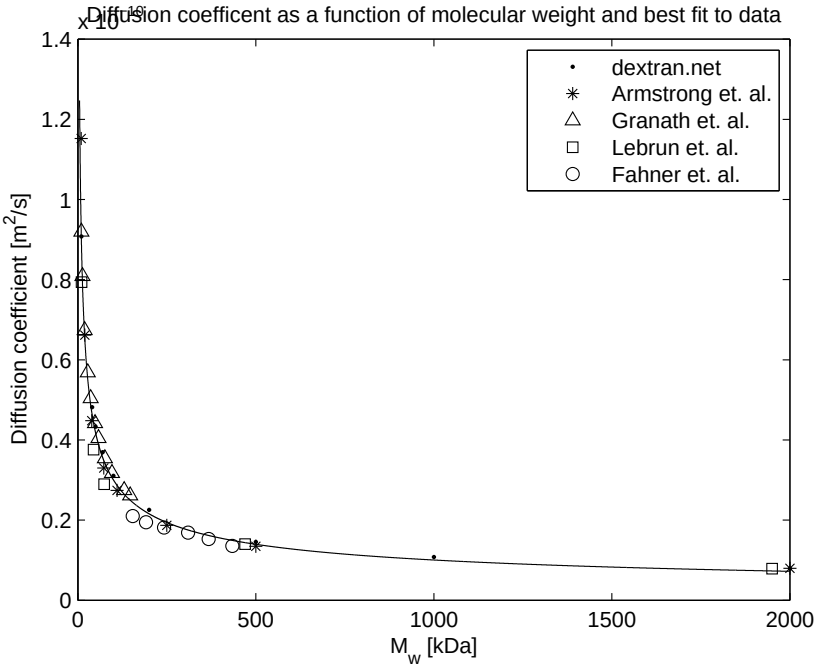


Figure 2.5: The diffusion coefficient as a function of molecular weight. Plotted with different symbols is the diffusion coefficient calculated from equation (2.6) using data of the hydraulic radius found in the literature [36, 16, 18, 3, 47]. The full line is the best fit given by equation (2.7).

As seen there is good agreement between the data points from the literature and equation (2.7).

Therefore, in the model the diffusion coefficient for different molecular weights will be given by equation (2.7) with the parameters given in equation (2.8).

## 2.3 Osmotic pressure

The osmotic pressure for Dextran T10 has been found in [27] to be given by a third degree polynomial

$$\Pi = A_1 c + A_2 c^2 + A_3 c^3 \,, \tag{2.9}$$

where

$$A_1 = 0.1116\,, \quad A_2 = -0.00491\,, \quad A_3 = 0.000257\,. \tag{2.10}$$

Here the concentration is given in wt% and the osmotic pressure is measured in atm, where wt% is defined as

$$\text{wt\%} := \frac{\text{Weight of solute}}{\text{Weight of solution}}\,. \tag{2.11}$$

A plot of equation (2.9) is shown in figure 2.6.

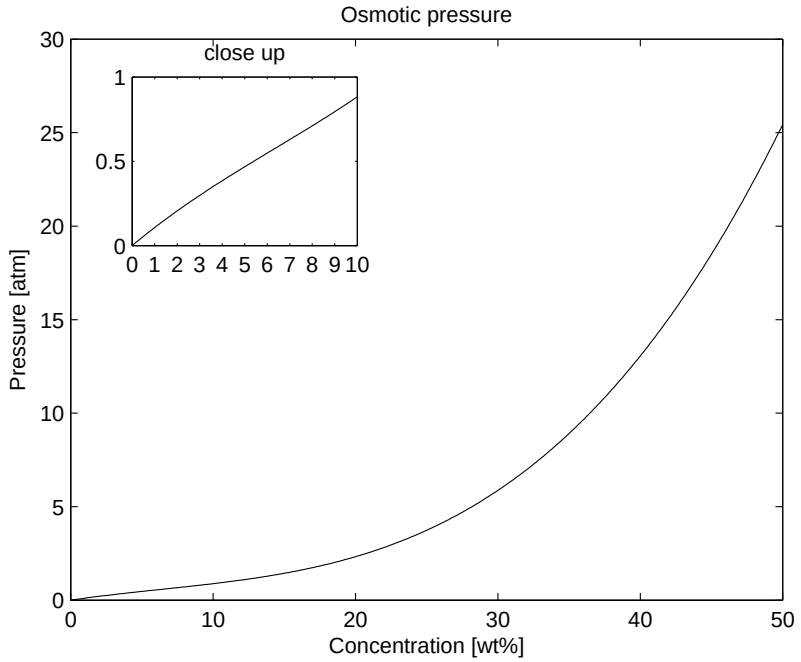


Figure 2.6: The osmotic pressure as a function of concentration as found in [27].

All the expressions presented in this section will be used in the models described in chapter 4 and chapter 5.

Chapter 3

# Statistical model

Separation and Purification Technology 89 (2012) 261–269

Contents lists available at SciVerse ScienceDirect

Separation and Purification Technology

journal homepage: www.elsevier.com/locate/seppur

# Statistical modelling of the interplay between solute shape and rejection in porous membranes

Frank Vinther [a], Manuel Pinelo [b,*], Morten Brøns [a], Gunnar Jonsson [b], Anne S. Meyer [b]

[a] Technical University of Denmark, Department of Mathematics, Matematiktorvet 303s, 2800 Kgs. Lyngby, Denmark
[b] Technical University of Denmark, Department of Chemical and Biochemical Engineering, Center for BioProcess Engineering, Søltofts Plads Bygning 229, 2800 Kgs. Lyngby, Denmark

ARTICLE INFO

*Article history:*
Received 22 December 2011
Received in revised form 13 January 2012
Accepted 14 January 2012
Available online 28 January 2012

*Keywords:*
Rejection coefficient
Membrane separation
Porous membrane
Statistical model
Prolate ellipsoids

ABSTRACT

The structural conformation of complex molecules, e.g., polymers and proteins, is determined by several factors like composition of the basic structural units, charge, and properties of the surrounding solvent. In absence of any chemical or physical interaction solute–solute and/or solute–membrane, it can be expected that the possibility for a solute particle to enter the membrane pore will only depend upon the relation between such molecular conformation and pore size. The objective of the present study is to use geometric and statistical modelling to determine the effect of particle elongation – from spherical to being increasingly prolate ellipsoidal – on the possibility of entering the pore, and, in turn, on the macroscopic distribution coefficient, $K$, and overall retention during filtration. The model showed that the value of $K$ was maximal when the longer of the radii in the prolate ellipsoid was approximately equal to the radius of the pores, in case the spherical size of the particle was smaller than the membrane pore. Furthermore, for spherical particles larger than the pore, such a maximum was found to occur after the smaller of the radii was smaller than the pore radius. Either for spherical particles bigger or smaller than the pore radius, $K$ was monotonically decreasing towards zero as the particles became more elongated. When relating the values of $K$ to the friction model, the maximal rejection coefficient was found to reach a characteristic minimum when changing shape. The results suggested that the retention during porous membrane filtration can be manipulated when working with solute particles prone to alter conformation via, e.g., adding proper functional groups to the molecule, or modifying charge density/distribution by varying pH.



## 1. Introduction

Mathematical modelling has been applied to a wide range of membrane separation processes, from the most simple microfiltration in which practically only pore size has been factored in to complex nanofiltration operations in which more advanced physical principles have been considered, e.g., friction forces or charge effects. The purpose was to use the resulting model as a tool for interpreting – or even better, predicting – the behaviour of critical variables, e.g., flux or rejection, or phenomena, e.g., fouling, inherent to separation systems that were, in most of the cases, very specific.

For many of these models the target has been to describe values of flux across the membrane, which is one of the most decisive variables related to the economic feasibility of membrane separation operations at industrial level. Some of these models recognized the membrane as a porous matrix [1–3], whilst diffusion was considered as the main principle ruling transmission in others [4,5]. Several other models have gone further by focusing on the behaviour of the solute in the bulk solution and treating the membrane as a boundary condition. The common point of such models has been to work on the fluid dynamics on a macroscopic level, which enabled to obtain equations for assessing permeate fluxes [6–8]. Other models have attempted to describe certain membrane separations from a microscopic point of view, ranging from determining the lift of a molecule within the pore [9] to directly investigate total fouling via stochastic models [10–12].

Despite of the fact that the size of the pores and size of the solute molecules are parameters that will dramatically change the outcome of most of the above mentioned models, little or no attention has been paid to the shape of the solute molecules in most of them. In papers that relates the flux through the membrane and include solute shape as a parameter, e.g., [13,14], the microscopic shape of the particle was associated with a macroscopic value, e.g., diffusion constant, Stokes radius, steric partition factor, which was in turn related to other parameters describing the flux through the membrane.

* Corresponding author. Tel.: +45 4525 2950; fax: +45 4588 2258.
*E-mail addresses:* f.vinther@mat.dtu.dk (F. Vinther), mp@kt.dtu.dk (M. Pinelo), m.brons@mat.dtu.dk (M. Brøns), gj@kt.dtu.dk (G. Jonsson), am@kt.dtu.dk (A.S. Meyer).

1383-5866/$ - see front matter © 2012 Elsevier B.V. All rights reserved.
doi:10.1016/j.seppur.2012.01.032

It has been reported that the rejection coefficient, related to the probability of entering a pore, depends on the shape and the size of the molecule [13–17]. Certain molecules are considered completely spherical, e.g., Ficoll whereas other particles are more elongated, e.g., polyethylene oxide [18]. There can be many reasons why the shape of different particles is different. For instance, the shape of proteins can depend on pH – which regulates the charge distribution and density – particularly in cases in which other charge solutes are present in the feed solution or/and the membrane carries some charge groups [19,20]. Accepting the criticism that states that it is difficult to obtain reliable conclusions on permeability-molecular extension relations based on comparisons on molecules of different nature, pH can be also a factor which can help to solve this problem. For example, charge density of carboxymethylcellulose, which bears a carboxylic group for each glucose molecule, increases from low to high pH values. The higher the number of uncharged monomers, the more globular is the conformation, which becomes more linear with increasing charge density (high pH) [21–23].

The scope of this paper is to investigate the effect of a change in shape on a microscopic level, in dead end filtration. More specifically this model investigates the probability of a single molecule to enter a pore, when the shape of the molecule changes from spherical to an increasingly prolate ellipsoidal (elongated) shape. Therefore, this paper will not consider fouling or aggregation of solute particles on the membrane surface or within the membrane pore.

The probability of entering a pore will be related to the distribution coefficient between solute concentration on the membrane surface, $c_{ms}$, and in the membrane pore, $c_{mp}$

$$K = \frac{c_{mp}}{c_{ms}}. \tag{1}$$

In many mathematical models that describe the flux through porous membranes $K$ is a parameter [1,2,24]. These models also predict a rejection coefficient. Hence, assuming that other parameters in these models are not changing when changing the shape of a molecule, a one to one correspondence is given between the distribution coefficient and the rejection coefficient.

To investigate the effect of elongation, the molecules in the model will have the same volume but varying shape. The volume of an ellipsoid $V_e$ is given by

$$V_e = \frac{4}{3}\pi r_1 r_2 r_3. \tag{2}$$

A prolate ellipsoid has $r_1 > r_2$ and $r_2 = r_3$. The volume of the solute particle when spherical, $V_{m,s}$, is then equal to the volume of the same particle when this is a prolate ellipsoid, $V_{m,e}$. Thus,

$$V_{m,s} = \frac{4}{3}\pi R_0^3 = \frac{4}{3}\pi r_1 r_2^2 = V_{m,e}, \tag{3}$$

where $R_0$ is the radius of the molecule when considered spherical. Hence, the following relation is obtained from Eq. (3)

$$r_1 = \frac{R_0^3}{r_2^2}. \tag{4}$$

Letting $r_1 \in [R_0; \infty[$ one has allowed all elongations for a molecule with spherical radius $R_0$. Changing $R_0$ allows investigation of different sized molecules.

One assumption made in this paper is that the molecules hit the membrane surface at random. Hence, the centre of mass will be thought of as an evenly distributed random variable. This is an approach similar to other models that study solute particles in a microscopic perspective [11,12,10], when investigating dead end filtration. Furthermore, it will be assumed that a molecule has no preferred orientation. Hence, the orientation of the molecules will also be an evenly distributed random variable.

The porosity is defined as the ratio of the area of the pores, $A_p$ and the total area of the membrane, $A_m$

$$\xi = \frac{A_p}{A_m}. \tag{5}$$

The membrane will be assumed homogeneous. That is, the pores are circular with the same radius, $r_p$, and evenly distributed across the membrane. This assumption reduces the dimension of the molecules by one, because of the symmetry. Thus, instead of prolate ellipsoids one can look at ellipses.

Under the above assumption the area of the pores is equal to the number of pores, $n$, times the area of an individual pore. Hence,

$$\xi = \frac{n\pi r_p^2}{A_m}. \tag{6}$$

Furthermore, a characteristic length $l = 2r_p$ can be defined such that

$$\xi = \frac{l}{L}, \tag{7}$$

where $L$ is given from Eq. (6), $L = \frac{2A_m}{n\pi r_p}$.

In a Cartesian coordinate system aligned with the membrane surface, the abscissa of the centre of the ellipse is denoted $x_c$. The angle between the direction of $r_1$ and the $y$-axis is denoted $\theta$. Letting $\theta \in \left[-\frac{\pi}{2}; \frac{\pi}{2}\right[$ one has allowed all orientations of the ellipsoid. Letting $x_c \in [0; L]$ one has allowed all positions of the ellipsoid. This is illustrated in Fig. 1.

The molecules will be assumed rigid. Under this assumption the elongated molecules will be able to tilt, as they hit the membrane, depending on the angle of the molecule. This is similar to an egg tilting on a table under the influence of gravity. However, in this situation it is not gravity that tilts the molecule, but the motion of the fluid as a whole, moving downwards through the membrane. Therefore, a molecule will tilt, depending on the angle $\theta$, ending in a position where there is a minimal distance between the membrane surface and the centre of mass (horizontal position). This is illustrated in Fig. 2.

Under these assumption the statistical model can be defined.

## 2. Statistical model

The interesting part is whether or not the molecule will pass into the membrane. Denoting success (entering the pore) by one and failure (not entering the pore) by zero, the sample space is

$$\Omega = \{0, 1\}. \tag{8}$$

The probability of success depends on the two, evenly distributed, random variables; the position of the centre of mass, $x_c$, and the angle $\theta$. Furthermore, it depends on the three parameters $R_0$, $r_1$, and $\xi$, defined in Eqs. (3), (4), and (7).

Both the position of the centre of mass and $\theta$ are continuous random variables, where $x_c$ belongs to the interval $[0; L]$ and $\theta$ belongs to the interval $[\frac{-\pi}{2}; \frac{\pi}{2}]$. This corresponds to the molecules hitting the membrane surface at random positions with random orientations. Thus, for a given set of parameters there exists a probability that the molecule passes into the membrane. This implies that a continuous probability function exists as a function of the parameter $r_1$, where $r_1$ belongs to the interval $[R_0; \infty[$, and $\xi$ and $R_0$ are kept constant.

Knowing the value of $x_c$, $\theta$, $r_1$, and $r_2$ positions of various points on the ellipse, which are important for success or failure, must be found. These are the point on the ellipse furthest to the left, $x_l$, the position of the point on the ellipse furthest to the right, $x_r$, the position of the contact point molecule-membrane, $x_b$, a given arc

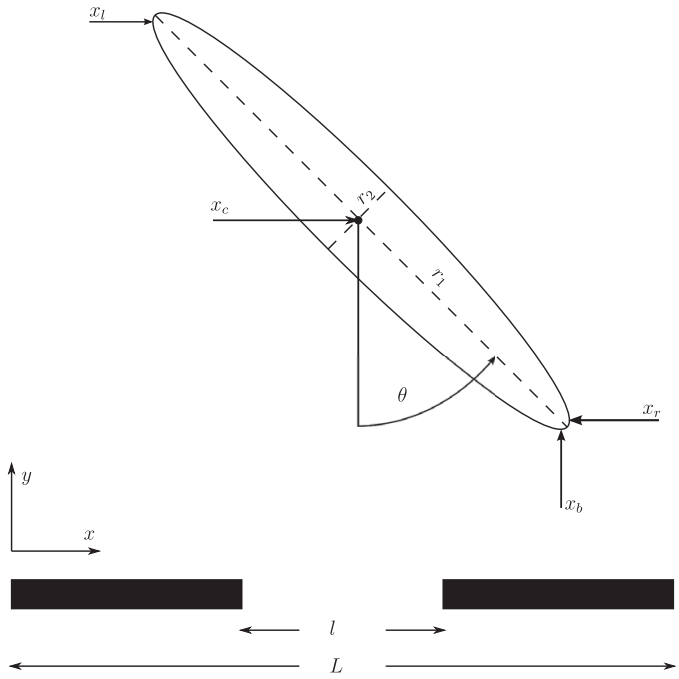


**Fig. 1.** An illustration of the molecule and the membrane. The molecule has two radii $r_1$ and $r_2$ with $r_1 \geqslant r_2$. The angle between the membrane normal and the direction of $r_1$ is $\theta$. The length of the membrane segment is $L$ and the width of the pore is $l$. Also marked is the abscissa of the molecules centre of mass $x_c$, the left and right sides of the molecule, $x_l$ and $x_r$, and the lowest point on the molecule, $x_c$. Furthermore, the coordinate system is illustrated.

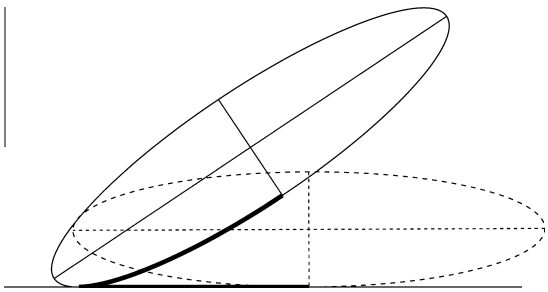

**Fig. 2.** An illustration of where the centre of mass is situated. The distance of the thick line on the ellipse is equal to the thick line on the $x$-axis. Therefore, when pure rolling is assumed the molecule change position in the way illustrated. The initial position being the ellipse that is drawn with a full line, the final position being the ellipse drawn with a dotted line.

length on the ellipse, the position of the centre of mass after a pure rolling $\tilde{x}_c$, and the longest chord within an ellipse from a given point on the ellipse. The geometric calculations needed to find these quantities are presented in Section 3. However, the statistical model can be understood without understanding the underlying mathematics in detail. Therefore, Section 3 serves as an offer to insight in the construction of the numerical method used to obtain the results of this paper and the possibility to reproduce data. However, the reader may skip Section 3 and proceed directly, from the end of this section, to Section 4 for simulation results.

It will be useful to define the interval $\phi$ where the pore is located, that is

$$\phi = \left[\frac{L-l}{2}; \frac{L+l}{2}\right]. \tag{9}$$

The contact point molecule-membrane, $x_b$, can either be within – or outside the pore, $\phi$. There are three situations that lead to success when the contact point molecule-membrane, $x_b$, is within the pore, $\phi$, and one situation that leads to success when the contact point molecule-membrane, $x_b$, is not within the pore, $\phi$.

### 2.1. When the contact point molecule-membrane is within the pore

Success occurs if both the left and the right sides of the molecule are within the pore. In mathematical terms this is expressed as

$$x_l \in \phi \wedge x_r \in \phi. \tag{10}$$

The other two situations that leads to success will depend on the sign of the angle $\theta$.

For $\theta > 0$ success will be defined if the centre of mass is above the pore and the right side of the molecule is above the pore, corresponding to the molecule sliding into the pore. A similar situation exists when $\theta < 0$. In mathematical terms this is written as

$$\theta > 0 \wedge x_c \in \phi \wedge x_r \in \phi \quad \vee \tag{11a}$$
$$\theta < 0 \wedge x_c \in \phi \wedge x_l \in \phi. \tag{11b}$$

Furthermore, the molecule can hit the edge of the pore. If $\theta \geqslant 0$ the molecule will hit the right edge of the hole if and only if $x_r \notin \phi$. In this case the molecule is thought of as tilting around this point. Therefore, the ability of entering the pore depends on the size of the molecule. The longest chord, within the ellipse, $l_c$, from the

point that hits the edge will determine if the molecule enters the pore or will end in a position lying across the pore. There is a similar situation for $\theta \leqslant 0$. Hence, success will be given if

$$\theta \geqslant 0 \wedge x_b \in \phi \wedge x_r \notin \phi \wedge l_c < l \quad \vee \tag{12a}$$
$$\theta \leqslant 0 \wedge x_b \in \phi \wedge x_l \notin \phi \wedge l_c < l. \tag{12b}$$

This is illustrated in Fig. 3.

### 2.2. When the contact point molecule-membrane is not within the pore

When the molecule hits the membrane surface the vertical movement of the centre of mass will cause the molecule to tilt around the point that touches the membrane first. This will lead to the molecule lying horizontally on the surface of the membrane. The direction of tilting will depend on the angle. The molecule will tilt left if $\theta > 0$, right if $\theta < 0$. $\theta = 0$ will correspond to the molecule maintaining its vertical position after the impact with the membrane.

For $\theta > 0$ success will be defined if the position of the molecule, after tilting, is positioned in such a way, that the centre of mass, $\tilde{x}_c$ is above the pore, and the end of the molecule, that did not initially touch the membrane, is above the pore. This situation is illustrated in Fig. 4. In mathematical terms this is defined in the following way:

$$\theta > 0 \wedge x_b \notin \phi \wedge \tilde{x}_c \in \phi \wedge \tilde{x}_c - r_1 \in \phi \quad \vee \tag{13a}$$
$$\theta < 0 \wedge x_b \notin \phi \wedge \tilde{x}_c \in \phi \wedge \tilde{x}_c + r_1 \in \phi. \tag{13b}$$

If none of the above criteria are fulfilled, the outcome will be denoted by failure. Since there are only two possibilities the probability of the molecules not entering the pore is

$$P(0) = 1 - P(1). \tag{14}$$

The distribution coefficient given in Eq. (1) is the ratio between solute concentration within the pore and the solute concentration at the membrane surface. The solute concentration within the pore is related to the probability of the molecule entering the membrane pore. Furthermore, the solute concentration on the membrane surface is related to the probability of the solute molecule not entering the pore (if the molecule does not enter the membrane pore it will be retained at the membrane surface. Hence, contribute to the concentration). This relation is elaborated in Section 4.1.

The distribution coefficient can be related to the maximal rejection under the assumption of a high Peclet number [1,2,24]. This is done in details in Section 4.2, and the validity of the assumption is discussed in Section 5.

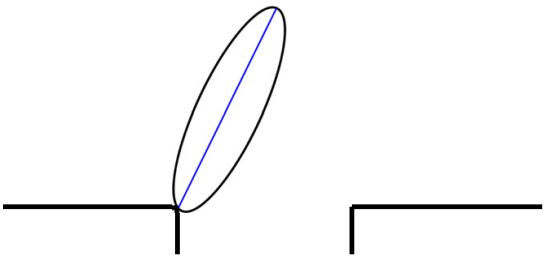

**Fig. 3.** Illustration of a molecule hitting the edge of the pore. The line inside the molecule illustrates the longest chord, $l_c$. Success will depend on the length of this chord relative to the diameter of the pore, $l$.

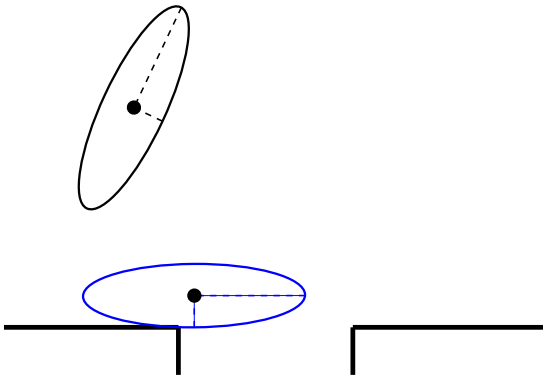

**Fig. 4.** An illustration of a molecule hitting the membrane outside the pore. Success will depend on the position of the centre of mass after pure rolling, $\tilde{x}_c$.

## 3. Geometric computations

This section contains the parametrization of an ellipse, how to calculate the various points, the arcs, and the longest chords needed in the statistical model.

### 3.1. Parametrization of an ellipse

When defining the angle $\theta$ as the angle between the $y$-axis and the longer of the two radii, $r_1$, every point on the ellipse can be found by introducing the parameter $t \in [0; 2\pi]$, such that $t$ is the positive angle measured from the angle $\theta$. This is illustrated in Fig. 5.

In this case the points on the ellipse are given by

$$x(t) = x_c + r_1 \cos(t) \sin(\theta) + r_2 \sin(t) \cos(\theta), \tag{15a}$$
$$y(t) = y_c - r_1 \cos(t) \cos(\theta) + r_2 \sin(t) \sin(\theta), \tag{15b}$$

where $(x_c, y_c)$ is the position of the centre of the ellipse.

### 3.2. Calculation of $x_l$, $x_r$, and $x_b$

As seen it is of interest where the sides of the ellipse is situated relatively to the centre of mass. The two sides can be found from Eq. (15a) as $\tilde{t} \mid \dot{x}(\tilde{t}) = 0$. That is

$$\tilde{t} = \tan^{-1}\left(\frac{r_2}{r_1}\frac{1}{\tan(\theta)}\right). \tag{16}$$

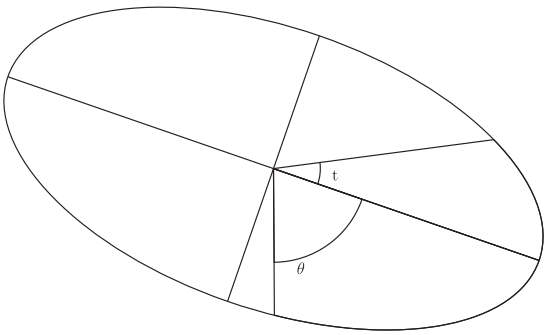


**Fig. 5.** An illustration the parametrization of an ellipse.

There will be two solutions to Eq. (16) and in this case both of them are of interest. Denoting the two solutions by $t_r \in [0;\pi)$ and $t_l \in [\pi;2\pi)$. Then, the right side of the ellipse, $x_r$, and the left side of the ellipse, $x_l$, will be given by

$$x_r = x(t_r) = x_c + r_1\cos(\tilde{t}_r)\sin(\theta) + r_2\sin(\tilde{t}_r)\cos(\theta), \tag{17a}$$

$$x_l = x(t_l) = x_c + r_1\cos(\tilde{t}_l)\sin(\theta) + r_2\sin(\tilde{t}_l)\cos(\theta). \tag{17b}$$

The point of the ellipse that touches the membrane, is the solution $\hat{t}$ of $\dot{y}(\hat{t}) = 0$ for which $\hat{t} + \theta \in \left[-\frac{\pi}{2};\frac{\pi}{2}\right]$.

The $x$-coordinate of the point that touches the membrane will then be given by

$$x_b = x(\hat{t}) = x_c + r_1\cos(\hat{t})\sin(\theta) - r_2\sin(\hat{t})\cos(\theta). \tag{18}$$

### 3.3. Length of an arc

From the point where the molecule touches down on the membrane surface the molecule will roll towards one of the sides depending on the value of $\hat{t}$. The molecule will roll to the right if $\hat{t} \in (0;\frac{\pi}{2})$, and to the left if $\hat{t} \in (\frac{3}{2\pi};2\pi)$. The distance that the molecule will roll will depend on the length of the arc, from the $x_b$ on the ellipse the can be derived from elementary differential geometry [25].

The length of a an segment of an arc from $t_0$ to $t$ is given by

$$s(t_0,t) = \int_{t_0}^{t} \|\dot{\gamma}(u)\|du, \tag{19}$$

where

$$\dot{\gamma}(t) = (\dot{x}(t),\dot{y}(t)). \tag{20}$$

Denoting the angle of integration by $\Phi$, $\Phi = t - t_0$, one can easily show that

$$s(t) = r_2E(\Phi,k) = r_1E(\Phi,m), \tag{21}$$

where $m = \sqrt{1-\left(\frac{r_2}{r_1}\right)^2}$, $k = \sqrt{1-\left(\frac{r_1}{r_2}\right)^2}$. Here $E(\phi,k)$, $E(\phi,m)$ are incomplete elliptic integrals of the second kind.

### 3.4. The position of the centre of mass after rolling

Now one is able to define where the centre of mass will be situated once the molecule has come to rest. The molecule will touch down on the membrane at the point $x(\hat{t}(\theta))$. From this point the molecule will roll to its equilibrium position. The final position of the centre of mass will be derived in the following. There are two situations $\theta > 0$ and $\theta < 0$.

When $\theta < 0$ we have $\hat{t} \in (0;\frac{\pi}{2})$. This implies that the position of the centre mass after rolling, $\tilde{x}_c$ is

$$\tilde{x}_c = x(\hat{t}) + \int_{\hat{t}}^{\frac{3\pi}{2}} \|\dot{\gamma}(t)\|dt. \tag{22}$$

When $\theta > 0$, $\hat{t} \in (\frac{3\pi}{2};2\pi)$. This implies that the position of the centre of mass after rolling will be given by

$$\tilde{x}_c = x(\hat{t}) - \int_{\frac{3\pi}{2}}^{\hat{t}} \|\dot{\gamma}(t)\|dt. \tag{23}$$

The first situation is illustrated in Fig. 2.

### 3.5. The longest chord in an ellipse

The length of a chord in an ellipse is given by

$$|\,\bar{\gamma}(s,\tilde{s})\,| = |\,\gamma(s) - \gamma(\tilde{s})\,|\,. \tag{24}$$

Thus, the problem reduces to; given $s$, what is the value of $\hat{s}$, where $\hat{s}$ is defined as

$$\hat{s} = \{\tilde{s} \mid \tilde{s} \in [0;2\pi[, |\,\bar{\gamma}(s,\hat{s})\,| = \max |\,\bar{\gamma}(s,\tilde{s})\,| \;\forall\tilde{s}\}. \tag{25}$$

The value of $\hat{s}$ will be found by solving the equation

$$\frac{d}{d\tilde{s}}|\,\bar{\gamma}(s,\tilde{s})\,| = 0, \quad s \neq \tilde{s}. \tag{26}$$

The relation between $s$ and $\hat{s}$ is given by the following equation

$$\sin(\hat{s}-s) = k^2[\cos(s) - \cos(\hat{s})]\sin(\hat{s}). \tag{27}$$

In the specific statistical model this will be used in the following way. If $x_b = x(\hat{t}) \in \phi \wedge x_r = x(t_r) \notin \phi$ then there will be an angle $s : \hat{t} < s < t_r, s \in ]-\frac{\pi}{2};\frac{\pi}{2}[$, such that

$$x_c + r_1\cos(s)\sin(\theta) + r_2\sin(s)\cos(\theta) = \frac{L+l}{2}. \tag{28}$$

The angle $s$ then defines the point on the ellipse from where to find the longest chord. As seen in Eq. (27) there exist an angle $\hat{s}$ such that $|\,\gamma(s) - \gamma(\hat{s})\,|$ is the longest chord from $\gamma(s)$. The molecule will be thought of as tilting around the point specified in Eq. (28). Hence, success will be defined if and only if $l_c = |\,\gamma(s) - \gamma(\hat{s})\,| < l$.

## 4. Results

First a few remarks on what to expect, from the model, and why.

The simplest situation is when the molecule is large compared to the radius of the pore ($R_0 > \frac{l}{2}$). In this case, when the molecule is spherical, no molecules will enter the pore. When the molecule becomes so elongated that the smaller of the two radii is equal to the radius of the pore, $r_2 = \frac{l}{2}$, there will exist a possibility of the molecule entering the pore. At exactly this point only molecules that hit the membrane with centre of mass directly above the centre of the pore, and an angle of zero, can enter the membrane. This event has an effective probability of success equal to zero. When the molecule becomes more elongated one would expect the probability of success to increase. When the molecules become infinitely long only molecules above the pore and with an angle of zero can enter the membrane. Thus, the probability of a molecule entering the membrane will be zero. Hence, a maximum must exist. A simulation of the statistical model can be seen in Fig. 6.

Another possibility is that the solute molecules are small compared to the pore radius ($R_0 < \frac{l}{2}$). In this case, when the molecules

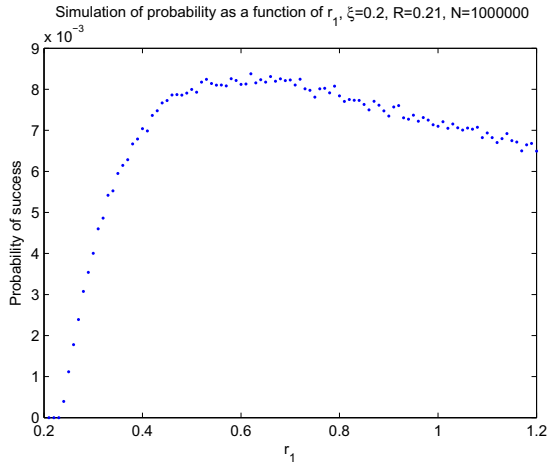


**Fig. 6.** The probability of success as a function of $r_1$, with the parameters $R_0 = 0.21$, $\xi = 0.2$. For each value of $r_1$ $10^6$ simulations have been made.

are spherical the probability of the molecule entering the membrane is equal to the porosity. This is because the probability only depends on the position of the centre of mass, which in return is a random variable. When the molecule becomes more elongated there is a possibility of the molecule tilting into the pore when having centre of mass outside the pore. This will in return increase the probability. As with the larger molecules, the probability must tend to zero, when the longer of the two radii tends to infinity. Hence, also in this situation a maximum exist. A simulation of the statistical model showing can be seen in Fig. 7.

Clearly the most interesting part of Fig. 7 is the part where the maximum exist. A figure illustrating this part more clearly is given in Fig. 8.

As seen from Fig. 8 the probability of success when the molecule is spherical is equal to the porosity as expected. Furthermore, the probability is seen to increase as the length of $r_1$ increases. The increase continues until a peak at approximately $r_1 = \frac{l}{2}$. From a physical point of view a peak, at exactly this value, can be explained from the fact, that for values of $r_1$ larger than this value molecules will be able to lie across the pore. Hence, molecules landing on the edge of the pore will not enter the pore. Of course, this effect increases as $r_1$ becomes longer.

The influence of changing the porosity and maintaining the original volume of the molecule is shown in Fig. 9.

As seen from the figure this changes the probability of entering the pore proportional to the change in porosity. Hence, the maximum probability of entering the pore is approximately two times higher on Fig. 7 compared to Fig. 9. Furthermore, the probability in Fig. 9 is seen to decrease more rapidly after the maximum, as compared to Fig. 7.

From Figs. 9 and 8, it is seen that there is approximately 20% increase in the probability for entering the membrane when $r_1 = \frac{l}{2}$ compared to $r_1 = R_0$. That is

$$P\left(1 \mid r_1 = \frac{l}{2}\right) \approx 1.2P(1 \mid r_1 = R_0). \tag{29}$$

### 4.1. Relation between K and the statistical model

As mentioned $K$ is the distribution coefficient of solute concentration between the membrane surface, $c_{ms}$, and the membrane pore, $c_{mp}$, Eq. (1).

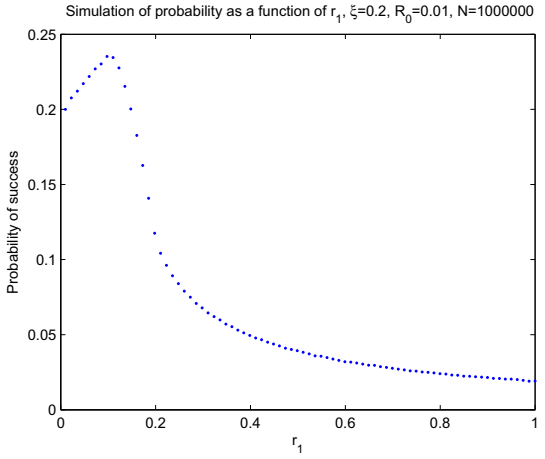


**Fig. 7.** The probability of success as a function of $r_1$, with the parameters $R_0 = 0.01$, $\xi = 0.2$. For each value of $r_1$ $10^6$ simulations have been made.

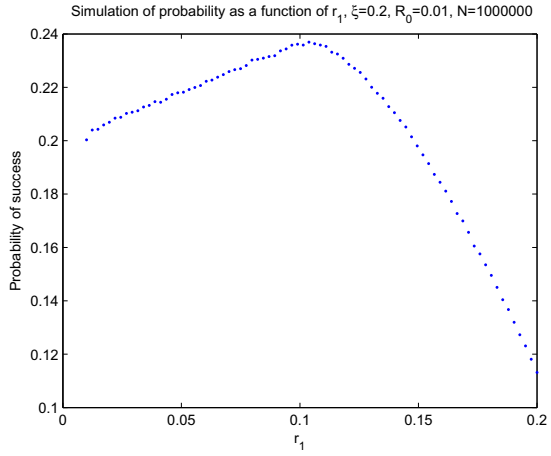


**Fig. 8.** The probability of success as a function of $r_1$, with the parameters $R_0 = 0.01$, $\xi = 0.2$. For each value of $r_1$ $10^6$ simulations have been made.

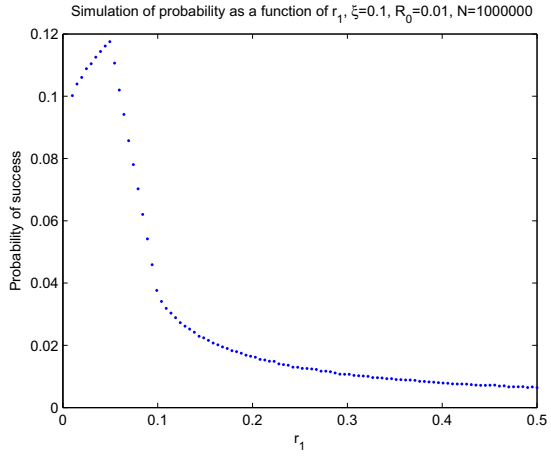


**Fig. 9.** The probability of success as a function of $r_1$, with the parameters $R_0 = 0.01$, $\xi = 0.1$. For each value of $r_1$ $10^6$ simulations have been made.

Assume that all particles are spherical and $R_0 < \frac{\xi}{2}$ and they are randomly distributed. In this case the concentration in the pore will be equal to the concentration in the bulk solution. This is due to the fact that all particles with centre of mass directly above the pore will enter the pore. Hence, one can think of the column of fluid directly above the pore as being repeated within the pore.

The statistical model presented in this paper also relates the shape of the particle to the probability of entering the pore. However, since no accumulation of solute particles on the membrane surface is included in the model, it is only possible to relate the results of the model, to experiments on non-fouled membranes, or at the beginning of a separation process.

Under these assumptions the concentration in the membrane pore is related to the probability of a solute particle to enter the pore, and the concentration at the membrane surface is related to the probability of the molecule not entering the membrane pore. If one furthermore assumes that the time interval under consideration is such that all molecules that enter a pore does not exit the

pore, and that there is no accumulation of particles in the vicinity of each individual pore on the membrane surface, the distribution coefficient will be given by

$$K = \frac{P(1 \mid R_0, r_1, \xi)}{P(0 \mid R_0, r_1, \xi)} = \frac{P(1 \mid R_0, r_1, \xi)}{1 - P(1 \mid R_0, r_1, \xi)}. \quad (30)$$

A plot of the distribution coefficient as a function of $r_1$ in the case presented in the previous section (Fig. 7) is shown in Fig. 10.

As seen, from Eq. (30) the distribution coefficient behaves in a similar way as the probability of entering the pore behaves. Hence, the discussions related to the probability of entering the pore, as a function of $r_1$, can be repeated when explaining the behaviour of the distribution coefficient, as a function of $r_1$.

### 4.2. Relation to mathematical models

In [1,2,24], the maximum rejection, $R_{max}$, was found by letting the flux through the membrane (the Peclet number) tend to infinity. The expression for $R_{max}$ is given by

$$R_{max} = \sigma = 1 - \frac{K}{b}, \quad (31)$$

where $b$ is a friction coefficient,

$$b = 1 - \frac{f_{sm}}{f_{sw}}. \quad (32)$$

Here $f_{sm}$ denotes a friction coefficient between the solute and the membrane and $f_{sw}$ denotes a friction coefficient between the solute and the solvent.

If one assumes that $b$ is constant when changing the elongation the statistical model predicts a rejection coefficient, on a non-fouled membrane or at the beginning of a separation experiment, that varies as a function of elongation.

Using the expression of the distribution coefficient found in the previous section, Eq. (30), and inserting this into Eq. (31), the maximal rejection will be given by

$$R_{max} = 1 - \frac{P(1 \mid R_0, r_1, \xi)}{1 - P(1 \mid R_0, r_1, \xi)}. \quad (33)$$

A plot of this using the same parameters as in Figs. 7 and 10 is shown in Fig. 11.

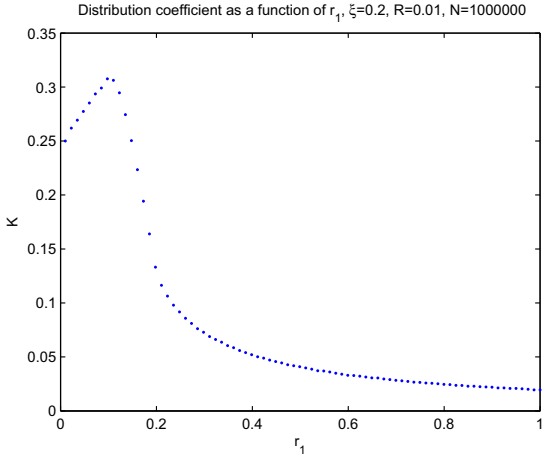


**Fig. 10.** The distribution coefficient as a function of $r_1$, with the parameters $R_0 = 0.01$, $\xi = 0.2$. For each value of $r_1$ $10^6$ simulations have been made.

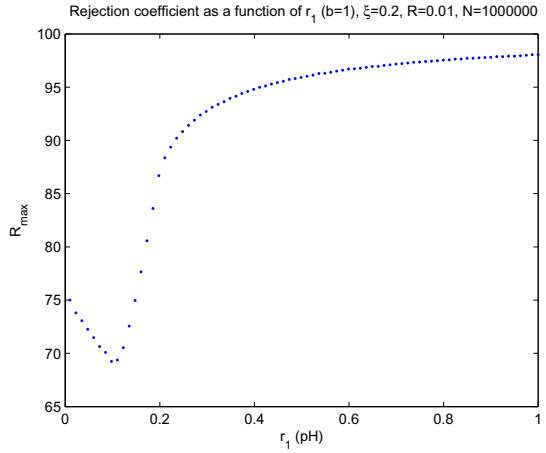


**Fig. 11.** The maximum rejection as a function of $r_1$, with the parameters $R_0 = 0.01$, $\xi = 0.2$. For each value of $r_1$ $10^6$ simulations have been made.

## 5. Discussion

The statistical model showed a relation between the coefficient of distribution of solute concentration between the membrane surface and the membrane pore, $K$, measured in terms of probability of solute entering the pore, and the molecular shape of the solute particle for a given membrane pore size.

As seen in Figs. 6, 7, and 9 the probability of a solute particle to pass into a pore was found to follow two tendencies, depending on the volume of the molecule. For molecules with a large volume compared to pore area ($R_0 > \frac{l}{2}$) the coefficient of distribution was found to be zero until the elongation corresponded to the smaller of the two radii being equal to the pore radius ($r_2 = \frac{l}{2}$). A further increase in elongation resulted in an increase in probability until a maximum was obtained. Further elongation implied a monotonically decreasing probability. This result indicates, when having large solute molecules compared to pore radius, it would be beneficial to have the solute molecules in a globular shape.

For solute molecules that are small compared to pore radius ($R_0 < \frac{l}{2}$) the probability of the solute molecule was found to follow two tendencies. Initially, when the spherical-shaped particle ($R_0 = 0.01$) was elongated to a prolate ellipsoidal-shaped particle with the longer of the two radii equal to the half the pore size of the membrane, a peak of maximal probability of entering the pore (approximately 20% higher than the initial value) was observed. This increase is ascribable to the fact that a higher number of molecules will have the possibility of tilting into the pore as a function of elongation, hence a higher probability.

The relation between $R_{max}$ and the distribution coefficient, $K$, shown in this study, Eq. (31), is based on the assumption that diffusion is negligible as compared to convection (high Peclet numbers). This is true in microfiltration and ultrafiltration, where fluxes are high and diffusion coefficients for large molecules small, resulting in high Peclet numbers. Therefore, the membrane rejection will be very close to the maximum rejection [1,2]. In Reverse osmosis, the distribution coefficient is rather a function of the physical–chemical interactions between membrane and solute, e.g., interaction between membrane material and salt charges, rather than a function of the geometry and sizes of pores and solutes, therefore the validity of the model is doubtful for reverse osmosis applications.

The increase of permeability for slightly elongated solutes predicted by the model has been confirmed in a previous study

including four different polymers with increasing Stokes radius (Ficoll < dextran < pullulan < polyethylene oxide) and similar molecular weight [18]. The study showed a significant increase of the sieving coefficient – related to permeability – with increasing Stokes radius, and revealed that permeability could be correlated to slight increases of molecular elongation. The same effect was observed for 1-propanol and 2-propanol, 1- and 2-butanol, and 1- and 2-pentanol when studying the rejection on nanofiltration membranes [13]. Assuming a cylindrical shape for all the species and having 1-alcohols a slight higher molecular length in all cases, the permeability was found to be lower for 2-alcohols. In [14], rejection data was given for various solute molecules. Furthermore, the molecular shape was fitted to prolate ellipsoids. Relating solute molecules of similar molecular volume (3-hexanol and 1,8-octanediol) but different shape, the permeability of 1,8-octanediol, which was found to be more elongated than 3-hexanol, was found to be higher at low Peclet numbers, where a random orientation is most valid. Furthermore, for solute molecules having the same shape but different molecular volume (glucose and glycerol), the permeability was found to be higher for glycerol, which has the smallest volume. The shape and size of solute molecules was also studied in [15–17], they found that the most important parameter was not the shape but the size. As seen from Figs. 7 and 9 this paper also found that the size of molecule, relative to the size of the pore, has a major influence on the permeability.

The lower permeability of spherical – or globular – conformations has particular importance during filtration of proteins, e.g., albumin, bikunin, catalase, ribonuclease, which commonly have a structure more close to a rigid sphere as compared to more extended polymers of similar molecular weight, e.g., dextran, whose permeabilities are higher [18,26].

A peak of maximal permeability is also observed when the pore size of the membrane was increased (Fig. 6). Also in this case, the maximal value of permeability is attained when the radius of the particle corresponds to half the pore size radius. However, the main difference is that the permeability increased almost 100% when the pore size was doubled. In experiments with membranes of different pore sizes, i.e., NF70 (MWCO = 250), UTC-20 (180), NTR 7450 (600–800), and Zirfon (2000–3000), the tendency of retention for a group of solutes within a range of molecular weight (32–696) was quite different. Whilst a gradual increasing curve retention-solute molecular weight was observed for NTR 7450 and Zirfon (high pore sizes), a sharply increasing function was observed for the other two membranes [17]. This indicates that a higher pore size allows a higher number of molecular conformations (or positions of the mass centre of particles) to pass through. If this hypothesis was correct, it would mean that the spatial disposition of the solute particle – and probably also the flexibility – in the solution gains importance as confronted to the molecular weight as the pore size becomes lower. For high pore sizes then, spatial disposition of the particles loses importance, as particles will encounter the pore anyway.

The model predicted a sharp decrease of permeability for ellipsoid-shaped particles whose $r_1$ increases from the size of the membrane pore radius to the diameter (Figs. 7 and 9). After that, the permeability followed a slow, progressive decrease. Such results imply that, in general, the separation of totally linear molecules is much easier than the separation of equivalent molecules – equivalent meaning that have the same total volume – with a globular shape. For molecules that change shape with operation conditions, e.g., pH or ionic strength, the model suggests to manipulate the conditions in such a manner that the molecule becomes linear when a high rejection is required. For example, increasing pH during filtration of carboxymethylcellulose results in an increase of negative charges in the molecular structure, which causes the molecule to be more linear [21]. This would decrease the transmission of the molecule across the membrane, as predicted by the model. There is scarcity of studies in which the filtration of the same compound with different conformations have been compared. In those few cases, the interpretation of the observations related to filtration efficiency is complicated because of the possible confounding effects of chemical conformation on charge with effects on size and shape [27]. Ficoll is probably the most studied molecule to this regard. It is assumed to have an ideal spherical shape and is used to study pore size distribution and permeability of membranes [28]. Recent studies have compared the glomerular permeability of anionic versus neutral ficoll and the enhanced permeability of anionic versus neutral ficoll was explained by electrostatic interactions independent of size and conformation [29]. Other studies compared the retention of small molecules, e.g., methanol, isopropanol, with bigger ones like benzoic acid or benzylalcohol in nanofiltration membranes, and reported the expected higher levels of retention for the bigger molecules, albeit molecular weights were quite different [17]. The same effect was observed for monodisperse solutions of PEG of increasing molecular weights, in which the rejection decreased exponentially as the molecular weight increased from 2 to 35 kDa [30].

The present paper is capable of relating the distribution coefficient and maximal rejection coefficient to the probability of success on a non-fouled membrane, or in an infinitesimal time interval in the beginning of a separation experiment. Other predictions can be made about the kind of fouling one can expect. When the molecules are very elongated such that the probability of entering a pore is very small, one would expect that the solute molecules accumulate on the membrane surface. Hence, in these experiments a high concentration polarization, or external fouling would be expected. Furthermore, this model does not focus on the interaction between the solute molecules and the membrane pore. Assuming that the molecule has a tendency to interact with the membrane within the pore a high internal fouling would be expected when the probability of the solute molecule entering the pore is high. If on the other hand there is no interaction between the solute and the membrane pore a lower rejection is expected when the probability of the solute molecule entering the pore is high.

The model also predicts that very large molecules will have higher probability of entering the membrane pore when prolate ellipsoidal compared to spherical. This prediction would be fairly easy to test, if the shape of the molecule depends on a single parameter, e.g., pH. The predicted consequence would be either internal fouling or a rejection different from 100%.

## 6. Conclusions

The main conclusion of the paper is that the shape of the molecule alters the probability of entering a membrane pore on a non-fouled membrane. In absence of any kind of interaction solute–solute or solute–membrane, and assuming the same molecular volume for all configurations, there were two cases depending on the ratio between spherical particle size and pore size.

When the radius of the spherical particles were larger than the pore radius, the probability of entering the pore was found to zero until an elongation corresponding to the smaller of the two radii in the ellipsoid was equal to the pore radius. At this point the probability was found to increase until a maximum was obtained. A further increase in elongation resulted in a monotonically decreasing probability.

When the radius of the spherical particles was smaller than the pore radius, the probability was found to be equal to the porosity, when the particle was spherical. An increase in elongation resulted in an increasing probability of entering the pore, until a maximum

was obtained. This maximum occurred when the longer of the two radii in the ellipsoid was approximately equal to the radius of the pore. A further elongation beyond this maximum resulted in a probability decreasing monotonically towards zero.

A relation between the probability of a molecule entering the membrane pore was related to the distribution coefficient, $K$, and to the maximal rejection, $R_{max}$. The maximal rejection was found follow the opposite behaviour than the probability of a particle entering the membrane pore. Hence, having a characteristic minimum when the longer of the two radii in the ellipsoid was approximately equal to the radius of the pore, in case of molecules with spherical particle size smaller than the pore size. These relations are considered a good approximation for porous transport through membranes, where the convective contribution to the flux is large compared to the diffusive term, i.e., ultrafiltration and microfiltration.

This means that spherical conformations of molecules, small compared to pore size, have higher probabilities of passing into pores of a given membrane as compared to very linear shapes. This is of particular interest during the filtration of molecules whose conformation can be manipulated by modifying certain operational variables, e.g., carboxymethylcellulose at different pH, and implies that the rejection of such molecules during membrane filtration can be controlled in accordance with the molecular shape. Furthermore, this could play an important role during the filtration of spherical-shaped proteins, e.g., catalase and albumin, as small modifications in the structure, e.g., by changing the charge density, could result in important decreases of rejection during membrane purification.

Future versions of the present model will include additional parameters that factor in likely interactions between different solutes, due to, e.g., charge or hydrogen bonds, beyond the merely geometrical parameters considered in this version. However, the present model provides the basic insights and the benchmark rejection which can be expected before any physical or chemical interactions affect the filtration.

## References


[1] K. Spiegler, O. Kedem, Thermodynamics of hyperfiltration (reverse osmosis): criteria for efficient membranes, Desalination 1 (1966) 311–326.
[2] G. Jonsson, C. Boesen, Water and solute transport through cellulose acetate reverse osmosis membranes, Desalination 17 (1975) 145–165.
[3] P. Dolecek, Mathematical modelling of permeate flow in multichannel ceramic membrane, Journal of Membrane Science 100 (1995) 111–119.
[4] J.G. Wijmans, R.W. Baker, The solution-diffusion model: a review, Journal of Membrane Science 107 (1995) 1–21.
[5] J. Paris, P. Guichardon, F. Charbit, Transport phenomena in ultrafiltration: a new two-dimensional model compared with classical models, Journal of Membrane Science 207 (2002) 43–58.
[6] P. Henriksen, O. Hassager, Simulation of transport phenomena in ultrafiltration, Chemical Engineering Science 48 (1993) 2983–2999.
[7] M. Hansen, V.A. Barker, O. Hassager, Spectral element simulation of ultrafiltration, Chemical Engineering Science 53 (1998) 3099–3115.
[8] K. Damak, A. Ayadi, P. Schmitz, B. Zeghmati, Modeling of crossflow membrane separation processes under laminar flow conditions in tubular membrane, Desalination 168 (2004) 231–239.
[9] F. Altena, G. Belfort, Lateral migration of spherical particles in porous flow channels: application to membrane filtration, Chemical Engineering Science 39 (1984) 343–355.
[10] M. Wessling, Two-dimensional stochastic modeling of membrane fouling, Separation and Purification Technology 24 (2001) 375–387.
[11] Y. Chen, H. Kim, Monte Carlo simulation of pore blocking and cake formation by interfacial interactions during membrane filtration, Desalination 233 (2008) 258–266.
[12] Y. Li, N. Vu, A.S. Kim, 3-d Monte Carlo simulation of particle deposition on a permeable surface, Desalination 249 (2009) 416–422.
[13] Y. Kiso, K. Muroshige, T. Oguchi, T. Yamada, M. Hhirose, T. Ohara, T. Shintani, Effect of molecular shape on rejection of uncharged organic compounds by nanofiltration membranes and on calculated pore radii, Journal of Membrane Science 358 (2010) 101–113.
[14] J.L. Santos, P. de Beukelaar, I.F. Vankelecom, S. Velizarov, J.G. Crespo, Effect of solute geometry and orientation on the rejection of uncharged compounds by nanofiltration, Separation and Purification Technology 50 (2006) 122–131.
[15] L. Braeken, R. Ramaekers, Y. Zhang, G. Maes, B.V. der Bruggen, C. Vandecasteele, Influence of hydrophobicity on retention in nanofiltration of aqueous solutions containing organic compounds, Journal of Membrane Science 252 (2005) 195–203.
[16] K.O. Agenson, J.-I. Oh, T. Urase, Retention of a wide variety of organic pollutants by different nanofiltration/reverse osmosis membranes: controlling parameters of process, Journal of Membrane Science 225 (2003) 91–103.
[17] B.V. der Bruggen, J. Schaep, D. Wilms, C. Vandecasteele, Influence of molecular size, polarity and charge on the retention of organic molecules by nanofiltration, Journal of Membrane Science 156 (1999) 29–41.
[18] D. Asgeirsson, D. Venturoli, E. Fries, B. Rippe, C. Rippe, Glomerular sieving of three neutral polysaccharides, polyethylene oxide and bikunin in rat: effects of molecular size and conformation, Acta Physiologica 191 (2007) 237–246.
[19] M. Pinelo, C. Ferrer, A.S. Meyer, G. Jonsson, Controlling the rejection of protein during membrane filtration by adding selected polyelectrolytes, Separation and Purification Technology 85 (2012) 54–60.
[20] H. Sun, D. Qi, S.J.J. Xu, C. Zhe, Fractionation of polysaccharides from rapeseed by ultrafiltration: effect of molecular pore size and operation conditions on the membrane performance, Separation and Purification Technology 80 (2011) 670–676.
[21] J. Fujimoto, D. Petri, Adsorption behavior of carboxymethylcellulose on amino-terminated surfaces, Langmuir 17 (2001) 56–60.
[22] C. Hoogendam, A.D. Keizer, M.C. Stuart, B. Bijsterbosch, J. Smit, J.V. Dijk, P.V.D. Horst, J. Batelaan, Persistence length of carboxymethyl cellulose as evaluated from size exclusion chromatography and potentiometric titrations, Macromolecules 31 (1998) 6297–6309.
[23] M. Pinelo, G. Jonsson, A.S. Meyer, Membrane technology for purification of enzymatically produced oligosaccharides: molecular and operational features affecting performance, Separation and Purification Technology 70 (2009) 1–11.
[24] M. Mulder, Basic Principles of Membrane Technology, Kluwer Academic Publishers, 2003.
[25] A. Pressley, Elementary Differential Geometry, Springer-Verlag, 2007.
[26] M. Ohlson, J. Sœrensson, K. Lindstrœm, A. Blom, E. Fries, B. Haraldsson, Effects of filtration rate on the glomerular barrier and clearance of four differently shaped molecules, American Journal of Physiology – Renal Physiology 281 (2001) F103–F113.
[27] J. Groszek, L. Li, N. Ferrell, R. Smith, C. Zorman, C. Hofmann, S. Roy, W. Fissell, Molecular conformation and filtration properties of anionic ficoll, American Journal of Physiology – Renal Physiology 299 (2010) F752–F757.
[28] W. Janssen, A. Ribickas, L. Meyer, R. Smilee, Large-scale ficoll gradient separations using a commercially available, effectively closed, system, Cytotherapy 12 (2010) 418–424.
[29] J. Axelsson, K. Sverrisson, A. Rippe, W. Fissell, B. Rippe, Reduced diffusion of charge-modified, conformationally intact anionic ficoll relative to neutral ficoll across the rat glomerular filtration barrier in vivo, American Journal of Physiology – Renal Physiology 301 (2011) F708–F712.
[30] N. Ochoa, P. Prádanos, L. Palacio, C. Pagliero, J. Marchese, A. HernSSndez, Pore size distributions based on afm imaging and retention of multidisperse polymer solutes: characterisation of polyethersulfone uf membranes with dopes containing different pvp, Journal of Membrane Science 187 (2001) 227–237.

Chapter 4

# Stationary model

# Mathematical modelling of dextran filtration through hollow fibre membranes

Frank Vinther[a], Manuel Pinelo[b,1,*], Morten Brøns[a], Gunnar Jonsson[b], Anne S. Meyer[b]

[a]*Technical University of Denmark, Department of Applied Mathematics and Computer Science, Matematiktorvet 303B, 2800, Kgs. Lyngby, Denmark*
[b]*Technical University of Denmark, Department of Chemical and Biochemical Engineering, Center for BioProcess Engineering, Søltofts Plads Bygning 229, 2800, Kgs. Lyngby, Denmark*

**Abstract**

In this paper we present a mathematical model of an ultrafiltration process. The results of the model are produced using standard numerical techniques with Comsol Multiphysics. The model describes the fluid flow and separation in hollow fibre membranes. The flow of solute and solvent within the hollow fibre is modelled by solving the Navier-Stokes equation along with the continuity equation for both the solute and the solvent. The flux of solute and solvent through the membrane are given by the solution diffusion model, since ultrafiltration occurs at high rejections. For a given set of parameters describing the characteristics of the membrane, effect on the observed and the intrinsic rejection of the membrane are investigated for the different working parameters: inlet velocity, molecular weight, and transmembrane pressure. Furthermore, the model investigates the effect of a concentration dependent viscosity.

The model shows that both the observed and intrinsic rejection increase when the inlet velocity increases. Moreover, the intrinsic rejection increases as a function of transmembrane pressure, but the observed rejection has a characteristic maximum. Therefore, the observed rejection can either increase or decrease as a function of pressure.

The influence of a concentration dependent viscosity is to increase the concentration on the membrane surface. This leads to a decrease in both the observed and the intrinsic rejection, when compared to a constant viscosity.

For small values of the solute permeability the concentration dependent viscosity decreases the volumetric flux through the membrane at high pressures. This effect is due to a very high concentration at the membrane surface.

The model is related to experimental data. There is a good qualitative and a reasonable quantitative agreement between simulations and experimental data.

*Keywords:*
Rejection coefficient, Membrane separation, CFD, Mathematical modelling, Dextran, Ultrafiltration

## 1. Introduction

Pressure driven, hollow fibre, membranes processes such as ultrafiltration are useful to separate components, i.e., to purify solute. In the membrane process we simulate that the feed solution enters into the hollow fibres and flows in the axial direction. The separation then takes place through each hollow fibre membrane in the radial direction, i.e., similar to cross-flow membranes. The efficiency, however, of the separation process is limited by the increase of solute concentration on the retentate side of the membrane surface, i.e., concentration polarization. The concentration on the retentate side of the membrane surface increases in the axial direction of the hollow fibre because the solute is rejected by the membrane. This, in return, causes the osmotic pressure to increase in the axial direction. Hence, leading to a decrease in solvent flux through the membrane, an increase in solute flux through the membrane, and a decrease in efficiency. The concentration polarization depends on the working parameters of the process, i.e., feed velocity, molecular size of the solute, transmembrane pressure.

Because of the coupling between the flow of the fluid in the bulk on the retentate (and the permeate) side of the membrane, and the flux of the solute and solvent through the membrane, numerous models build upon computational fluid dynamics (CFD) has been used to investigate the effects of concentration polarization [1, 2, 3, 4, 5, 6, 7, 8, 9].

In [4] the Navier - Stokes equation and continuity equation were solved in a crossflow membrane channel. The flux of solvent through the membrane was allowed to be dependent on the concentration on the membrane surface, and the flux of solute to depend on the true rejection, considered constant. The focus, however, was only on the concentration and flow on the retentate side of the membrane.

In [1, 2, 6] a numerical scheme was developed that solved the Navier - Stokes equation for the fluid in the bulk - crossflow membrane channel - with permeation of solvent through the membrane. The model assumed that the solvent flux depended on the pressure and the concentration - through the osmotic pressure - on the membrane surface. Furthermore, they allowed the viscosity to be concentration dependent. However, it is unknown how well this method will work when permeation of

*Corresponding author
*Email addresses:* fravi@dtu.dk (Frank Vinther), mp@kt.dtu.dk (Manuel Pinelo), mobr@dtu.dk (Morten Brøns), gj@kt.dtu.dk (Gunnar Jonsson), am@kt.dk (Anne S. Meyer)
[1]Tel: +45 4525 2950; fax: +45 4588 2258

solute through the membrane is allowed.

To the knowledge of the authors, the influence of both solvent and solute flux through the membrane (without a predetermined intrinsic rejection) is still to be investigated.

In this paper we use the standard numerical tool - Comsol Multiphysics - to solve the model. The model consists of the Navier - Stokes equation, the continuity equation for solvent and solute in the bulk of the hollow fibre. These are coupled to the flux through the membrane of both solute and solvent. Moreover, we allow both the diffusion coefficient and the viscosity to depend on the molecular size of the molecules. This allows us to investigate the effect of working parameters; inlet velocity, molecular size, and transmembrane pressure, on the concentration polarization, the solute and solvent flux, and the true and observed rejection. Furthermore, we allow the viscosity to be concentration dependent. In this paper the working parameters will be varied in the following intervals: the transmembrane pressure will be varied from 0 to 2 bar, the molecular weight in the interval 10 to 500 kDa, and the volumetric flux into the hollow fibre module will be varied from 2 to 6 l/min.

The hollow fibre module considered in this paper consists of 50 hollow fibres. These fibres are bundled together in an inner casing. The inner casing is then situated in an outer casing. The hollow fibre module is shown in figure 1.

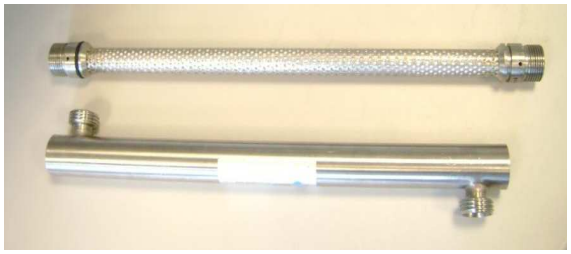

Figure 1: The hollow fibre module that is modelled. At the top the inner casing is seen. Within the inner casing, there are 50 hollow fibres. The inner casing is inserted into the outer casing. A pressure difference is applied from the inside of the hollow fibres (the retentate) to the outside (the permeate). The separation takes place radially through the membrane on the edge of each hollow fibre.

The length of the inner casing is 53 cm. There is an inlet into each hollow fibre where the membrane is impermeable due to the fibres being fixed in an impermeable material. Similarly, there is an outlet where the membrane in each hollow fibre is impermeable. The length of the inlet and the the length of the outlet is 3.5 cm, leaving a length of permeable membrane of 46 cm. The inner radius of each hollow fibre is 0.7 mm.

An illustration of a single hollow fibre in the $rz$-plane is shown in figure 2.

As explained, the separation takes place radially across each hollow fibre membrane due to a pressure difference across the membrane - the transmembrane pressure. The pressure can be measured at the inlet $p_{in}$ and at the outlet $p_{out}$ of the inner casing, and at the outlet of the outer casing, $p_{perm}$. The transmembrane

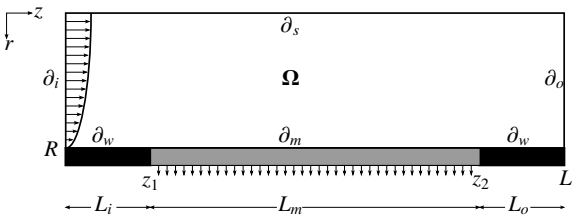


Figure 2: Illustration the hollow fibre tube. The tube has radius $R$ and the permeable membrane is situated between $z_1$ and $z_2$. The impermeable inlet is situated between 0 and $z_1$. And, the impermeable outlet is situated between $z_2$ and $L$.

pressure is defined as

$$p_{TMP} = \frac{p_{in} + p_{out}}{2} - p_{perm}\,. \tag{1}$$

Furthermore, the average velocity, $U_{av}$, at the inlet is known.

Previous studies have reported that the solution-diffusion model can be used to describe the transport of solute during ultrafiltration in case of high intrinsic rejection of solute - in our case higher than the 98% [10]. This can be confirmed by considering the convection term of the Spiegler-Kedem model - which includes terms related to diffusion and convection-, that becomes negligible as compared to the diffusion term for values of the reflection coefficient higher than 0.9 [11]. This indicates that the interaction between solvent and solute at such conditions is negligible, and the transport can be properly explained by the diffusion term. Likewise, it has been demonstrated that for high retention ultrafiltration, the friction model derives into the solution-diffusion model, for identical reasons [12]. Therefore, for high values of the intrinsic rejection, the solution-diffusion model is a good description of the transport of both solute and solvent through the membrane in ultrafiltration, which is one of the assumptions in our study.

In all simulations the solvent is water with a temperature of 295.15 K, a density of $\rho_s = 999.62$ kg/m$^3$, and a shear viscosity of $\eta_s = 0.001$ Pa $\cdot$ s. The solute in all simulations is dextran with different molecular weight.

All simulations are made with Comsol Multiphysics, using only consistent stabilization techniques, i.e., crosswind and streamline diffusion, using the standard values of the parameters.

The mesh used is a mapped mesh. In the axial direction an element size of 0.04 is used. In the radial direction a geometric sequence with 200 elements and an element ratio of 0.0005, with the smallest element size closest to the membrane, is used.

The equations are solved for a total of 15219720 degrees of freedom. Convergence was achieved when the total error was less than $10^{-3}$.

## 2. Mathematical model

We will only consider a single hollow fibre and assume that the separation is the same for each hollow fibre. Furthermore, the pressure on the permeate side of the membrane will be

assumed uniform and equal to $p_{perm}$. The hollow fibre tube will have an inlet, and an outlet, of 3.5 cm where the membrane is impermeable. Moreover, the length of the membrane will be 46 cm. This corresponds to $z_1 = 3.5$cm, $z_2 = 49.5$cm, and $L = 54$cm in figure 2.

### 2.1. Fluxes through the membrane

The flux through the membrane will be given by the solution diffusion model [13].

$$J_v = A\left(\Delta p(z) - \pi(\Delta c(z))\right) \tag{2a}$$

$$J_s = B\Delta c\,. \tag{2b}$$

Here $J_v$ is the solvent flux, $J_s$ is the solute flux, $\Delta p$ is the local transmembrane pressure, $\Delta p(z) = p(R,z) - p_{perm}(z)$. Similarly $\Delta c(z) = c(R,z) - c_{perm}(z)$. As explained the pressure on the permeate side of the membrane will be considered uniform. Hence, $\Delta p(z) = p(R,z) - p_{perm}$. Furthermore, the concentration on the permeate side will be considered small compared to the concentration on the retentate side. I.e, $\Delta c(z) = c(R,z) - c_{perm}(z) \approx c(R,z)$. This is a good approximation when the true, or intrinsic, rejection is high since concentration in the permeate side of the membrane is given by $c_{perm}(z) = (1 - R_{true}(z))c(R,z)$. Thus, equation (2) reduces to

$$J_v = A\left(p(R,z) - p_{perm} - \pi(c(R,z))\right) \tag{3a}$$

$$J_s = Bc(R,z)\,. \tag{3b}$$

The permeability of the solvent depends mainly on the membrane considered. Therefore, the parameter $A$ can vary within a rather large interval in ultrafiltration. In this paper we have chosen the value to be $A = 192\,\mathrm{L/m^2hbar}$. The permeability of solute depends on: the membrane used, the size and shape of the solute molecules, and chemical interactions between solute and membrane [14]. In this paper we have chosen $B = 0.47\,\mathrm{L/hm^2}$. The choice of $A$ and $B$ is, partly, because both are considered within the range used in ultrafiltration [15, 16, 17]. Partly, because previous experiments, available to the authors, have shown similar values of $A$ and $B$ as the ones chosen here.

Throughout this paper the values of $A$ and $B$ will *not* depend on the molecular weight of the solute. We would like to emphasize that this corresponds to membranes having the same characteristics towards both solute and solvent, or membranes having the same intrinsic retention towards solute at a given transmembrane pressure - considering that there is no concentration polarization-.

### 2.2. Osmotic pressure

The osmotic pressure for Dextran has been found in [10] to be given by a third degree polynomial

$$\Pi = A_1 c + A_2 c^2 + A_3 c^3\,, \tag{4}$$

where

$$A_1 = 0.1116\,, \quad A_2 = -0.00491\,, \quad A_3 = 0.000257\,. \tag{5}$$

Here the concentration is given in wt% and the osmotic pressure is measured in atm. As found in [18] the osmotic pressure does not depend on the molecular weight in the case on high concentrations. We will use this expression for the osmotic pressure throughout the paper.

### 2.3. Diffusion coefficient of dextran

The diffusion coefficient depends on the size of the molecules in the solution. Using the Stokes-Einstein relation [19] the diffusion coefficient is

$$D = \frac{k_B T}{6\pi\eta_s R_H}\,, \tag{6}$$

where $k_B$ is Boltzmann's constant, $T$ is the temperature, $\eta_s$ is the viscosity of the solvent, and $R_H$ is the hydraulic radius of the molecule.

Measurements of $R_H$ as a function of average molecular weight for dextran, have been collected from the literature [20, 21, 22, 23, 24]. The diffusion coefficient has been calculated from equation (6), using the temperature of 293.15 Kelvin and the viscosity of water. A relation between the diffusion coefficient and the molecular weight has been found to be

$$D = k_1 M_w^{k_2}\,. \tag{7}$$

Fitting a straight line to the data points in a double logarithmic plot gives the following values for $k_1$ and $k_2$.

$$k_1 = 2.6804 \cdot 10^{-10}\,, \quad k_2 = -0.4754 \tag{8}$$

The data points can be seen in figure 3.

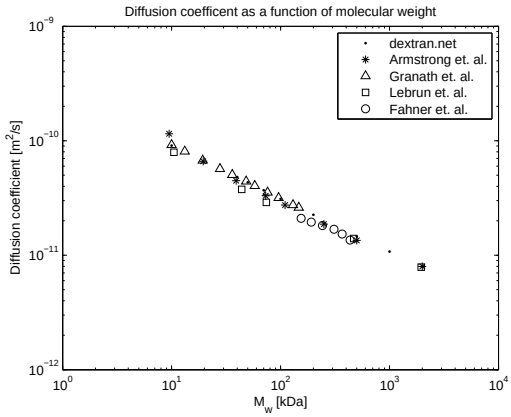


Figure 3: Double logarithmic plot of the diffusion coefficient, calculated using equation (6) and using data of the hydraulic radius found in the literature [20, 21, 22, 23, 24], and the molecular weight.

### 2.4. Equations of motion

Within the bulk of the hollow fibre the equations of motion are the continuity equation of solute and solvent and the momentum equation. The continuity equation for the solvent is

$$\nabla \cdot \boldsymbol{v} = 0\,. \tag{9}$$

The continuity equation for the solute is

$$\boldsymbol{v} \cdot \nabla c = D\nabla^2 c\,, \tag{10}$$

where $D$ is the diffusion coefficient of the solute.

The momentum equation is

$$\rho \boldsymbol{v} \cdot \nabla \boldsymbol{v} = \nabla \cdot \boldsymbol{\Pi}\,, \tag{11}$$

where $\rho$ is the density of the solvent and $\boldsymbol{\Pi}$ is the total stress tensor and is given by

$$\boldsymbol{\Pi} = p\boldsymbol{I} + \eta(c)\left(\nabla \boldsymbol{v} + (\nabla \boldsymbol{v})^T\right)\,, \tag{12}$$

where $\boldsymbol{I}$ is the $3 \times 3$ unit matrix and $\eta(c)$ is the concentration-dependent viscosity of the fluid.

The concentration-dependent viscosity will be given by

$$\eta(c) = \eta_s\left(1 + \alpha_v\left([\eta]\, c + k_H\,[\eta]^2\, c^2\right)\right). \tag{13}$$

Here $\eta_s$ is the viscosity of the solvent and $\alpha_v$ takes the value 0 or 1 and is used to investigate the effect of the viscosity being either constant or concentration dependent. The intrinsic viscosity, $[\eta]$, and the Huggins coefficient, $k_H$, are independent of the concentration.

It is found that the the relation between $[\eta]_0$ and the molecular weight can be given by:

$$[\eta]_0 = K' M_w^a\,, \tag{14}$$

where $K'$ and $a$ will depend on the specific solute and solvent [25]. The parameter $a$ is known as the Mark-Houwink exponent.

From the literature [26, 27, 28, 29] measurements of the intrinsic viscosity are collected. Fitting equation (14) to the data, gives the parameters $K' = 0.0371$ and $a = 0.4352$. The best fit in a double logarithmic plot is shown in figure 4. In [26, 29] the

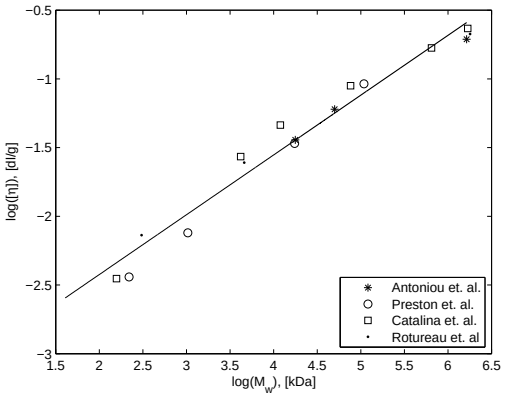


Figure 4: Double logarithmic plot of the intrinsic viscosity as a function of molecular weight along with the best fit through the data.

Huggins coefficient for dextran in water is given to be between 0.495 and 0.58 for molecular weights in the range 10-500 kDa. Therefore, we have chosen $k_H = 0.5$.

Hence, a simple dependence on the viscosity of concentration and molecular weight can be made by combining equation (13) and equation (14).

$$\eta = \eta_s\left(1 + \alpha_v\left(K' M_w^a c + k'\left(K' M_w^a\right)^2 c^2\right)\right). \tag{15}$$

## 3. Boundary conditions

The boundary conditions in the hollow fibre can be divided into five distinctive boundaries.

### 3.1. The inlet

At the inlet of each hollow fibre there is essentially a plug flow with an average velocity $U_{in}$. The flow then gradually develops into a Poiseuille flow. The distance it takes for the flow to develop is given by the hydrodynamic entrance length $L_h$, usually defined as

$$L_h = 0.04 Re_d\,, \tag{16}$$

where $Re_d$ is a Reynolds number defined with the hydraulic diameter as the characteristic length $Re_d = {}^{U_{in} d_h}/_{\nu}$ [30]. For the velocities used in this paper, this corresponds to a hydrodynamic entrance length between 3.4 and 10.1 cm. Therefore, the flow can be considered fully developed at the beginning of the membrane for the lowest inlet velocities, and not fully developed for at most ${}^1/_7$ of the length of the membrane, for the highest inlet velocities. We will, however, assume a fully developed Poiseuille flow at the inlet of each hollow fibre. This is done for three reasons. Firstly, it enables us to give a good estimate for the transmembrane pressure. Secondly, simulations made with a plug-flow and a Poiseuille flow using the same values of the remaining parameters and the largest velocity did not influence the results considerably. Thirdly, the convergence time of the numerical method greatly improved when using a Poiseuille flow as inlet condition. Therefore, at the inlet, $\partial_i = \{r, z\,|z = 0\}$, the boundary condition on the velocity will be a fully developed Poiseuille flow with a known average velocity, $U_{in}$. Hence,

$$\boldsymbol{v}(r, 0) = 2U_{in}\left(1 - \left(\frac{r}{R}\right)^2\right). \tag{17}$$

Furthermore, the boundary condition on the concentration will be uniform and equal to the inlet concentration, i.e.,

$$c(r, 0) = c_{in}\,. \tag{18}$$

### 3.2. The outlet

At the outlet, $\partial_o = \{r, z\,|z = L\}$, there will be a condition on the pressure

$$p(r, L) = p_{out}\,. \tag{19}$$

Moreover, the boundary condition on the concentration will be

$$\nabla c \cdot \boldsymbol{n} = 0 \tag{20}$$

where $\boldsymbol{n}$ is the outward normal vector.

### 3.3. The edge of the hollow fibre

The edge of the hollow fibre $\partial_e = \{r, z\,|r = R\}$ consists of three different domains. The inlet $\partial_w = \{r, z\,|r = R \wedge 0 \leq z < z_1\}$, the membrane $\partial_m = \{r, z\,|r = R \wedge z_1 \leq z \leq z_2\}$, and the outlet $\partial_w = \{r, z\,|r = R \wedge z_2 < z \leq L\}$. At all boundaries $v_z = 0$. At the inlet and the outlet all velocity components are zero. Furthermore, the normal derivative of the concentration is equal to zero, i.e., for $\{r, z\,|r = R \wedge 0 \leq z < z_1\}$ and $\{r, z\,|r = R \wedge z_2 < z \leq L\}$

$$\boldsymbol{v} = 0 \tag{21a}$$

$$\boldsymbol{n} \cdot \nabla c = 0\,. \tag{21b}$$

At the membrane the radial velocity component, $v_r$, is given by the solvent flux, equation (3a), and the concentration flux is given by the solute flux, equation (3b). Thus,

$$\boldsymbol{v}(r, z) \cdot \boldsymbol{n} = A\left(p(R, z) - p_{perm} - \pi(c(R, z))\right) \tag{22a}$$

$$(\boldsymbol{v}(r, z)c(r, z) - D\nabla c(r, z)) \cdot \boldsymbol{n} = Bc(R, z)\,, \tag{22b}$$

where $\boldsymbol{n}$ is the outward unit normal vector.

To avoid discontinuities at $z = z_1$ and $z = z_2$, however, a continuous hat function, $\Psi(z) : z \mapsto [0; 1]$, is introduced. This function has a smooth transition from zero to one around $z_1$ and a smooth transition from 1 to zero around $z_2$. The transition takes place over a length equal to the radius of the hollow fibre, $R$. Hence,

$$\Psi(z) = \begin{cases} 0 & \text{for} \quad 0 \leq z \leq z_1 - R/2 \\ 1 & \text{for} \quad z_1 + R/2 \leq z \leq z_2 - R/2 \\ 0 & \text{for} \quad z_2 + R/2 \leq z \leq L \end{cases}. \tag{23}$$

In the interval $z \in (z_1 - R/2; z_1 + R/2)$ there is a smooth transition from zero to one. Similarly, there is a smooth transition from one to zero in the interval $z \in (z_2 - R/2; z_2 + R/2)$.

With this function the boundary conditions, equation (21) and equation (22), for $\{r, z\,|r = R \wedge 0 \leq z \leq L\}$ can be written as

$$\boldsymbol{v}(r, z) \cdot \boldsymbol{t} = 0 \tag{24a}$$

$$\boldsymbol{v}(r, z) \cdot \boldsymbol{n} = A\left(p(R, z) - p_{perm} - \pi(c(R, z))\right)\Psi(z) \tag{24b}$$

$$(\boldsymbol{v}(r, z)c(r, z) - D\nabla c(r, z)) \cdot \boldsymbol{n} = Bc(R, z)\Psi(z)\,, \tag{24c}$$

where $\boldsymbol{n}$ is the outward unit normal vector, and $\boldsymbol{t}$ the unit vector tangential to the surface.

Taking into account, the high length to radius ratio of the hollow fibre tube, the introduction of the smoothing function $\Psi$, should not influence the results significantly.

### 3.4. Transmembrane pressure

In order to relate the results to a given transmembrane pressure the boundary condition at the outlet $p_{out}$ is calculated assuming that there is a fully developed Poiseuille flow, with the viscosity of the solvent, within the hollow fibre. For a fully developed Poiseuille flow the average velocity can be expressed as

$$U_{in} = \frac{R^2}{8\eta_s}\frac{p_{in} - p_{out}}{L}\,. \tag{25}$$

Hence,

$$p_{in} - p_{out} = \frac{8\eta_s L U_{in}}{R^2}\,. \tag{26}$$

Furthermore, from the definition of the transmembrane pressure, (equation (1)), we have

$$p_{TMP} = \frac{p_{in} + p_{out}}{2} - p_{perm}\,. \tag{27}$$

Combining equation (26) and equation (27) an expression for the pressure at the outlet can be found

$$p_{out} = p_{TMP} + p_{perm} - \frac{4\eta_s L U_{in}}{R^2}\,. \tag{28}$$

This pressure is used as the boundary condition at the outlet, see equation (19).

### 3.5. Observed rejection

The observed rejection is given by the

$$R_{obs} = \left(1 - \frac{\bar{c}_p}{\bar{c}_R}\right)100\%\,. \tag{29}$$

where $\bar{c}_p$ is the average concentration in the permeate after separation and $\bar{c}_R$ is the average concentration in the retentate after separation. The average concentration in the retentate after the separation is given by the ratio between the total solute flux and the total solvent flux

$$\bar{c}_R = \frac{\int_0^R \int_0^{2\pi} r v_z(r, L) c(r, L) d\theta dr}{\int_0^R \int_0^{2\pi} r v_z(r, L) d\theta dr}\,. \tag{30}$$

Similarly, the average concentration on the permeate side is given by the ratio between the total solute flux, and the total solvent flux through the membrane. That is,

$$\bar{c}_p = \frac{\int_0^L \int_0^{2\pi} J_s(z) d\theta dz}{\int_0^L \int_0^{2\pi} J_v(z) d\theta dz} = \frac{\int_0^L \int_0^{2\pi} Bc(z) d\theta dz}{\int_0^L \int_0^{2\pi} v_r(z) d\theta dz}\,. \tag{31}$$

### 3.6. True rejection

The true, or intrinsic, rejection is given by

$$R_{true}(z) = \left(1 - \frac{c_p(z)}{c(R, z)}\right) \cdot 100\%\,. \tag{32}$$

Given that there is a flux of solvent through the membrane, the concentration on the permeate side of the membrane $c_p(z)$ can be written as

$$c_p(z) = \frac{J_s(z)}{J_v(z)} = \frac{B(c(R, z) - c_p(z))}{J_v(z)}\,. \tag{33}$$

Hence, isolating $c_p(z)$ in equation (33)

$$c_p(z) = \frac{Bc(R, z)}{J_v(z) + B}\,. \tag{34}$$

Inserting equation (34) into equation (32) we have

$$R_{true}(z) = \left(1 - \frac{B}{J_v(z) + B}\right) \cdot 100\% = \left(\frac{J_v(z)}{J_v(z) + B}\right) \cdot 100\%\,. \tag{35}$$

Hence, the true rejection in the simulations is given by

$$R_{true}(z) = \left(\frac{v_r(R, z)}{v_r(R, z) + B}\right) \cdot 100\%\,. \tag{36}$$

### 3.7. Non dimensional groups, variables and equations of motion

Introducing the scaled variables

$$\hat{\boldsymbol{x}} = \frac{\boldsymbol{x}}{R}, \quad \hat{\boldsymbol{v}} = \frac{\boldsymbol{v}}{U_{in}}, \quad \hat{p} = \frac{p - p_{perm}}{U_{in}\rho}, \quad \hat{c} = \frac{c}{c_{in}}. \tag{37}$$

The continuity equation of the solvent can be written as

$$\nabla \cdot \hat{\boldsymbol{v}} = 0. \tag{38}$$

The continuity equation of the solvent can be written as

$$\hat{\boldsymbol{v}} \cdot \nabla \hat{c} = \frac{1}{Pe} \nabla^2 \hat{c}, \tag{39}$$

where the Péclet number is given by

$$Pe = \frac{U_{in} R}{D}. \tag{40}$$

The momentum equation can be written as

$$\hat{\boldsymbol{v}} \cdot \nabla \boldsymbol{v} = \nabla \cdot \hat{\boldsymbol{\Pi}}, \tag{41}$$

where, the nondimensional total stress tensor is given by

$$\hat{\boldsymbol{\Pi}} = \hat{p}\boldsymbol{I} + \frac{1}{Re} \hat{\eta}(\hat{c}) \left[ \nabla \hat{\boldsymbol{v}} + (\nabla \hat{\boldsymbol{v}})^T \right]. \tag{42}$$

Here the Reynolds number is defined by

$$Re = \frac{U_{in} R \rho}{\eta_s}, \tag{43}$$

where $\eta_s$ is the viscosity of the solvent. Furthermore, $\hat{\eta}(\hat{c})$ is given by

$$\hat{\eta}(\hat{c}) = 1 + \alpha_v \left( K' M_w^a c_{in} \hat{c} + k' \left( K' M_w^a \right)^2 c_{in}^2 \hat{c}^2 \right) \tag{44}$$

## 4. Results

In section 4.1 and 4.2 the viscosity is considered independent of the concentration, i.e, $\alpha_v = 0$. In section 4.3 and 4.4 we allow the viscosity to depend on the concentration, i.e., $\alpha_v = 1$.

### 4.1. Influence of Péclet and Reynolds numbers on the concentration of solute on the membrane surface

In figure 5 the concentration on the membrane surface is shown for different Péclet numbers, i.e., different molecular weight. In figure 5 the dimensionless concentration at the inlet, $\hat{z} = 0$, is 1. As the fluid reaches the permeable membrane a sharp increase in concentration is observed due to the separation. Similarly, there is a sharp decrease in the concentration as the hollow fibre tube becomes impermeable. This sharp decrease in concentration is caused by back diffusion into the bulk of the fluid. This is also observed in [1, 2, 6]

As the molecular weight increases, the diffusion coefficient decreases according to equation (7). Therefore, the larger the molecular weight, the smaller the back diffusion along the membrane surface, leading to an increased concentration on the membrane surface.

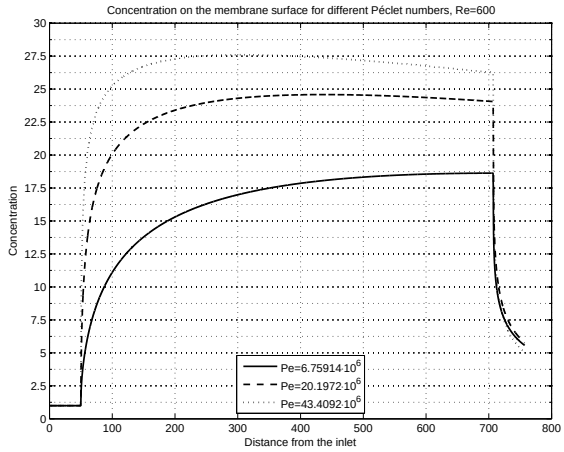


Figure 5: Concentration on the membrane surface for different Péclet numbers. The Péclet numbers corresponds to an average volumetric flux into the hollow fibre module of 4 l/min ($Re$ = 600) and molecular weights of 10, 100, and 500 KDa.

In figure 6 the concentration on the boundary of the hollow fibre is shown for different Reynolds numbers. The Reynolds numbers corresponds to an average volumetric flux into the hollow fibre module of 2, 4, and 6 l/min. The molecular weight in this particular simulation is 100 kDa.

As seen in figure 6 the concentration on the membrane surface decreases as the Reynolds number increases. Similar results are observed in [3, 5]. This is usually explained as an increasing self-cleaning of the membrane, due to the increased tangential velocity in the boundary layer. Another explanation commonly used is that an increase in Reynolds number leads to an increase in turbulence in the boundary layer, which in return gives rise to a self cleaning. However, turbulence is not a part of this model and the flow is laminar. Therefore, the reduced concentration on the membrane surface is not caused by turbulence. Our hypothesis is that the reduced concentration is caused by the change in the streamlines, see e.g. [31]. At a given Reynolds number the streamline for a fluid parcel with inlet point $(\hat{r}, \hat{z}) = (\hat{r}^*, 0)$, where $0 < \hat{r}^* < 1$ will end at the membrane surface at a point $(\hat{r}, \hat{z}) = (0, \hat{z}^*)$. An increase in Reynolds number will cause a streamline with the same inlet point to end at a point further down the membrane, i.e, at a point $(\hat{r}, \hat{z}) = (0, \hat{z}^{**})$, where $\hat{z}^* < \hat{z}^{**}$. Hence, the larger the Reynolds number the less of the fluid is transported to a given part of the membrane, resulting in both a decrease of concentration on the membrane surface, and a less sharp increase in concentration at the beginning of the membrane. Both effects are seen in figure 6.

In figure 7 the true rejection is shown for the same set of parameters as used in figure 5. Since the true rejection, equation (36), is only properly defined when the flux through the membrane is different from zero, it is only shown along the membrane surface. As seen in figure 7 the true rejection is highest for small molecular weight, small Péclet numbers. This is due to the higher back-diffusion from the membrane. Because

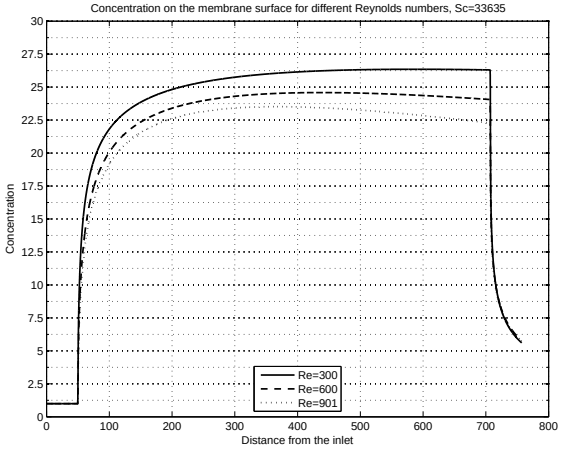


Figure 6: Concentration on membrane surface for different Reynold numbers.

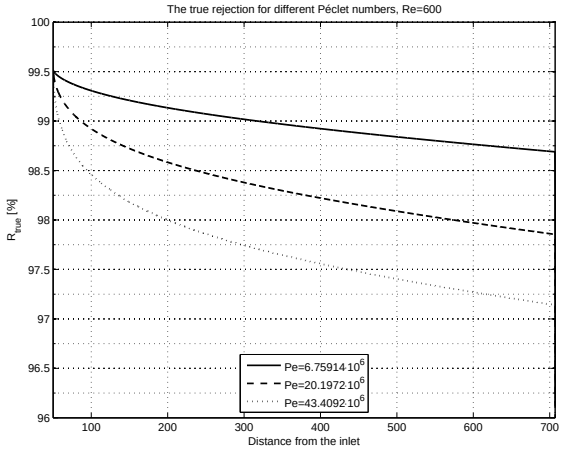


Figure 7: True rejection for different Péclet numbers. The Péclet numbers corresponds to an average volumetric flux into the hollow fibre module of 4 l/min and molecular weights of 10, 100, and 500 KDa.

a high concentration on the membrane surface reduces the flux through the membrane due to an increased osmotic pressure, the true rejection decreases.

In figure 8 the true rejection is shown for different Reynolds numbers. As before, the true rejection increases when the concentration on the membrane surface decreases. Hence, the true rejection is highest for large Reynolds numbers.

In figure 9 the observed rejection is shown for the parameters used in the previous figures. As seen the observed rejection is highest for the smaller molecules, at the same Reynolds number, and increases with increasing Reynolds number. Again this effect is ascribed to the concentration polarization on the membrane surface. A large concentration on the membrane surface increases the solute flux through the membrane and reduces the solvent flux through the membrane. Both lead to a higher concentration in the permeate.

### *4.2. Influence of different transmembrane pressures*

In figure 10 the concentration on the membrane surface is shown for different transmembrane pressures. The transmembrane pressures are 0.5, 1, and 2 bar. Moreover, the molecular weight used in the simulation is 110 kDa and the volumetric flux into the hollow fibre module is 6 l/min. As seen, in figure 10, the concentration on the membrane surface increases when the transmembrane pressure increases. The increase in concentration is caused by an increase in advection towards the membrane surface due to the increase in transmembrane pressure. This effect is also observed in [2, 6].

In figure 11 the true rejection is shown for the same transmembrane pressures. As seen, the true rejection increases as a function of transmembrane pressure. Hence, even though the concentration on the membrane surface increases, and thus, the osmotic pressure increases, the solvent flux through the membrane still increases.

The effect on the observed rejection for different transmembrane pressures and different molecular weights are shown in figure 12. Again the different transmembrane pressures are 0.5, 1, and 2 bar. The molecular weights used in the simulations are 10, 110, and 500 kDa. Furthermore, the volumetric flux into the hollow fibre module is 6 l/min. As seen, in figure 12, the observed rejection is decreasing as a function of transmembrane pressure for the different molecular weights. This reduction is caused by the interplay between the solute flux and the solvent flux. From figure 11 we can infer that the solvent flux through the membrane is increasing as a function of the transmembrane pressure. In figure 10, however, it is seen that the concentration on the membrane surface also increases, leading to an increasing solute flux through the membrane. From figure 12 and the definition of the true rejection, equation (29), it can be concluded that, within the interval of molecular weight and transmembrane pressure used in these simulations, the ratio between the total solute flux and the total solvent flux is increasing when the Péclet number is decreased, the pressure is increased, or both.

The observed rejection, however, will be zero for very low transmembrane pressures. Therefore, there must be an interval of transmembrane pressure where the observed rejection is increasing. This will be investigated in more detail in section 4.4.

### *4.3. Influence of concentration dependent viscosity*

In this section we present simulations where the viscosity is concentration dependent, i.e., $\alpha_v = 1$ in equation (44). Using the same working parameters, these simulations will be compared to simulations where the viscosity is independent of the concentration, i.e, $\alpha_v = 0$ in equation (44).

In figure 13 the concentration on the membrane surface is shown for different Reynolds numbers, a transmembrane pressure of 0.5 bar, and a molecular weight of 10 kDa. As seen, in figure 13, the concentration on the membrane surface increases when the viscosity is concentration dependent. This increase can

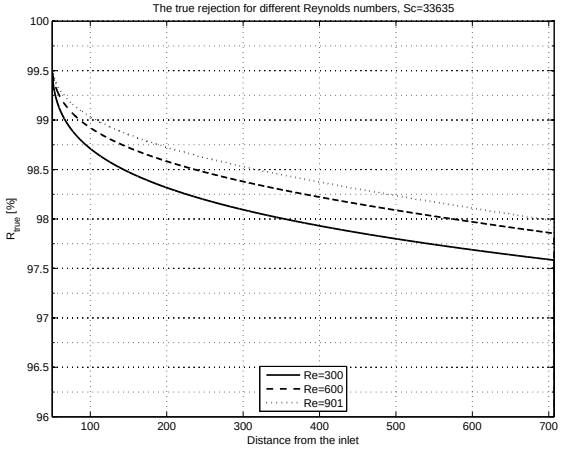


Figure 8: True rejection for different Reynolds numbers but constant Schmidt number.

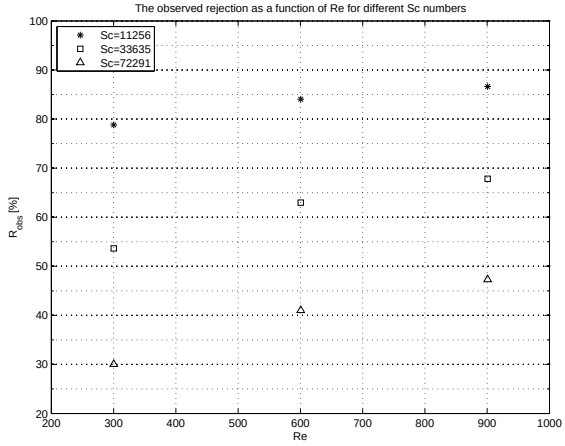


Figure 9: Observed rejection for different values of Reynolds number and Schmidt number.

be explained by a decrease in axial velocity within the boundary layer. The decrease in axial velocity perpendicular to the membrane surface is shown, halfway down the membrane, for molecular weights of 10 and 500 kDa, in figure 14. The decrease in axial velocity close to the membrane surface is more obvious for large molecules. This is due to both the smaller back diffusion which cause a larger concentration in the boundary layer and the increased dependence of the viscosity for the larger molecules.

In figure 15 the concentration perpendicular to the membrane surface is shown halfway down the membrane. As seen, the introduction of a concentration dependence on the viscosity both increase the concentration on the membrane surface and increase the width of the boundary layer. Both effects are more obvious for the larger molecules. For the larger molecules, an increase in concentration to 30 times the inlet concentration corresponds to an increase in viscosity by a factor of 6.4, as compared to the solvent viscosity. Similar results are found in [2, 1].

Thus, introducing a concentration dependent viscosity increases the concentration on the membrane surface. Therefore, the solvent flux trough the membrane will decrease and reduce the true rejection. Furthermore, the solute flux will increase as the concentration on the membrane surface increases. Thus, the observed rejection decreases. The decrease in observed rejection is shown in figure 16. This effect is more obvious for larger molecules because of the higher concentration dependence on the viscosity and the higher concentration in the boundary layer caused by the smaller back diffusion.

### *4.4. Observed rejection for different transmembrane pressures and different values of B*

As mentioned previously, the observed rejection has to be increasing an function of the transmembrane pressure in a certain interval. Furthermore, the value of the parameter $B$ will have a huge effect on the observed rejection. In this section we therefore present the observed rejection as a function of transmembrane pressure in the interval $p_{TMP} \in [0, 2]$ bar. Moreover, we present the results for three different values of $B$. Namely, $B = 0.47, 0.047, 0.0047 \text{l/h}\cdot\text{m}^2$. Furthermore, we present the results with and without a concentration dependent viscosity.

In figure 17 the observed rejection is shown for different transmembrane pressures. As seen the effect of decreasing the value of the parameter $B$ is to increase the observed rejection. This is simply because of the smaller sorption of solute into the membrane, or the smaller diffusion of solute through the membrane, or both - increasing the membranes capability of retaining the solute particles. Furthermore, it is seen that introducing a concentration dependent viscosity reduces the observed rejection. This effect increases as the transmembrane pressure increases due to the increasing concentration on the membrane surface.

As expected the observed rejection is increasing for very small values of the transmembrane pressure. At these low pressures the advective transport towards the membrane is so small that there is no significant boundary layer. As the transmembrane pressure increases, however, the concentration on the membrane surface increases rapidly causing the osmotic pressure and the solute flux to increase. The increase osmotic pressure and in solute flux reduces the observed rejection.

In figure 18 the observed rejection is plotted against the volumetric flux through the membrane.

As seen for low values of the parameter $B$ the volumetric flux through the membrane decreases rapidly for high transmembrane pressures. This is due to of the high concentration polarization caused by the high retention of the membrane, leading to a high osmotic pressure.

### *4.5. Relating the model to experimental results*

Using the experimental hollow fibre module, mentioned in the introduction, a set of experiments at different pressures have been performed.

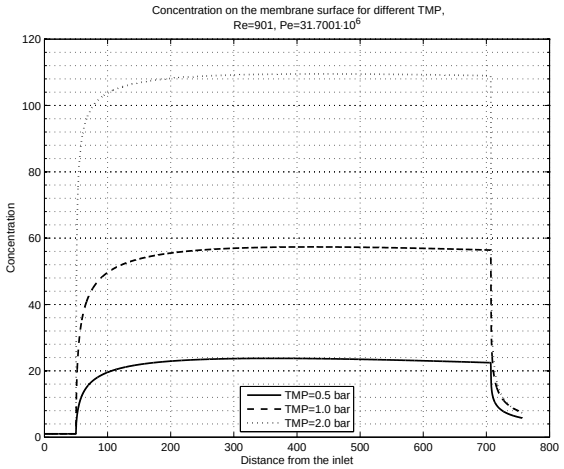


Figure 10: Concentration on the membrane for different transmembrane pressures. The Reynolds number corresponds to a volumetric flux into the entire module of 6 l/min. The Péclet number corresponds to a molecular weight of 110 kDa.

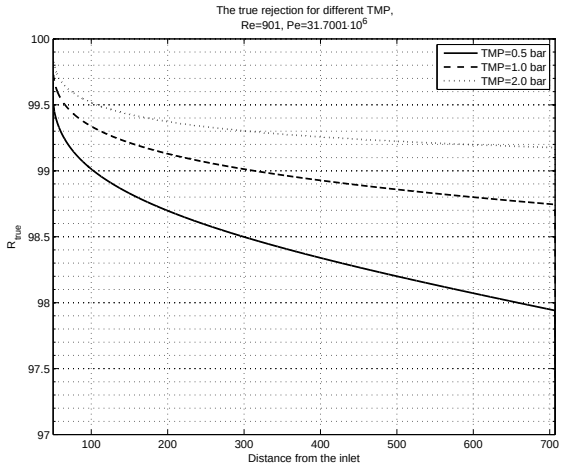


Figure 11: True rejection for different transmembrane pressures. The Reynolds number corresponds to an inlet velocity to the hollow fibre module of 6 l/min. The Péclet number corresponds to a molecular weight of 110 kDa.

The experiments were performed using an UFM membrane from X-Flow, with a water permeability $A = 245.65^{\mathrm{L}}/_{\mathrm{m^2hbar}}$. The solute was dextran T500 and the solvent was water. In all experiments the volumetric flux through the inlet was 3.87 l/min. For each experiment the concentration in the feed solution, $c_f$, was measured. Moreover, the concentration in the permeate was measured. For each experiment the separation took place for approximately 50 seconds until steady state was obtained. The five experiments were performed at five different pressures. The observed rejection $S$, was calculated from

$$S = \left(1 - \frac{\bar{c}_p}{c_f}\right) \cdot 100\% \,. \tag{45}$$

The results of the experiments are presented in table 1.

| Exp i | $p_{TMP}$ [bar] | $\bar{J}_v$ [$^{\mathrm{L}}/_{\mathrm{m^2h}}$] | $c_f$ [wt%] | $\bar{c}_p$ [wt%] | $S$ [%] |
|---|---|---|---|---|---|
| 1 | 0.51 | 31.54 | 0.1452 | 0.0508 | 64.97 |
| 2 | 0.74 | 35.04 | 0.1414 | 0.0700 | 50.46 |
| 3 | 1.00 | 41.77 | 0.1389 | 0.0968 | 30.36 |
| 4 | 1.23 | 48.01 | 0.1381 | 0.1072 | 22.39 |
| 5 | 2.10 | 53.64 | 0.1367 | 0.1139 | 16.71 |

Table 1: Experimental data.

From the data presented in table 1 it is possible to give an estimate of the parameter $B$.

*4.5.1. Estimation of B*

In order to calculate the value of B, we used the following method:

The concentration difference across the membrane is approximated by a constant concentration on the membrane surface, $\hat{c}_m$. Thus, $\hat{c}_m - \bar{c}_{p,m} \approx \hat{c}_m$

Hence, for each experiment, denoted by subscript $i$, $\bar{J}_v$ is given by

$$\bar{J}_{v,i} = A\left(p_{TMP,i} - \pi(\hat{c}_{m,i})\right) \,, \tag{46}$$

where $\hat{c}_{m,i}$ is the constant concentration on the membrane surface and $\pi(\hat{c}_{m,i})$ is the osmotic pressure given by equation (4). From equation (46) $\hat{c}_{m,i}$ can be calculated as

$$\hat{c}_{m,i} = \pi^{-1}\left(p_{TMP,i} - \frac{\bar{J}_{v,i}}{A}\right) . \tag{47}$$

The average concentration in the permeate, $\bar{c}_{p,i}$ can be given by the ratio between the solute and solvent flux or expressed in terms of the observed rejection. I.e,

$$\bar{c}_{p,i} = \frac{B_i \hat{c}_{m,i}}{\bar{J}_{v,i}} = (1 - S_i)\,\bar{c}_{in,i} \tag{48}$$

Solving equation (48) for $B_i$, one has

$$B_i = \frac{(1 - S_i)\,\bar{c}_{in,i}\bar{J}_{v,i}}{\hat{c}_{m,i}} = \frac{(1 - S_i)\,\bar{c}_{in,i}\bar{J}_{v,i}}{\pi^{-1}\left(p_{TMP,i} - \frac{\bar{J}_{v,i}}{A}\right)} \,. \tag{49}$$

Using the data from table 1, values for $\hat{c}_m$ and $B$ are estimated in table 2.

| Exp. | $\hat{c}_m$ [Wt%] | B [$^{\mathrm{l}}/_{\mathrm{m^2h}}$] |
|---|---|---|
| 1 | 3.8811 | 0.4132 |
| 2 | 9.3145 | 0.4339 |
| 3 | 6.4406 | 0.3811 |
| 4 | 11.4333 | 0.4500 |
| 5 | 17.6737 | 0.3457 |

Table 2: Calculated values of $\hat{c}_m$ and $B$.

In order to simulate this specific experiment a single value for the inlet concentration and $B$ is needed. Therefore, the average

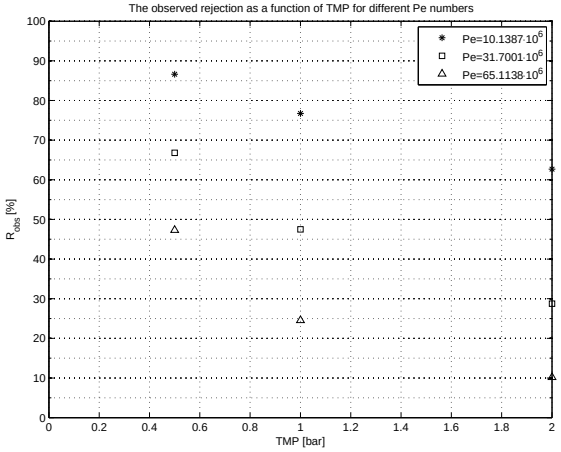


Figure 12: Observed rejection for different transmembrane pressures. The Reynolds number corresponds to an inlet velocity to the entire module of 6 l/min. The Péclet numbers corresponds to molecular weights of 10, 110, and 500 kDa.

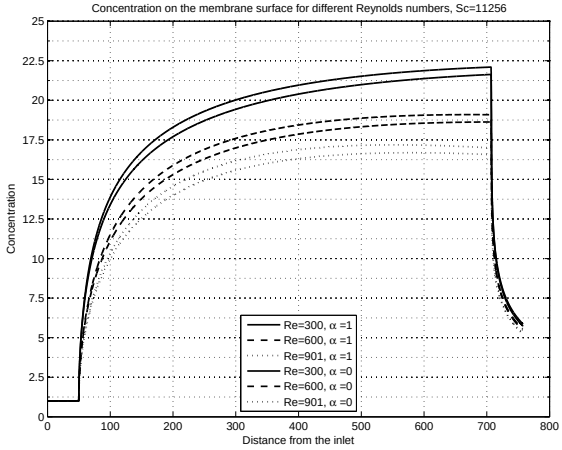


Figure 13: Concentration on the membrane surface for different Reynolds numbers. The Reynolds numbers correspond to an inlet velocity in the entire module of 2, 4, and 6 l/min. The Schmidt number correspond to a molecular weight of 10 kDa. The transmembrane pressure is 0.5 bar. The blue lines corresponds to the viscosity being constant and equal to the solvent viscosity. The black lines corresponds to the viscosity being concentration dependent.

of the above values is chosen, i.e., $c_{in,av}$ = 0.1401 [Wt%] and $B_{av}$ = 0.4048 [l/m²h].

Hence, the values of $A$ and $B$ deviates slightly from the values used in the previous sections.

*4.5.2. Comparison between experiment and simulations*

Using the parameters given in the previous section we present the results from the simulations, as well as the experimental results in this section.

In figure 19 the volumetric flux through the membrane is shown together with the experimental results. As seen there is a good agreement between the experiment and the simulation.

In figure 20 the permeate concentration is shown for the simulations and the experiments. As seen the concentration in permeate is lower in the experiments than in the simulations.

In figure 21 the observed rejection is shown. As seen from the figure the observed rejection is lower in the simulations than in the experiments.

The main reason for the deviation from the experiments is the determination of $B$ using the approximation that the concentration on the membrane surface is constant. The concentration on the membrane surface depends on the axial position. Therefore, the parameter $B$ should be determined by a least error fit. This, however, is beyond the scope of the current paper.

Nevertheless, there is a good qualitative agreement between the experiment and the simulations, and a reasonable quantitative agreement.

## 5. Discussion

Back diffusion of solute from the membrane surface to the bulk decreased for increasing molecular weights (increasing Péclet numbers), which resulted in higher concentrations of solute on the membrane surface (Figure 5). Albeit the differences in concentration were obvious for different Péclet numbers, such concentration varied along the length of the membrane. After an initial sharp increase, a maximal, almost stable value of solute concentration along the remaining length of the membrane was observed. Such trend has been reported to be typical in cross flow filtrations in which the variation of solute concentration and diffusive transport along the tangential direction can be assumed to be small [32].

Considering the important role of the molecular diffusion of solute particles to the bulk solution, the clear influence of the Reynolds number on the solute concentration on the membrane surface was expected (Figure 6). The higher the axial velocity (high Reynolds numbers), the lower was the solute concentration on the membrane surface.

Solute concentration on the membrane surface plays a major role for the total performance of the membrane, as selectivity, retention and flux through the membrane are directly dependent. The ratio between solute concentration on the membrane surface and solute concentration in the permeate (true retention) depends on both the flux of solvent and the solute through the membrane. Higher Péclet numbers contributed to decrease the permeate flux, which resulted in a reduction of true retention along the length of the membrane (Figure 7). The effect of decreasing true retention due to low permeate fluxes was more obvious when Reynolds numbers decreased (Figure 8). High Reynolds numbers contributed to increase the permeate flux, which in turn contributed to increase the true retention - due to the decrease in the permeate concentration. The increasing values of true retention for increasing cross-flow velocities was also reported for cross-flow filtration of aqueous solutions of PEGs through polyamide ultrafiltration membranes [33].

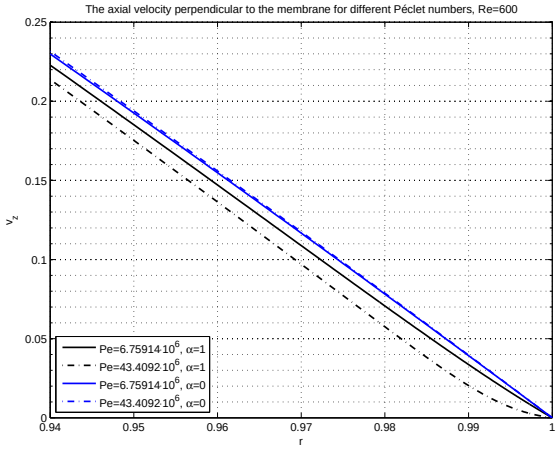


Figure 14: Axial velocity in the boundary layer, perpendicular to the membrane surface half way down the hollow fibre, for different Péclet numbers. The Reynolds number corresponds to an inlet velocity in the entire module of 4 l/min. The Péclet numbers corresponds to a molecular weight of 10 and 500 kDa. The transmembrane pressure is 0.5 bar. The blue lines corresponds to the viscosity being constant and equal to the solvent viscosity. The black lines corresponds to the viscosity being concentration dependent.

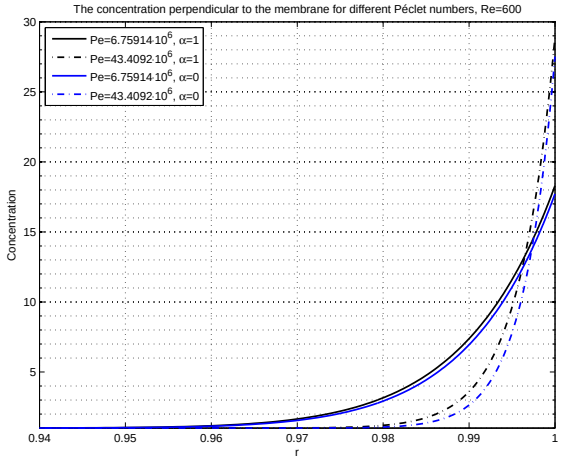


Figure 15: Concentration in the boundary layer, perpendicular to the membrane surface half way down the hollow fibre, for different Péclet numbers. The Reynolds numbers corresponds to an inlet velocity in the entire module of 4 l/min. The Péclet numbers corresponds to a molecular weight of 10 and 500 kDa. The transmembrane pressure is 0.5 bar. The blue lines corresponds to the viscosity being constant and equal to the solvent viscosity. Whereas, the black lines corresponds to the viscosity being concentration dependent.

### *5.1. True versus observed retention: Influence of transmembrane pressure*

The values of observed retention in the simulation were lower than the ones corresponding to true retention (Figure 9). This was explained by two phenomena that take place when the concentration of solute on the membrane surface increases. On one hand, high solute concentrations decreases the solvent flux through the membrane, which contributes to increase the solute concentration in the permeate. On the other hand, high concentrations of solute favours the diffusion of solute through the membrane, which contributes to enhance the solute concentration in the permeate. These phenomena explains the lower values of observed retention, for low Reynolds numbers, or high Péclet numbers, or both.

There are many examples in literature reporting the effect of decreasing observed retention, particularly for increasing values of transmembrane pressure or permeate flux - as observed in our simulations (Figure 12). For instance, a sharp decrease in the observed retention was observed during ultrafiltration of dextran and PEG when permeate flux increased, and the decrease was more dramatic for higher values of molecular weight [34]. The decreasing observed retention trend has been also reported for other molecules with quite different chemically e.g. copolymers of dimethyl aminoethyl acrylate (CoAA) or humic acid [35]. The latter study also confirmed that such effect does not seem to depend much either on the membrane material - in this particular case polyethersulfone and cellulose - what make us infer that it is mainly the difference of solute concentration on both sides of the membrane that is controlling this phenomenon, beyond the possible chemical or physical interactions between the solute and membrane material. To this regard, it has been reported that the decrease in observed retention can also occur for ionic solutes [36]. The differences between true and observed retention have been previously explained on the basis of convection and diffusion, the two phenomena that determines the values of Péclet number. Whilst for low Péclet numbers (small solute and large diffusion) the retention is low and both the true and the observed retention follow the same tendency, for high Péclet numbers, the convection and concentration polarization become more important. As a consequence, the concentration on the surface of the membrane increases (low true retention), and the pass of solute through the membrane causes the solute concentration in the permeate to increase, which in turn results in a decrease of the observed retention [37].

### *5.2. Effect of Viscosity*

While the axial velocity or transmembrane pressure have a noticeable effect on the solute concentration on the membrane surface, the physical-chemical properties inherent to the nature of the solute molecules, particularly viscosity, can also influence to a great extent the performance of the membrane in terms of retention. When the variation of viscosity for increasing dextran concentrations was considered in the simulations, an increase of solute concentration on the membrane surface was observed (Figure 13). The higher the molecular weight of the dextran considered, the more dramatic was the increase of viscosity for increasing concentrations, which in turn resulted in higher solute concentrations on the membrane surface (data not shown).

The dependence of viscosity with solute concentration is a common phenomenon which depends on both the molecular weight of the solute and the chemical features of the molecule. For instance, it has been reported an increase of viscosity of 1.7

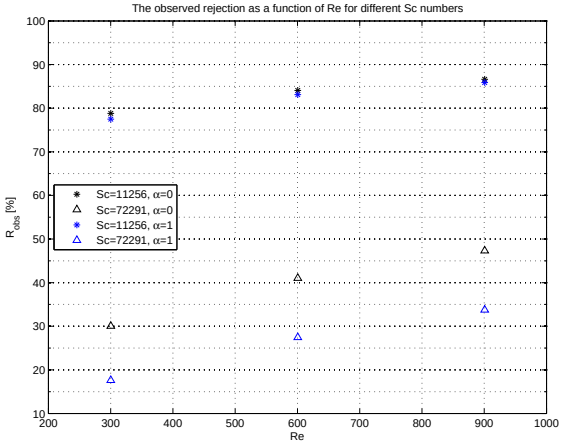


Figure 16: Observed rejection for different Schmidt and Reynolds numbers. The Reynolds numbers corresponds to an inlet velocity in the entire module of 2, 4, and 6 l/min. The Schmidt numbers corresponds to a molecular weight of 10 and 500 kDa. The transmembrane pressure is 0.5 bar. The blue markers corresponds to the viscosity being constant and equal to the solvent viscosity. Whereas, the black markers corresponds to the viscosity being concentration dependent.

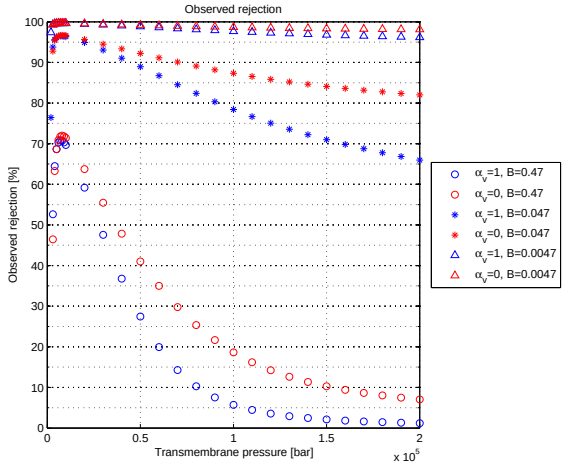


Figure 17: Observed rejection as a function of transmembrane pressure for three different values of B. For each value of B the red symbols corresponds to a constant viscosity. Whereas, thee blue symbols corresponds to a concentration dependent viscosity.

and 2.7 times when solutions of sucrose and BSA were concentrated 20 times, respectively. For the same increase of concentration, the viscosity of a dextran solution increased 29.2 times [38]. Other studies have also found that the increase of solute concentration on the membrane is dependent on time, increasing as time passes, until a certain concentration is reached at steady state [39]. A previous study has compared the solute concentration on the membrane surface for different solutions of sucrose - 0.2, 2, and 4%- concluding that the concentration-dependent viscosity has a higher influence on the solute concentration than the concentration-dependent diffusivity, which results in an increase of such concentration [40].

Viscosity increases, besides causing increases of solute concentration on the membrane surface, also resulted in increases in the thickness of the boundary layer. This effect was more prominent for larger molecular weight solutes (Figure 15). Therefore, it could be said that the effect of considering a viscosity that depends on concentration is similar to the effect of decreasing the axial velocity or the Reynolds number. To this regard, significant increases of permeate flux for increasing axial velocities during filtration of Dextran T20 have been reported, which demonstrated that high axial velocities contributed to sweep off the layer of solute formed on the surface of the membrane. For low values of axial velocity, the permeate flux attained a stable value that was independent of the transmembrane pressure for high values of pressure - limiting flux [10].

Although such behaviour could in principle be explained by the formation of a constant gelling concentration, a previous study based on a simulation of dextran ultrafiltration at different applied pressures demonstrated that even if the solute concentration on the membrane surface increases and the permeate velocity decreases along the crossflow (due to viscosity increases), reaching a limiting flux does not necessarily mean a constant solute concentration on the membrane surface [6]. This suggests that the solute concentration on the membrane surface always increases, at least in the case of dextran, but that there are other factors influencing the permeate flux.

Since the permeate flux through the membrane decreased when the viscosity became concentration-dependent, the true retention is also expected to decrease. Along with the decrease in permeate flux, the solute flux is assumed to increase - due to the increased concentration on the membrane surface- which in turn resulted in reductions of the observed retention (Figure 16).

### *5.3. Effect of solute permeability coefficient (B)*

The solute permeability coefficient, which is directly dependent on the sorption and diffusivity of solute through the membrane, had a significant effect on the values of the observed retention (Figure 17). Higher values of B meant lower values of solute concentration on the membrane surface (high sorption) and easy diffusion of solute through the membrane, which resulted in increases of solute concentration in the permeate - and thus lower observed retentions.

Whilst the solvent permeability coefficient $A$, is characteristic of the membrane used, $B$ values can be modified by changing the membrane material, as both sorption and diffusion depend on the physical-chemical affinity between membrane material and solute nature. Even for solutes with same molecular weight, values of $B$ can change dramatically depending on the chemical nature of the solute [41, 42]. Therefore, depending on the application, the observed retention can be tailored in order to obtain more or less solute in the permeate. Hence, a careful selection of the membrane material will have a direct effect on the retention of a particular solute.

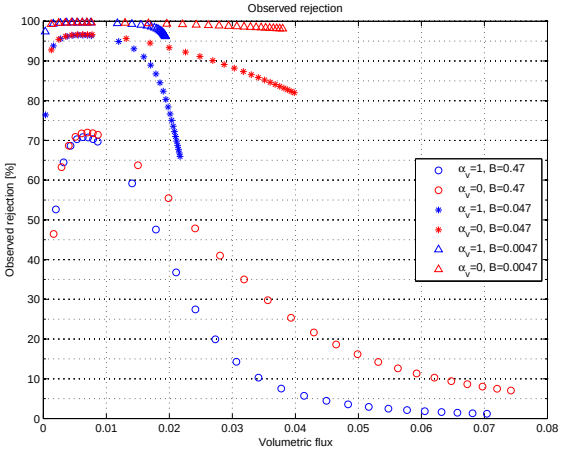


Figure 18: Observed rejection as a function of the non-dimensional volumetric flux through the membrane for three different values of B. For each value of B the red symbols corresponds to a constant viscosity. Whereas, the blue symbols corresponds to a concentration dependent viscosity.

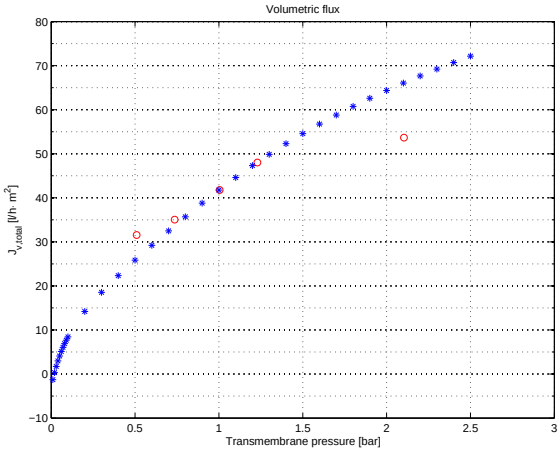


Figure 19: Volumetric flux through the membrane. Red circles corresponds to experimental data and blue stars corresponds to numerical simulations.

It is also necessary to mention that values of $B$ will normally decrease during filtration, particularly in cases in which a deposited gel/polarized layer is formed as a consequence of concentration polarization and fouling. In those cases, the formed layer acted as a secondary membrane layer, modifying the sorption and diffusion capacity of the solute through the membrane [9]. As a result, observed retention values are expected to increase.

For extreme cases in which $B$ attains a very low value - so solute transport through the membrane is very small- and the transmembrane pressure is high (Figure 18), the concentration in the boundary layer caused the viscosity to be so high that the volumetric flux almost ceased to increase. In the case of the highest transmembrane pressure and the smallest value of $B$, the viscosity at the membrane surface increases to 60 times the viscosity of the pure solvent. In this limit the concentration dependent viscosity forms a gel layer where the self cleaning of the membrane is almost negligible. This caused the volumetric flux through the membrane to have almost half the value when comparing a concentration dependent viscosity to a constant viscosity. Moreover, this tendency seemed to increase even further when the transmembrane pressure was increased even more.

### *5.4. Relating the model to experiment*

The model was examined against an experiment made with the hollow fibre module. The results showed a good qualitative agreement and a reasonable quantitative agreement with these data. The quantitative agreement, however, showed that the concentration in the permeate was higher in the simulations than observed in the experiments. This resulted in a lower observed rejection in the simulations than observed in the experiments.

The parameter $B$ was determined assuming a constant concentration on the membrane surface of each hollow fibre. This assumption is obviously not valid and the parameter $B$ should

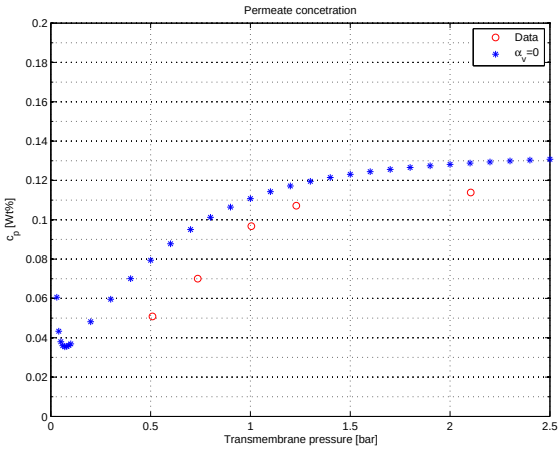


Figure 20: Concentration in the permeate. Red circles corresponds to experimental data and blue stars corresponds to numerical simulations.

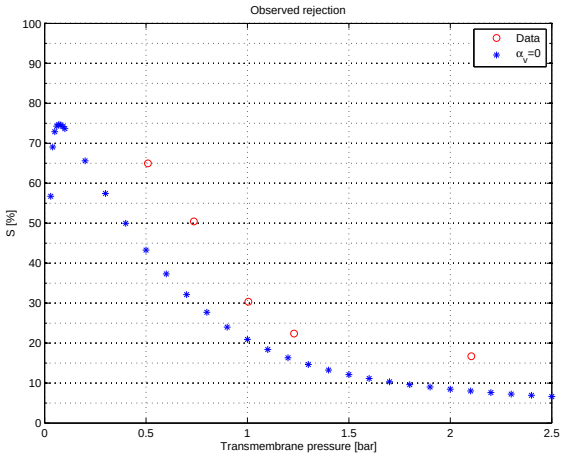


Figure 21: Observed rejection for both the experiments and the simulations. Red circles corresponds to experimental data and blue stars corresponds to numerical simulations.

be fitted to each particular experiment. It is the belief of the authors that a finer 'tuning' of $B$ would give simulations that can reproduce the observed rejection better. From the investigation of the parameter $B$, figure 17, it is seen that a smaller value of $B$, results in a higher observed rejection.

There are, however, other quantities that influence the results of the simulations. The virial coefficients in the expression for the osmotic pressure have been observed to depend on the molecular weight [43]. The osmotic pressure will effect both the solvent flux and the solute flux and thereby the observed rejection.

Moreover, it is well known that the solvent flux time is dependent - decreasing with time [9]. Therefore, the steady state will have a lower retention than in the beginning of the experiments. Thus, the steady state solution, give rise to a lower observed rejection than the experiment.

## 6. Conclusions

In this paper we presented a mathematical model capable of modelling the velocity field, concentration field, and pressure field in the bulk solution of a hollow fibre tube. The model was able to model both solvent and solute flux through membrane.

This has allowed us to investigate the effect, on the true rejection and the observed rejection, of the working parameters: inlet velocity, molecular size, and transmembrane pressure, for a given set of membrane parameters typical for ultrafiltration of polysaccharides.

It can be concluded that an increasing inlet velocity decreases the concentration on the membrane surface, due to a higher axial velocity. This in return, increases both the true and the observed rejection.

An increase in molecular weight resulted in an increase in concentration on the membrane surface, due to a lower backdiffusion. This in return, decreased both the true and the observed rejection.

An increase in transmembrane pressure gave rise to a higher solvent flux through the membrane and a higher concentration on the membrane surface. The increase in solvent flux, resulted in an increase in true rejection. Since, both the solute flux and the solvent flux increased, the concentration in the permeate, defined as the ratio between the two, had two distinct behaviours. At low transmembrane pressure an increase in transmembrane pressure resulted in a relative increase in solvent flux as compared to solute flux, which led to an increased observed rejection. For larger transmembrane pressure, an increase in transmembrane pressure led to an increasing solute flux as compared to solvent flux, resulting in a decrease in observed rejection. The decrease in observed rejection for high transmembrane pressures must be ascribed by the high increase in concentration polarization and osmotic pressure.

Decreasing the coefficient determining the solute permeability, $B$, led to an increase in observed rejection. Furthermore, it led to a decrease in solvent flux due to an increased concentration on the membrane surface.

In all cases, a concentration dependent viscosity, decreased both the true and the observed rejection. The reason being a decrease in tangential velocity near the membrane.

The model was related to experimental data. The simulations showed a good qualitative agreement and a reasonable quantitative agreement.


[1] P. Henriksen, O. Hassager, Simulation of transport phenomena in ultrafiltration, Chemical Engineering Science 48 (1993) 2983 – 2999.

[2] M. Hansen, V. A. Barker, O. Hassager, Spectral element simulation of ultrafiltration, Chemical Engineering Science 53 (1998) 3099 – 3115.

[3] J. Miranda, J. Campos, Numerical study of a hybrid membrane cell with semi and fully permeable membrane sub-sections, Chemical Engineering Science 62 (2007) 1215 – 1229.

[4] D. E. Wiley, D. F. Fletcher, Techniques for computational fluid dynamics modelling of flow in membrane channels, Journal of Membrane Science 211 (2003) 127 – 137.

[5] A. Ahmad, M. Chong, S. Bhatia, Mathematical modeling and simulation of the multiple solutes system for nanofiltration process, Journal of Membrane Science 253 (2005) 103 – 115.

[6] S. Ma, S. C. Kassinos, D. Kassinos, Direct simulation of the limiting flux: I. interpretation of the experimental results, Journal of Membrane Science 337 (2009) 81 – 91.

[7] M. Rahimi, S. Madaeni, M. Abolhasani, A. A. Alsairafi, {CFD} and experimental studies of fouling of a microfiltration membrane, Chemical Engineering and Processing: Process Intensification 48 (2009) 1405 – 1413.

[8] R. Ghidossi, J. Daurelle, D. Veyret, P. Moulin, Simplified {CFD} approach of a hollow fiber ultrafiltration system, Chemical Engineering Journal 123 (2006) 117 – 125.

[9] S. Ghose, C. Bhattacharjee, S. Datta, Simulation of unstirred batch ultrafiltration process based on a reversible pore-plugging model, Journal of Membrane Science 169 (2000) 29 – 38.

[10] G. Jonsson, Boundary layer phenomena during ultrafiltration of dextran and whey protein solutions, Desalination 51 (1984) 61 – 77.

[11] G. Jonsson, C. Boesen, Water and solute transport through cellulose acetate reverse osmosis membranes, Desalination 17 (1975) 145 – 165.

[12] G. Jonsson, Overview of theories for water and solute transport in9 uf/ro membranes, Desalination 35 (1980) 21 – 38.

[13] J. G. Wijmans, R. W. Baker, The solution-diffusion model: a review, Journal of Membrane Science 107 (1995) 1 – 21.

[14] F. Vinther, M. Pinelo, M. Brøns, G. Jonsson, A. S. Meyer, Statistical modelling of the interplay between solute shape and rejection in porous membranes, Separation and Purification Technology 89 (2012) 261 – 269.

[15] C. Bhattacharjee, P. Sarkar, S. Datta, B. Gupta, P. Bhattacharya, Parameter estimation and performance study during ultrafiltration of kraft black liquor, Separation and Purification Technology 51 (2006) 247 – 257.
[16] H. Susanto, S. Franzka, M. Ulbricht, Dextran fouling of polyethersulfone ultrafiltration membranes-causes, extent and consequences, Journal of Membrane Science 296 (2007) 147 – 155.
[17] T. Kobayashi, X. Chai, N. Fujii, Ultrasound enhanced cross-flow membrane filtration, Separation and Purification Technology 17 (1999) 31 – 40.
[18] G. Jonsson, The osmotic pressure model, in: Characterization of Ultrafiltration Membranes: Proceedings from an International Workshop , Arranged by Department of Food Engineering Lund University, Sweden in Cooperation with The Swedish Foundation for Membrane Technology; Örenäs Slott, Sweden, September 9-11, 1987, Lund Univ., 1988, pp. 125–140.
[19] L. Landau, E. Lifshitz, Course of Theoretical Physics Volume 6, Fluid Mechanics 2nd Edition, ©Reed Educational and Professional Publishing Ltd., 1998.
[20] L. Lebrun, G.-A. Junter, Diffusion of dextran through microporous membrane filters, Journal of Membrane Science 88 (1994) 253 – 261.
[21] E. M. Fahner, G. H. Grossmann, K. H. Ebert, Elastic and quasielastic light scattering studies on the branching characteristics of dextrans, Die Makromolekulare Chemie 185 (1984) 2205–2212.
[22] K. A. Granath, B. E. Kvist, Molecular weight distribution analysis by gel chromatography on sephadex, Journal of Chromatography A 28 (1967) 69 – 81.
[23] J. Armstrong, R. Wenby, H. Meiselman, T. Fisher, The hydrodynamic radii of macromolecules and their effect on red blood cell aggregation, Biophysical Journal 87 (2004) 4259 – 4270.
[24] Pharmacosmos, Physical properties of dextran, `http://dextran.net/dextran-physical-properties.html`, 2013. [Online; accessed 19-March-2013].
[25] R. B. Bird, R. C. Armstrong, O. Hassager, Dynamics of Polymeric Liquids, John Wiley & Sons, 1977.
[26] E. Antoniou, M. Tsianou, Solution properties of dextran in water and in formamide, Journal of Applied Polymer Science 125 (2012) 1681–1692.
[27] B. N. Preston, W. D. Comper, A. E. Hughes, I. Snook, W. van Megen, Diffusion of dextran at intermediate concentrations, J. Chem. Soc., Faraday Trans. 1 78 (1982) 1209–1221.
[28] C. E. Ioan, T. Aberle, W. Burchard, Structure properties of dextran. 2. dilute solution, Macromolecules 33 (2000) 5730–5739.
[29] E. Rotureau, E. Dellacherie, A. Durand, Viscosity of aqueous solutions of polysaccharides and hydrophobically modified polysaccharides: Application of fedors equation, European Polymer Journal 42 (2006) 1086 – 1092.
[30] H. Schlichting, K. Gersten, Boundary Layer Theory, 8th Revised and Enlarged Edition, Springer, 2003.
[31] N. Tilton, D. Martinand, E. Serre, R. M. Lueptow, Incorporating darcy's law for pure solvent flow through porous tubes: Asymptotic solution and numerical simulations, AIChE Journal 58 (2012) 2030–2044.
[32] J. M. Miranda, J. B. Campos, Mass transfer in the vicinity of a separation membrane-the applicability of the stagnant film theory, Journal of Membrane Science 202 (2002) 137 – 150.
[33] P. Prádanos, J. Arribas, A. Hernández, Mass transfer coefficient and retention of {PEGs} in low pressure cross-flow ultrafiltration through asymmetric membranes, Journal of Membrane Science 99 (1995) 1 – 20.
[34] G. Jonsson, Transport phenomena in ultrafiltration: Membrane selectivity and boundary layer phenomena, Pure and Applied Chemistry 58 (1986) 1647 – 1656.
[35] N. Hilal, M. Al-Abri, H. Al-Hinai, M. Abu-Arabi, Characterization and retention of {NF} membranes using peg, {HS} and polyelectrolytes, Desalination 221 (2008) 284 – 293.
[36] E. Tsapuik, M. Bryk, An interpretation of the separation of low and high molecular weight solutes by ultrafiltration, Journal of Membrane Science 79 (1993) 227 – 240.
[37] C. Causserand, S. Rouaix, A. Akbari, P. Aimar, Improvement of a method for the characterization of ultrafiltration membranes by measurements of tracers retention, Journal of Membrane Science 238 (2004) 177 – 190.
[38] W. N. Gill, D. E. Wiley, C. J. D. Fell, A. G. Fane, Effect of viscosity on concentration polarization in ultrafiltration, AIChE Journal 34 (1988) 1563–1567.
[39] S. Nicolas, I. Boulanouar, B. Bariou, Unstirred dead-end ultrafiltration: a method to determine diffusion coefficient or osmotic pressure for non-charged macromolecular solutions, Journal of Membrane Science 103 (1995) 19 – 30.
[40] S. Ma, S. C. Kassinos, D. F. Kassinos, Assessing the impact of concentration-dependent fluid properties on concentration polarization in crossflow membrane systems, Industrial & Engineering Chemistry Research 47 (2008) 1636–1649.
[41] Q. She, X. Jin, Q. Li, C. Y. Tang, Relating reverse and forward solute diffusion to membrane fouling in osmotically driven membrane processes, Water Research 46 (2012) 2478 – 2486.
[42] J. S. Yong, W. A. Phillip, M. Elimelech, Coupled reverse draw solute permeation and water flux in forward osmosis with neutral draw solutes, Journal of Membrane Science 392 - 393 (2012) 9 – 17.
[43] H. Vink, Precision measurements of osmotic pressure in concentrated polymer solutions, European Polymer Journal 7 (1971) 1411 – 1419.

Chapter 5

# Back-shocking

## 5.1 Introduction

As explained previously concentration polarization diminishes the performance of a given membrane separation process. In a time-dependent study, the build up of the concentration polarization decreases both the volumetric flux through the membrane and the observed rejection. These effects arise from two phenomena. Firstly, the build up of concentration polarization causes an increase in osmotic pressure, which in return decreases the volumetric flux through the membrane. Secondly, the increased concentration on the membrane surface will result in a larger transport of solute through the membrane. A schematic illustration of this is shown in figure 5.1.

In membrane processes without back-shocking the pressure difference across the membrane, $p_{tmp}$ is such that the solute flux and solvent flux is directed from the retentate to the permeate. Back-shocking is a process where the flux through the membrane is reversed for a period of time, known as the back-shock period, $t_{bs}$. The flux is reversed due to an increase in the pressure on the permeate side of the membrane. The pressure difference across the membrane during the back-shock period, $p_{bs}$, causes the driving force to be directed from the permeate to the retentate. This negative flux immediately decreases the concentration on the membrane surface which causes a decrease in the solute flux

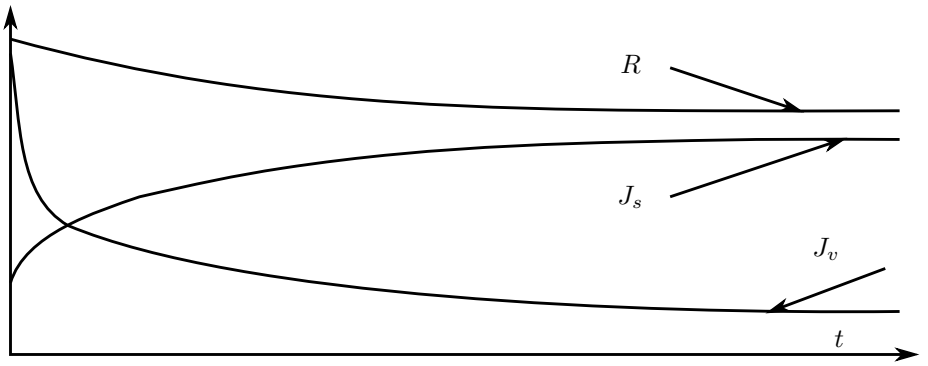


Figure 5.1: Illustration of the different fluxes as a function of time.

through the membrane. After a period of back-shocking the pressure difference is again reversed for a period of time, known as the time between back-shocking, $t_{bbs}$, causing the flux of both solute and solvent to be from the retentate to the permeate. The benefit of this process is that in the time of back-shocking the concentration polarization is convected into the bulk. Therefore, when the pressure is reversed the concentration polarization builds up towards the steady-state solution. Hence, in this period of time the membrane performs better as compared to the steady-state solution. A schematic illustration of this is shown in figure 5.2.

In the literature many examples can be found which demonstrates the benefit of operating with back-shocking [38, 52, 56, 57, 33, 54, 31, 59, 20]. Of these [38, 52, 33, 54, 31, 59, 20, 30, 7] are on ultrafiltration.

In [38] an increase in flux of 3.9 times compared to the steady-state was reported when using a dextrin solution in a spiral wrap membrane.

In [52] back-shocking was used with an impermeable membrane and an albumin solution. The results showed a maximum increase in the solvent flux of 3.8 times the flux without back-shocking.

In [54] wastewater is treated using ultrafiltration, here the increase in the solvent flux when using back-shocking was as high as 17 %.

In general a larger effect is observed in microfiltration. [56, 57] reports a flux of five times the steady-state solution when back-shocking is applied. This is assumed to be due to the formation of a cake layer on the membrane surface. This cake layer greatly reduces the flux through the membrane. In [32] a flux

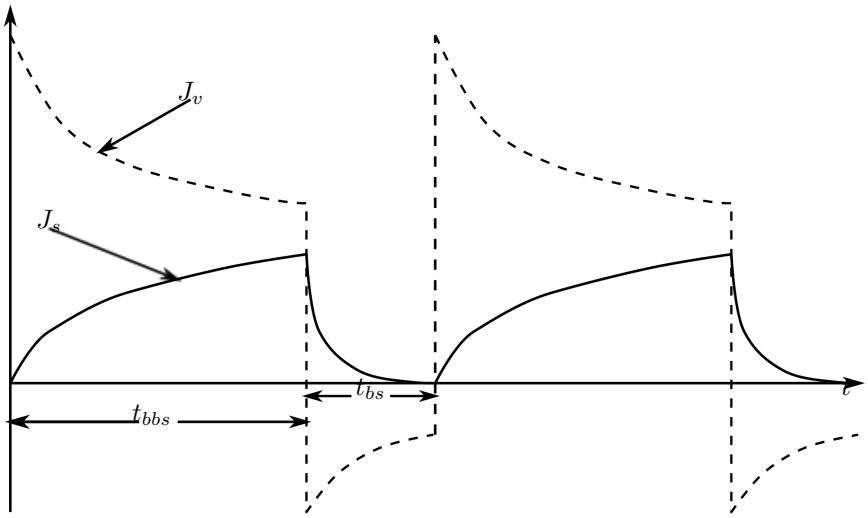


Figure 5.2: Illustration of the different fluxes as a function of time during back-shocking.

increase of up to ten times the flux without back-shocking is reported.

Several mathematical models describing back-shocking have been made [44, 49, 51, 50, 40]. Of these [49] models the dynamics of an osmotic backwash cycle. Whereas [51, 50, 40] all model microfiltration where a cake-layer is assumed. This assumption is well supported. Firstly, by the good agreement between the models and experiments. Secondly, by visual observations [41, 42, 43].

The general approach of the models presented in [51, 50, 40] is that the flux during forward filtration through the membrane is given by dead end filtration. In [51] the forward filtration happens immediately after the back-shock. In [50] the continuity equation for the solute in the bulk during and after back-shocking is solved. During forward filtration the continuity equation is solved until the concentration on the membrane reaches the maximum packing density. Until this value is reached the flux through the membrane is given by the pure water flux to account for the delay in cake formation. After the maximum packing density is reached the solvent flux decreases according to dead end filtration. In [40] an additional function is added that is a measure of the amount of the cake layer which is removed as a function time.

This chapter concerns mathematical modelling of back-shocking in the hollow fibre module presented in chapter 4. We will not model internal fouling of the

membrane. As a consequence the long time performance of the membrane will be determined by the steady-state solution presented in chapter 4. In this chapter two models will be presented that investigate the effect of back-shocking. As in the stationary model presented in section 4 the characteristics of the solute, $D, \eta(c)$, will influence the results of the model. This chapter, however, only concerns the modelling of a solute having the same properties as Dextran $T_{500}$. Moreover, it is obvious that the operating parameters - the inlet velocity, the transmembrane pressure, the back-shock pressure, the back-shock time, and the time between back-shocking - will influence the efficiency of back-shocking. The aim of the models presented in this chapter is therefore to find the parameter set that optimizes the volumetric flux, or the observed rejection, or both, when back-shocking is applied as compared to the steady-state solution.

We will assume that the characteristics of the membrane do not change with working parameters. Hence, we have a multi-parameter problem of finding the parameter set such that we maximize the observed rejection, the volumetric flux, or both. I.e., we want to find the parameter set such that we have

$$R_{obs,max} = \max R_{obs}(t; t_{bs}, t_{bbs}, p_{tmp}, p_{bs}, u_{in,av}), \tag{5.1}$$

$$J_{v,max} = \max J_v(t; t_{bs}, t_{bbs}, p_{tmp}, p_{bs}, u_{in,av}). \tag{5.2}$$

It will, however, be necessary to confine the parameters to certain intervals. These intervals are chosen for two reasons. Firstly, the model should reflect physically possible scenarios. E.g. infinite transmembrane pressure, back-shock pressure, or inlet velocity are unrealistic. Secondly, a finite set of parameters results in a finite amount of simulations. Therefore, the parameters will be varied in the following intervals

$$\begin{gathered} t_{bs} \in [0.1; 2]\mathrm{s}\,, \quad t_{bbs} \in [5; 10]\mathrm{s}\,, \\ p_{bs} \in [0.5; 3]\mathrm{bar}\,, \quad p_{tmp} \in [0.5; 2]\mathrm{bar}\,, \quad u_{in,av} \in [0.86; 1.29]\mathrm{m/s}\,. \end{gathered} \tag{5.3}$$

The inlet average inlet velocities corresponds to Reynolds numbers in the hollow fibre, of which this model is a simplification. Therefore, in order to relate this model with both the previous and the following model it should be noted that $u_{in,av} = 0.86\mathrm{m/s}$ correspond to $\mathrm{Re} = 600$ and $u_{in,av} = 1.29\mathrm{m/s}$ corresponds to $\mathrm{Re} = 900$.

Since there is a huge computational effort involved when solving the time dependent Navier-Stokes equation along with the continuity equation for the solute, it has been necessary to introduce two models.

The simplest model is a two dimensional model, presented in section 5.2, Here the continuity equation will be solved in a two dimensional domain. The domain will be the length of the membrane times several widths of the boundary layer

thickness. The velocity component perpendicular to the membrane is given by the flux through the membrane and the velocity component in tangential to the membrane will be assumed linear and given by a first order Taylor expansion of a fully developed Poiseuille flow. This model will be referred to as the 2D-model.

In the three dimensional, axial symmetric, model presented in section 5.7, the full Navier-Stokes equation, as well as the continuity equation for both solvent and solute, is solved within the hollow fibre. As compared to the 2D-model this model allows a concentration dependent viscosity. The computational effort in solving this model, however, restricts the simulations to a hollow fibre with a membrane length of 14 cm. Moreover, we will confine the simulations of the full three dimensional model around the parameter set, determined from the knowledge gained from the 2D-model. This model will be referred to as the 3D-model.

In both models we restrict the simulations to membranes where the intrinsic rejection is high, such that the solution diffusion model is a good approximation for the flux of solute and solvent through the membrane. Furthermore, the same values of the solvent permeability and the solute permeability used in chapter 4 will be used. I.e., $A = 192^{\mathrm{L}}/_{\mathrm{m^2hbar}}$ and $B = 0.47^{\mathrm{L}}/_{\mathrm{hm^2}}$. This allows us to investigate the influence of back-shocking on both the solvent flux and the observed rejection. Moreover, the flux through the membrane during back-shocking will be pure solvent.

## 5.2 2D model

In this model we will solve the continuity equation for the solute in two dimensions close to the membrane surface.

We will assume that for a given average inlet velocity into the hollow fibre, $u_{av}$, the velocity in the axial direction is well approximated by a Poiseuille flow. Furthermore, it will be assumed that this velocity does not depend on time. Thus,

$$v_x(r) \approx 2U_{av}\left(1 - \left(\frac{r}{R}\right)^2\right). \tag{5.4}$$

Moreover, we will assume that we are so close to the membrane surface that the axial velocity is well approximated by a first order Taylor expansion. Defining a new variable $y = R - r$ we have, by inserting the expression for $y$ into equation

(5.4), that

$$v_x(y) = 2u_{av}\left(1 - \left(1 - \frac{y}{R}\right)^2\right). \tag{5.5}$$

A first order Taylor expansion for small values of $y$ gives

$$v_x(y) \approx v_z(0) + \left.\frac{dv_z}{dy}\right|_{y=0} y = \frac{4u_{in,av}}{R} y\,. \tag{5.6}$$

The velocity normal to the membrane will be considered independent of $y$ and equal to the flux through the membrane. Hence,

$$v_y(x,t) = -A(p(x) - (p_{tmp} + p_{bs})\,\Phi_n(t) - \pi(c(x,0,t)))\,, \tag{5.7}$$

where $p(x)$ is the pressure that varies in the axial direction, $p_{tmp}$ is the transmembrane pressure and $p_{bs}$ is the back-shock pressure, $\Phi(t)$ is a smoothed hat function defined as being one when there is a back-shock applied and zero when no back-shock is applied.

More specific all simulations will be made such that there is an initial time $T_i$ followed by the first back-shock $t_{bs,1}$ followed by a the first time between back-shock $t_{bbs,1}$. Hereafter comes the second period and so forth. Thus, denoting

$$T_n = T_i + (n-1)(t_{bs} + t_{bbs}), \tag{5.8}$$

$\Phi_n(t)$ is defined as

$$\Phi_n(t) = \begin{cases} 0 & \text{for} \quad t < T_n - \epsilon/2 \\ 1 & \text{for} \quad T_n + \epsilon/2 < t < T_n + T_{bs} - \epsilon/2 \\ 0 & \text{for} \quad t < T_n + t_{bs} + \epsilon/2 \end{cases} \tag{5.9}$$

where $\epsilon$ is a time small compared to $t_{bs}$ where the $\Phi_n(t)$ continuously changes from zero to one or one to zero. The osmotic pressure $\pi(c(x,0,t))$ depends on the concentration on the membrane surface, which depends on both the time and the axial position. The osmotic pressure will be given by equation (2.9).

Notice that the fluid is incompressible since $\nabla \cdot \boldsymbol{v} = 0$.

The pressure on the membrane surface will be assumed linear and given by the Poiseuille pressure profile. Hence,

$$p_{in} - p_{out} = \frac{8\eta_s L_m u_{in,av}}{R^2}\,. \tag{5.10}$$

Furthermore, the average transmembrane pressure is given by

$$p_{tmp} = \frac{p_{in} + p_{out}}{2} \tag{5.11}$$

The assumption that the pressure is linear gives

$$p(x) = p_{in} - \frac{p_{in} - p_{out}}{L_m} x \,. \tag{5.12}$$

Combining equation (5.10), equation (5.11), and equation (5.12) we get the following expression for the pressure as a function of $x$

$$p(x) = p_{tmp} + \frac{8\eta_s L_m u_{in,av}}{R^2} \left( \frac{1}{2} - \frac{x}{L_m} \right) . \tag{5.13}$$

The continuity equation for the solute is given by

$$\frac{\partial c}{\partial t} + v_x(y) \frac{\partial c}{\partial x} + v_y(x,t) \frac{\partial c}{\partial y} = D \left( \frac{\partial^2 c}{\partial x^2} + \frac{\partial^2 c}{\partial x^2} \right) , \tag{5.14}$$

where $D$ is the diffusion coefficient given by equation (2.7) with a molecular weight of 500 kDa. The continuity equation is solved with the boundary conditions

$$c(0,y) = c_{in} \,, \tag{5.15a}$$

$$c(x, y_{max}) = c_{in} \wedge \frac{\partial c}{\partial y} \,|_{y_{max}} = 0 \,, \tag{5.15b}$$

$$v_y(x,0,t)c(x,0,t) - D \frac{\partial c(x,0,t)}{\partial y} = Bc(x,0,t) \,, \tag{5.15c}$$

$$\frac{\partial c(L_m, y, t)}{\partial x} = 0 \,. \tag{5.15d}$$

### 5.2.1 Scaling the equations

The equations of motion and the boundary conditions will be scaled using the scaled variables

$$\hat{c} = \frac{c}{c_{in}} \,, \quad \hat{x} = \frac{x}{L_m} \,, \quad \hat{y} = \frac{y}{\delta} \,, \quad \hat{v}_x = \frac{v_x}{\bar{J}_{v,av}} \,, \quad \hat{v}_y = \frac{v_y}{\bar{J}_{v,av}} \,, \quad \hat{t} = \frac{t}{\delta / J_{v,av}} \,. \tag{5.16}$$

As seen in appendix A.3 this gives the following expression for the continuity equation

$$\frac{\partial \hat{c}}{\partial \hat{t}} + \lambda \hat{v}_x \frac{\partial \hat{c}}{\partial \hat{x}} + \hat{v}_y \frac{\partial \hat{c}}{\partial \hat{y}} = \frac{1}{\mathrm{Pe}_{bl}} \left( \lambda^2 \frac{\partial^2 \hat{c}}{\partial \hat{x}^2} + \frac{\partial^2 \hat{c}}{\partial \hat{y}^2} \right) , \tag{5.17}$$

where $\mathrm{Pe}_{bl} = {}^{\bar{J}_{v,av}\delta}/_{D}$ and $\lambda = {}^{\delta}/_{L_m}$. The boundary conditions become

$$c(0,\hat{y}) = 1\,, \tag{5.18a}$$

$$c(\hat{x},\hat{y}_{max}) = 1 \wedge \frac{\partial \hat{c}}{\partial \hat{y}}\,|_{\hat{y}_{max}} = 0\,, \tag{5.18b}$$

$$\hat{v}_y(\hat{x},0,\hat{t})\hat{c}(\hat{x},0,\hat{t}) - \frac{1}{\mathrm{Pe}_{bl}}\frac{\partial \hat{c}(\hat{x},0,\hat{t})}{\partial \hat{y}} = \hat{B}\hat{c}(\hat{x},0,\hat{t})\,, \tag{5.18c}$$

$$\frac{\partial \hat{c}(1,\hat{y},\hat{t})}{\partial \hat{x}} = 0\,, \tag{5.18d}$$

where $\hat{B} = {}^{B}/_{\bar{J}_{v,av}}$.

The values of the various scaling constants are

$$\delta = 18\mu\mathrm{m}\,, \quad L_m = 46\mathrm{cm}\,, \quad \bar{J}_{v,av} = 6{}^{\mu\mathrm{m}}/_{\mathrm{s}}\,, \quad \frac{\delta}{\bar{J}_{v,av}} = 3s\,. \tag{5.19}$$

The equations above will be solved in the domain given by $[0,1]\times[0,\hat{y}_{max}]$ where $\hat{y}_{max} = \{5,10\}$ depending on the parameter values. This is done to ensure that the boundary condition at $y_{max}$ is a good approximation.

For both values of $\hat{y}_{max}$ a mapped mesh is used to ensure a high resolution close to the boundary layer. The mesh has 100 elements in the $\hat{x}$-direction. When $\hat{y}_{max} = 5$ there are 100 elements in $\hat{y}$-direction. The element size is decreasing towards the membrane surface using a geometric sequence with an element ratio of 0.05. This leads to 10201 degrees of freedom.

Dependence of the solution on the mesh has been tested. In all simulations made the mesh has the same number of elements in both directions and the element ratio given above. Denoting the solution to the simulations with $n \times n$ elements by $S_n$, computations were made with $n = \{25, 50, 100, 200, 400\}$. These simulations were simulated over the same period of time and having five back-shock periods. The solver gave an output for the same time-step $\Delta t$. It should, however, be noted that the solver solves the equations for internal time-steps much smaller than this time. It is, however, only desirable to have the solution for certain time-steps due to size of each data-set. Thus, the discrete time is given by $t_1 = 0, t_2 = \Delta t, ..., t_i = (i-1)\Delta t$.

The main interest of the simulations is the concentration on the membrane surface, as this influences the flux of both solute and solvent. As the amount of data points on the membrane surface is increasing with the number of $n$ a direct comparison was not possible. Instead a comparison between the integral over the membrane surface has been made. Since the time step is the same for

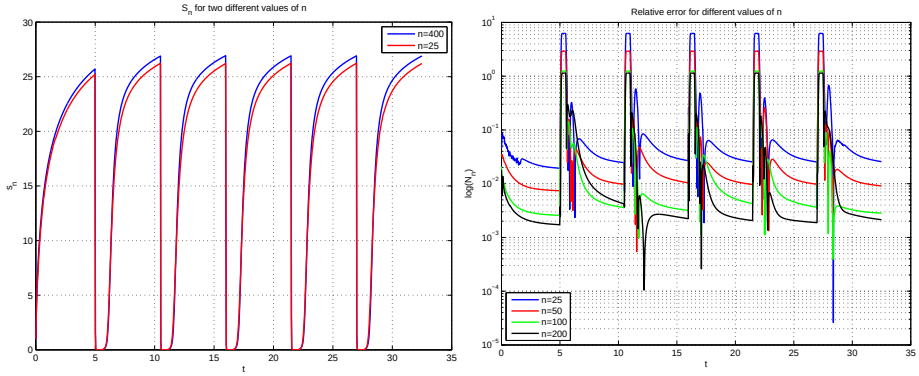


(a) Comparison between the solution on two different mesh, $n = 25$ and $n = 400$.

(b) The relative error for different number of mesh elements.

Figure 5.3: Investigation of relative error for different number of mesh elements: a) Comparison between the solution with the coarsest mesh and the finest mesh, b) Relative error for different number of mesh elements.

all values of $n$, the solution to every time-step can be compared. Hence, the following vectors are defined

$$\boldsymbol{s}_n : s_{n,i} = \int_0^1 S_n(x, 0, t_i)dx\,. \tag{5.20}$$

Here $i$ refers to the i'th element of the vector $\boldsymbol{s}_n$. Comparing the solutions with the densest mesh, $n = 400$, we define the following norm

$$\boldsymbol{N}_n : N_{n,i} = \frac{|s_{n,i} - s_{400,i}|}{|s_{400,i}|}\,. \tag{5.21}$$

One could fear that division with zero would be a problem. It turns out, however, that this is not the case. The smallest values in $\boldsymbol{s}_{400}$ is $7.2 \cdot 10^{-4}$. Hence, the relative norm is well defined. In figure 5.3a $\boldsymbol{s}_{400}$ and $\boldsymbol{s}_{25}$ is plotted as a function of time. As seen the solution for the two meshes follow the same tendency. There is, however, a rather large difference. Furthermore, it is seen that during back-shocking the concentration on the membrane surface tends to zero. Hence, the introduction of $\epsilon$ in equation (5.21). In figure 5.3b the relative error is shown for each time and for the different values of $n$.

As expected the relative error decreases for an increasing number of mesh elements. There is, however, rather large errors for all values of $n$. When comparing to figure 5.3a these are confined to when the concentration on the membrane surface is very small. Hence, these relative errors will not contribute

COMSOL 4.3.2.189

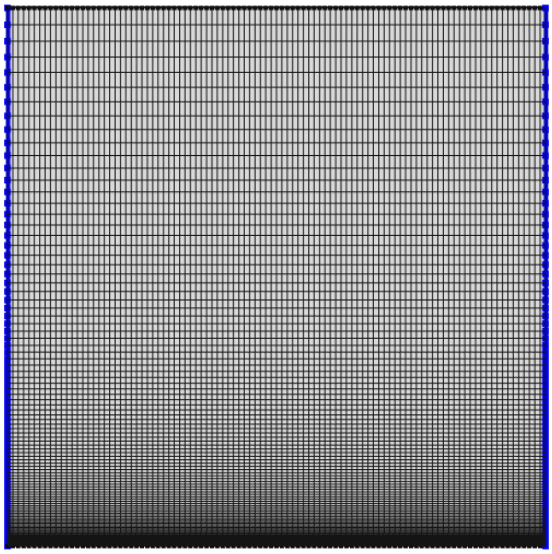

Figure 5.4: The mesh used when $\hat{y}_{max} = 5$.

significantly to the results presented. Besides the error when the concentration is close to zero, the error for $n = 100$ is within one percent of the solution with $n = 400$. Thus, in order to reduce simulation time $n = 100$ has been chosen.

When $\hat{y}_{max} = 10$ there are 250 elements in $\hat{y}$-direction. The element size decreases towards the membrane surface using a geometric sequence with an element ratio of 0.05. This leads to 25321 degrees of freedom. The mesh used for $\hat{y}_{max} = 5$ is shown in figure 5.4.

### 5.2.2 Simulations and measured quantities

For each parameter set $\theta = (p_{tmp}, u_{in,av})$ a steady-state simulation is made giving the steady-state flux of both solvent and solute, $J_{v,ss}(\theta)$ and $J_{s,ss}(\theta)$.

For all simulations the initial condition on the concentration will be $\hat{c} = 1$. We will simulate for a time given by $T_s = t_i + 5(t_{bs} + t_{bbs})$. If nothing else is mentioned the initial time $t_i$ will be equal to the time between back-shock $t_{bbs}$. The initial time is necessary to approach the steady state solution. Hereafter, the periodic back-shock is applied and the solution will converge towards a periodic

solution.

Since this is a two dimensional model there will be an average flux for each time instant. This is defined as

$$J_{v,av}(\hat{t}) = \int_0^1 \hat{J}_v(\hat{x},\hat{t})d\hat{x}\,, \tag{5.22}$$

and similarly for the solute flux

$$J_{s,av}(\hat{t}) = \int_0^1 \hat{J}_s(\hat{x},\hat{t})d\hat{x}\,. \tag{5.23}$$

Moreover, we define the steady-state average solvent flux as

$$J_{v,ss} = \int_0^1 \hat{J}_{v,ss}(\hat{x})d\hat{x}\,, \tag{5.24}$$

and similarly for the steady-state solute flux

$$J_{s,ss} = \int_0^1 \hat{J}_{s,ss}(\hat{x})d\hat{x}\,. \tag{5.25}$$

In all simulations the periodic solution is obtained after two back-shock cycles. Therefore, the average flux is calculated only from the data of the last three back-shock cycles. I.e.,

$$\langle J_v\rangle = \frac{\int_{\hat{t}_i+2(\hat{t}_{bs}+\hat{t}_{bbs})}^{\hat{t}_i+5(\hat{t}_{bs}+\hat{t}_{bbs})}\int_0^1 \hat{J}_v(\hat{x},\hat{t})d\hat{x}d\hat{t}}{3(\hat{t}_{bs}+\hat{t}_{bbs})} \tag{5.26}$$

and

$$\langle J_s\rangle = \frac{\int_{\hat{t}_i+2(\hat{t}_{bs}+\hat{t}_{bbs})}^{\hat{t}_i+5(\hat{t}_{bs}+\hat{t}_{bbs})}\int_0^1 \hat{J}_s(\hat{x},\hat{t})d\hat{x}d\hat{t}}{3(\hat{t}_{bs}+\hat{t}_{bbs})} \tag{5.27}$$

The observed rejection will be given by

$$R_{obs} = \left(1 - \frac{\langle J_s\rangle}{\langle J_v\rangle}\right)\,. \tag{5.28}$$

### 5.2.3 Results

The results of the simulations are presented in this section.

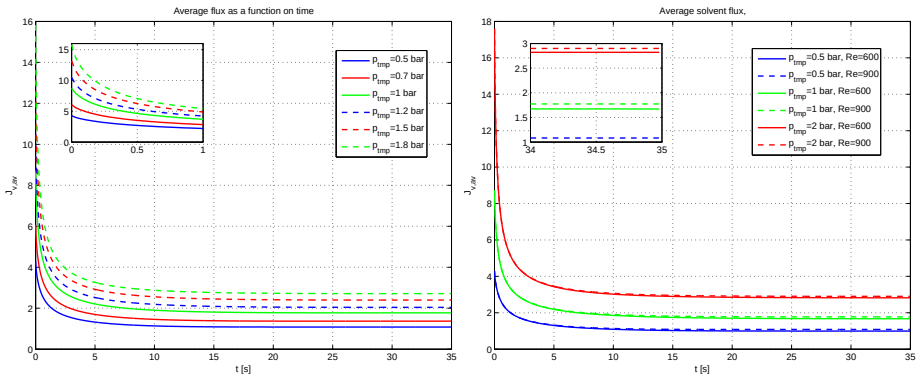


(a) Average solvent flux as a function of time for different transmembrane pressures when no back-shock pressure is applied. The inset is a zoom of the first second.

(b) Average solvent flux as a function of time for different transmembrane pressures and inlet velocities when no back-shock pressure is applied. The inset is a zoom of the last second.

Figure 5.5: Average solvent flux as a function of time for: a) different transmembrane pressures, b) different inlet velocities.

#### 5.2.3.1 General results

When there is no back-shock applied the average solvent flux through the membrane decreases towards the average solvent flux of the steady-state solution. This is illustrated for different transmembrane pressures in figure 5.5a. As seen both the initial average solvent flux and the steady-state average solvent flux increase for increasing transmembrane pressures.

In figure 5.5b the average solvent flux through the membrane is shown for different transmembrane pressures and different inlet velocities. As seen the steady-state average solvent flux through the membrane is higher for higher inlet velocities at the same transmembrane pressures.

Before investigating the effect of varying different parameters during back-shocking the qualitative features of the simulations will be illustrated.

In all simulations with back-shocking there is an initial time needed to obtain a periodic steady-state. When this is obtained all simulations have the same qualitative behaviour. This will be illustrated using a simulation with $t_{bs} = 0.6$s, $p_{tmp} = p_{bs} = 2$bar, and $\mathrm{Re} = 900$. To ease the illustration we define a variable, $t_{abs}$ - the time after back-shock. In figure 5.6 the concentration polarization, just before the back-shock is applied, is shown. Furthermore, the contour line where

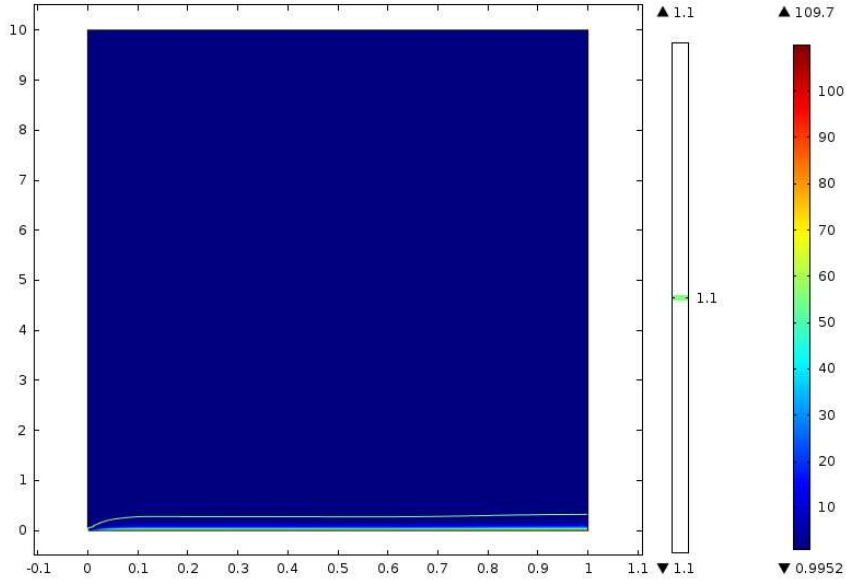


Figure 5.6: Concentration field just before the back-shock is applied, $t_{abs} = 0$.

the concentration is 1.1 illustrates the width of the boundary layer.

When the back-shock is applied the concentration polarization gets convected into the bulk of the hollow fibre. This is seen as an area of high concentration compared to the bulk concentration. This area is now confined within the contour line. The highly concentrated area gets convected into the bulk and tangentially along the membrane during the back-shock period. This is illustrated in figure 5.7.

When the pressure is reversed the highly concentrated area is convected towards the membrane. Furthermore, there is a build up of concentration close to the inlet. After a given time the highly concentrated area is in contact with the membrane again. This is illustrated in figure 5.8.

In figure 5.9 the concentration profile perpendicular to the membrane is shown at the end of the membrane $\hat{x} = 1$ and half way down the membrane, $\hat{x} = 1$. The concentration profile corresponds to the concentration field shown in figure 5.6-5.8. For a better illustration the graph has been cut off at $\hat{c} = 40$. It should, however, be noted that the concentration on the membrane surface at $\hat{c}(t_{abs}) \approx 108$. This also seen in figure 5.6. As before, just before the back-shock is applied $t_{abs}$=0 there is a high concentration polarization. The concentration

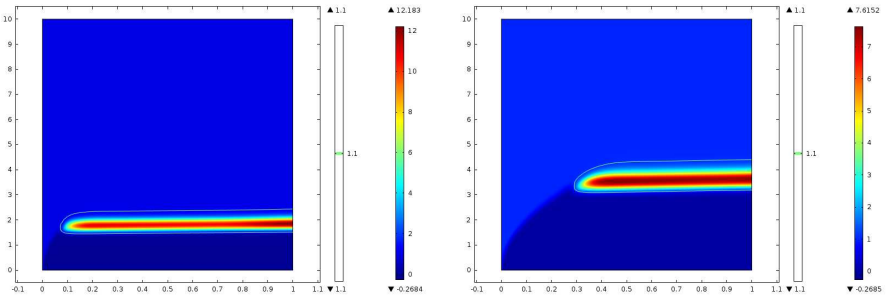

(a) Concentration field during back-shocking, $t_{abs} = 0.3$s.

(b) Concentration field just before the pressure is reversed, $t_{abs} = 0.6$s.

Figure 5.7: Concentration field during back-shocking.

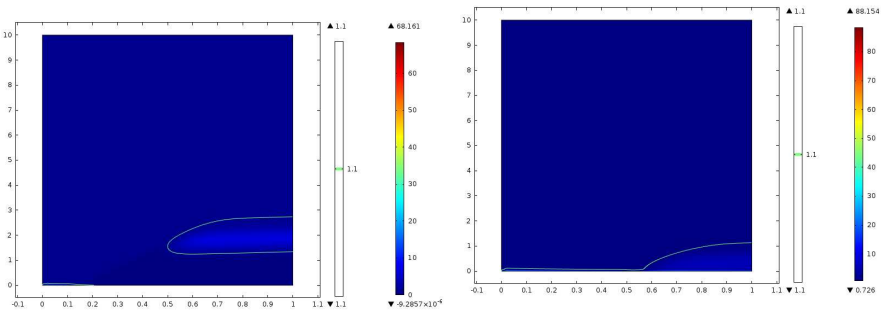

(a) Concentration field during forward filtration, $t_{abs} = 0.9$s.

(b) Concentration field when the highly concentrated area has contact with the membrane, $t_{abs} = 1.2$s.

Figure 5.8: Concentration field during forward filtration.

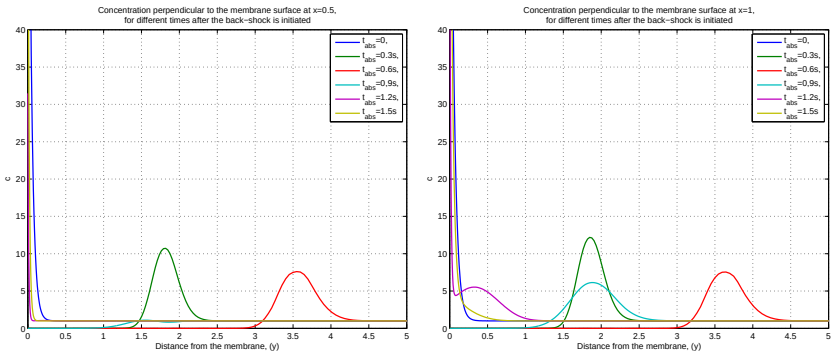


(a) $\hat{x} = 0.5$. (b) $\hat{x} = 1$.

Figure 5.9: Concentration perpendicular to the membrane surface for different times after the back-shock. The parameters used in this simulation is $p_{bs} = p_{tmp} = 2$bar, Re $= 900$.

is then convected away from the membrane. The maximum of the concentration profile decreases and the width of the concentration profile increases as a function of time due to diffusion. Furthermore, it should be noted that the pure solvent flux that is injected during back-shocking causes the concentration to be zero near the membrane surface. Moreover, the passing of the highly concentrated area is seen in figure 5.9a for time $t_{abs} = 0.9$s (see figure 5.8). This is seen as the concentration profile disappearing as compared to figure 5.9b where the profile is still well defined. When the non-zero concentration reaches the membrane the concentration starts to build up on the membrane surface. For times larger than the times shown here the concentration continues to builds up on the membrane surface until the concentration profile shown for $t_{abs} = 0$ is reached.

In figure 5.10a the typical behaviour of the average solvent flux along with the solution without back-shocking is shown. As seen the two solutions are identical in the initial period, $t_i$. When the back-shock is applied the flux becomes negative. Moreover, at the instant the back-shock is applied there is a concentration on the membrane surface which increases the negative flux due to the osmotic pressure. The concentration, however, is removed and the negative flux attains a constant value. When the pressure is reversed the flux attains the value of a clean membrane. As time increases the concentration builds up on the membrane surface causing the flux to decrease towards the steady-state solution. Furthermore, it is seen that the solution enters a periodic solution. This can be seen from the fact that there is no difference between the last three periods.

In figure 5.10b the typical behaviour of the average solute flux along with the solution without back-shock is shown. Again the two solutions are identical

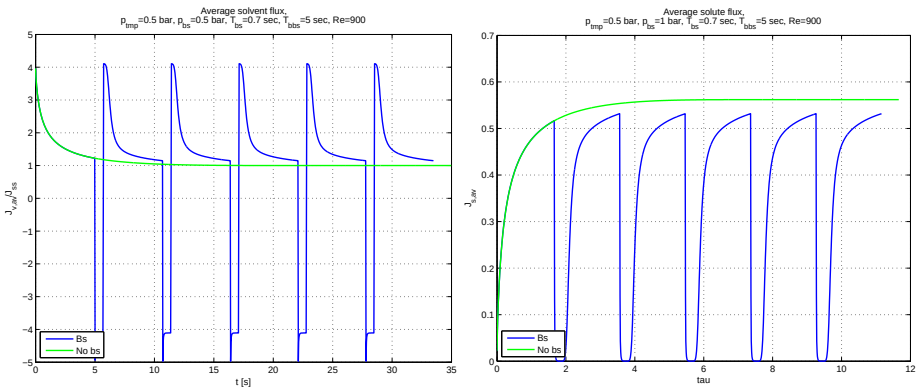


(a) The average solvent flux as a function of time.

(b) The average solute flux as a function of time.

Figure 5.10: Average fluxes: (a) solvent flux, (b) solute flux.

in the initial period. From the moment where the back-shock is applied the concentration on the membrane surface decreases towards zero, causing the solute flux to decrease. When the pressure is reversed, the concentration approaches the steady-state solution. It should be noticed that the solute flux with back-shocking is always lower than the steady-state solution.

Besides the inlet velocity, the parameters that will be varied are the transmembrane pressure, the back-shock pressure, the time between back-shocks, and the back-shock time.

In figure 5.11a the effect of varying the back-shock pressure is illustrated. As seen the negative flux increases with increasing back-shock pressure during the back-shock period. Moreover, the concentration boundary layer will be pushed further away from the membrane when a higher backshock pressure is applied. This results in a higher flux when the pressure is reversed or a longer time where the flux maintains a high value, or both.

In figure 5.11b the effect of varying the transmembrane pressure is shown. As seen the higher the transmembrane pressure the higher the initial flux after back-shock can be obtained as compared to the steady-state flux. The negative flux during back-shock is the same. The steady-state flux, however, is higher for high transmembrane pressures. This can be seen from the ratio between the flux and the steady-state flux having a higher value for high transmembrane pressures. Furthermore, it is seen that the average flux tends faster towards the steady-state solution for high transmembrane pressures.

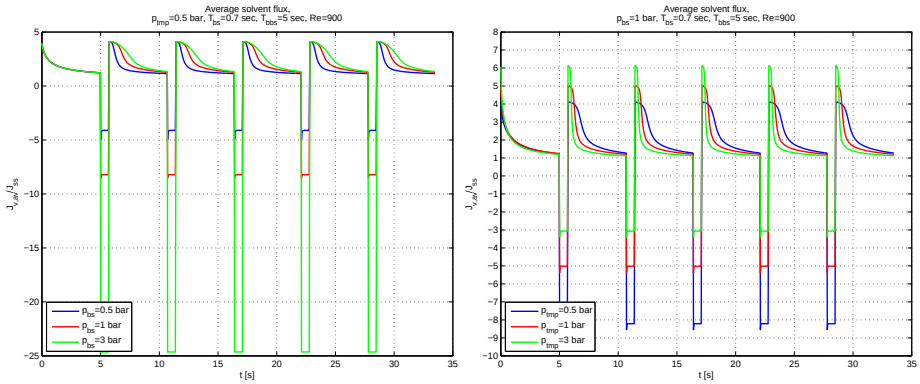


(a) The solvent flux as a function of time for different back-shock pressures.

(b) The solvent flux as a function of time for different transmembrane pressures.

Figure 5.11: Average solvent flux for: (a) different back-shock pressures, (b) different transmembrane pressures.

In figure 5.12a the average solvent flux is shown for different back-shock times. As seen the flux is higher for longer times when the back-shock time is high. This is comparable to the back-shock pressure where the same tendency was seen.

In figure 5.12b the average flux is seen for different times between back-shocking. The longer the time between back-shocking the closer the flux comes to the steady-state solution when the back-shock is applied.

#### 5.2.3.2 Time averaged values

In this section the effect of varying the parameters on the time averaged solvent flux, solute flux as compared to the steady-state solution, e.g, the integral over the last three periods in figure 5.10-5.12, will be investigated. Furthermore, the effect on the observed rejection will be presented. The parameter of interest will be varied whereas the other parameters will be fixed. In all figures the effect of varying the parameter will be shown as a function of the back-shock time.

In figure 5.13 the effect of changing the transmembrane pressure is shown.

The normalized solvent flux is shown in figure 5.13a. As seen, for transmembrane pressures larger than 0.7 bar the time averaged flux attains a value higher than the steady-state flux. Moreover, there is a characteristic maximum for each

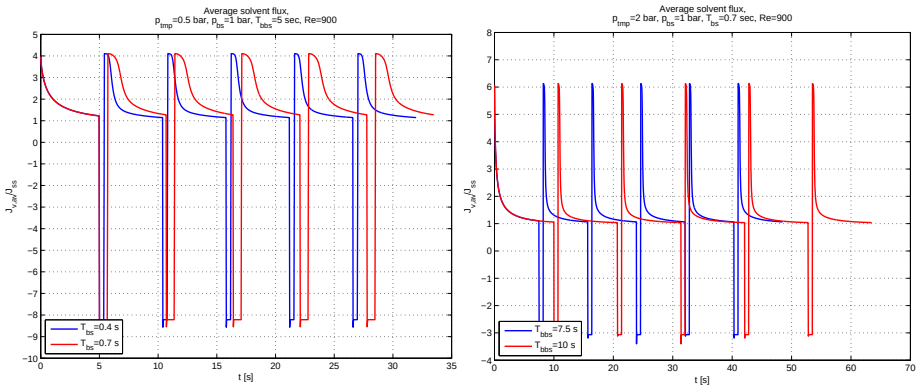


(a) The solvent flux as a function of time for different back-shock times.

(b) The solvent flux as a function of time for different transmembrane pressures.

Figure 5.12: Average solvent flux for: (a) different back-shock times, (b) different times between back-shocking.

transmembrane pressure. This maximum becomes shifted towards higher back-shock times for higher transmembrane pressures. Furthermore, the curves follow each other until they bend of. Here the curves with the smallest transmembrane pressures bend of first. Hence, there is a larger effect for high transmembrane pressures. This can be explained by the higher ratio between the pure solvent flux and steady-state flux. It is noted that the time averaged flux becomes negative for high back-shock times.

In figure 5.13b the time averaged solute flux is shown. As seen the solute flux is decreasing for all transmebrane pressures as a function of the back-shock time. Furthermore, it is noted that the solute flux is higher for higher transmembrane pressures. This is expected since a high transmembrane pressure leads an increase in concentration polarization during forward filtration and a higher solute flux.

In figure 5.13c the observed rejection is shown along with the steady-state observed rejection. It is seen that there is a positive effect of back-shocking for all transmembrane pressures. Here it should be noted that even for a decrease in solvent flux, the observed rejection can increase as seen for a transmembrane pressure of 0.5 bar. The highest values of the observed rejection are obtained for low transmembrane pressures. The increase compared to the steady-state, however, is largest for high transmembrane pressures. Here an increase from approximately 20% to 50 % is observed, whereas an increase from approximately 50% to 70% is observed for a transmembrane pressure of 0.5bar. The maximum of the observed rejection is shifted towards higher back-shock times for higher transmembrane pressures. If compared to figure 5.13a the maximum of the

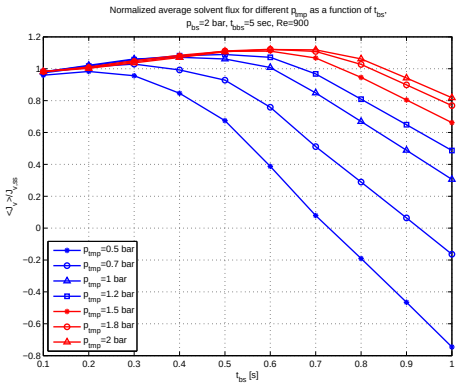


(a) Normalized solvent flux for different transmembrane pressures and different back-shock times.

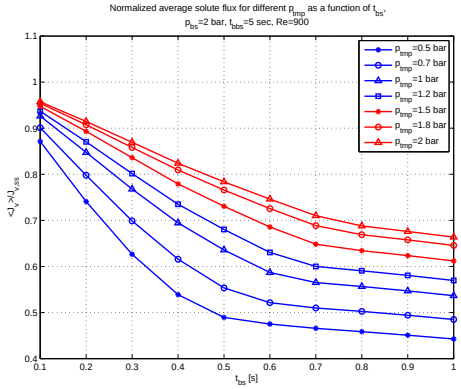


(b) Normalized solute flux for different transmembrane pressures and different back-shock times.

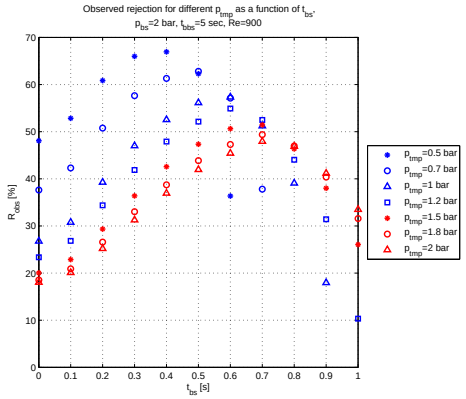


(c) Observed rejection for different transmembrane pressures and different back-shock times.

Figure 5.13: Normalized flux and observed rejection as a function of back-shock times for different transmembrane pressures, using the parameters $p_{bs} = 2$bar, $t_{bbs} = 5$s, and Re $= 900$. The figures represent: (a) The solvent flux, (b) The solute flux, (c) The observed rejection.

observed rejection is observed for higher back-shock times than the maximum of the solvent flux.

In figure 5.14 the effect of varying the back-shock pressure is shown.

As seen in figure 5.14a the maximum of the solvent flux is shifted towards smaller back-shock times for larger transmembrane pressures. Furthermore, the maximum value is increasing for shorter back-shock times.

In figure 5.14b it is seen that the solute flux is higher for smaller values of the back-shock pressure.

From figure 5.14a and 5.14b the behaviour of the observed rejection, shown in figure 5.14c is rather obvious. For small back-shock pressures the solute flux decreases almost linearly, whereas the solvent flux maintains an almost constant value. Hence, the observed rejection increases linearly. For high back-shock pressures the solvent flux attains a maximum value within the interval of back-shock times shown here. This implies that a maximum in the observed rejection is obtained as well. Since all simulations are with the same transmembrane pressure the observed rejection of the steady-state is the same. An increase in observed rejection of approximately 30% is observed for all back-shock pressures except the smallest bac-shock pressure. At this back-shock pressure, however, the observed rejection is still increasing. Thus, it is not possible to say how high an effect can be obtained.

In figure 5.15 the effect of increasing the time between back-shocking is shown.

As seen in figure 5.15a there seems to be no difference in the maximum solvent flux for different times between back-shocking. There is a tendency that for back-shock times smaller than the optimal back-shock time there is a higher effect when the time between back-shocking is short. This tendency is opposite for back-shock times longer than the optimal back-shock time, where the gradient is smaller for longer times between back-shocking. For longer times between back-shocking the concentration field is closer to the concentration field of the steady-state solution. Hence, a higher concentration polarization should be expected, which in the case of small back-shock times influence the forward filtration in a negative way when the pressure is reversed. This can explain the difference in the solvent flux for small back-shock times. That the maximum value does not change significantly suggests that the concentration fields immediately before the back-shock is applied are similar. Hence, at back-shock times of $t_{bbbs} = 5s$ the concentration field is rather close to the steady-state solution. This also implies that the gradient after the maximum is obtained is smaller for high back-shock times due to the relatively longer integration over the steady-state solution.

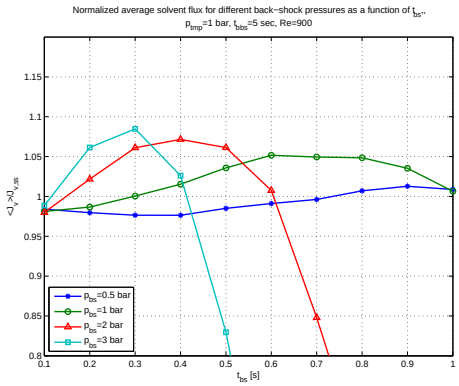


(a) Normalized solvent flux for different back-shock pressures as a function of different back-shock times.

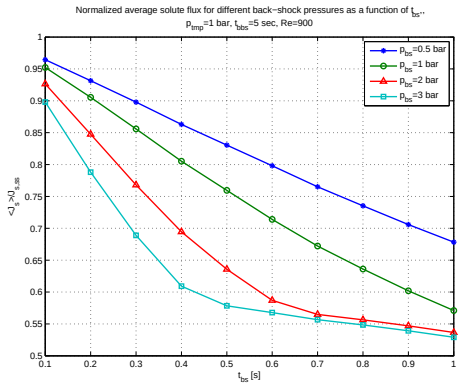


(b) Normalized solute flux for different back-shock pressures as a function of different back-shock times.

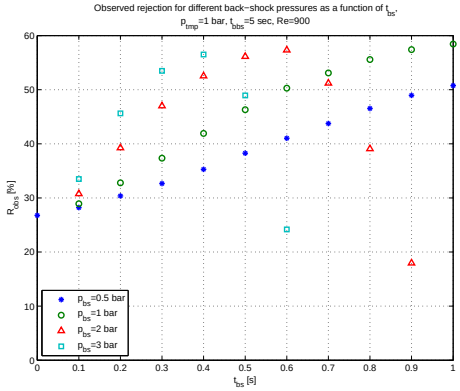


(c) Observed rejection for different back-shock pressures as a function of different back-shock times.

Figure 5.14: Normalized flux and observed rejection as a function of back-shock time for different back-shock pressures, $p_{tmp} = 1\text{bar}$, $\text{Re} = 900$, $t_{bbs} = 5s$. The figues show: (a) The solvent flux, (b) The solute flux, (c) The observed rejection.

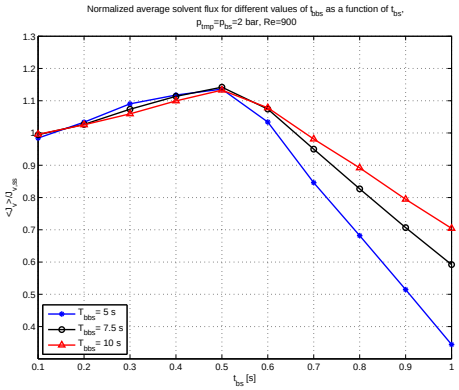


(a) Normalized solvent flux for different times between back-shocking as a function of back-shock time.

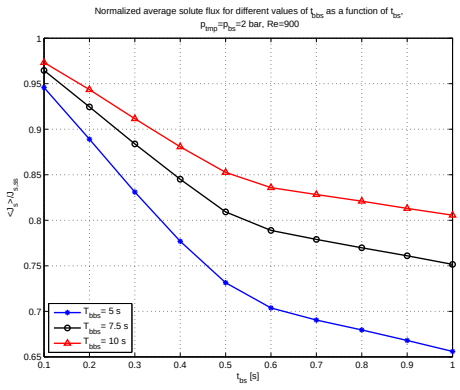


(b) Normalized solute flux for different times between back-shocking as a function of back-shock time.

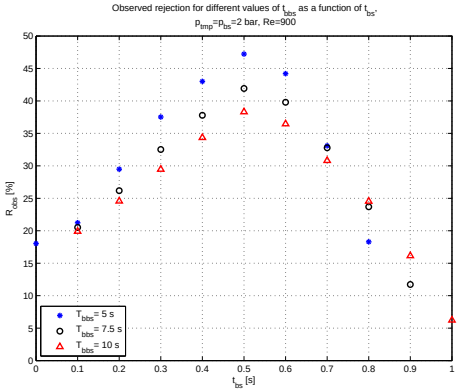


(c) Normalized solute flux for different times between back-shocking as a function of back-shock time.

Figure 5.15: Normalized flux and observed rejection as a function of back-shock times for different back-shock pressures, $p_{tmp} = pbs = 2$bar, Re $= 900$, $t_{bbs} = 5s$: The figures show: (a) The solvent flux, (b) The solute flux, (c) The observed rejection.

The average solute flux shown in figure 5.15b shows an increasing solute flux for long times between back-shocking. This is also expected from the arguments above, as the solute flux attains its highest value at the steady-state.

In figure 5.15c the observed rejection attains its maximum value for the same value of back-shock time, for all three times between back-shocking. The value, however, decreases for increasing time between back-shocking. This is also expected from operating close to the steady-state solution for longer periods of time.

In figure 5.16 the effect of changing the inlet velocity is shown.

As seen in figure 5.16a the normalized time averaged solvent flux attains a higher maximum value for higher inlet velocities. Furthermore, the maximum seems to be shifted towards smaller back-shock times for a high inlet velocity. Moreover, for high back-shock times the gradient of the two curves are similar.

In figure 5.16b the normalized solute flux is shown. Here the two curves more or less follow each other. The curve for highest inlet velocity, however, has the highest value for large times between back-shocking.

In figure 5.16c the observed rejection is shown for the two different inlet velocities. As seen a substantial increase is obtained. The increase is similar in size, with a larger observed rejection for the highest inlet velocity. The observed rejection in steady-state, however, is also larger for the highest inlet velocity. Furthermore, the maximum value is attained for lower back-shock times when the velocity is higher. This must be ascribed to the maximum in the solvent flux also attaining its maximum at lower back-shock times.

The interplay between the various parameters and the back-shock times can be understood from looking at the path-lines during the back-shock period. This will be elaborated in the following section.

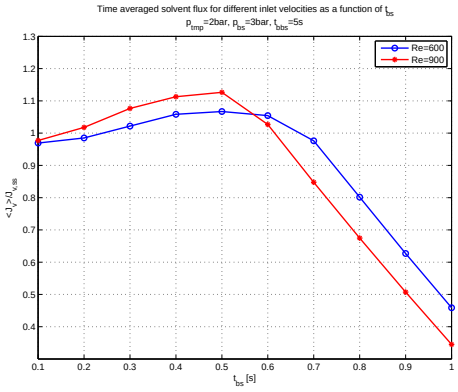


(a) Normalized solvent flux for different inlet velocities as a function of back-shock time.

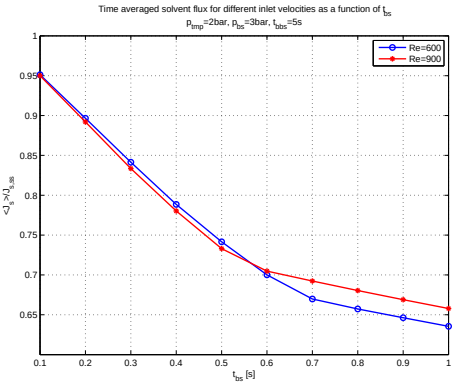


(b) Normalized solute flux for different inlet velocities as a function of back-shock time.

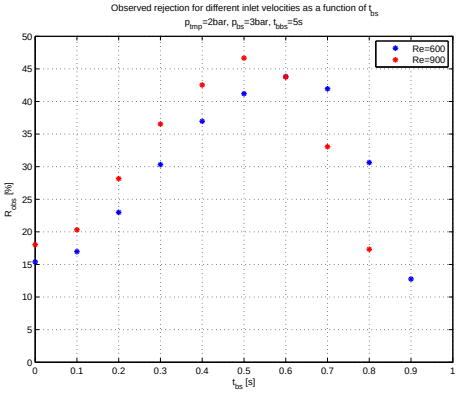


(c) Normalized solute flux for different inlet velocities as a function of back-shock time.

Figure 5.16: Normalized flux as a function of back-shock times for different back-shock pressures, $p_{tmp} = 2\text{bar}$, $p_{bs} = 3\text{bar}$, $t_{bbs} = 5s$. The figures shows: (a) The solvent flux, (b) The solute flux, (c) The observed rejection.

## 5.3 Upper estimate for the optimal back-shock time

In this section two upper estimates for the optimal back-shock time, as function of the parameters $p_{bs}$, $p_{tmp}$, $L_m$, $u_{in,av}$, and $\eta_s$, are given.

The hypothesis behind the estimates is that the path-line from the beginning of the membrane surface, during a back-shock cycle, should end at the other end of the membrane surface.

We will assume that the time-dependent solution has reached a periodic steady-state and confine ourselves to only one period, i.e., $t \in [0 : t_{bs} + t_{bbs}]$. Under this assumption a given concentration profile will exist when the back-shock is applied, $c(x, y, 0)$. This concentration profile will be polarized towards the membrane surface with the largest value at the membrane surface and exponentially decaying into the bulk of the hollow fibre. The width of the boundary layer, $\delta$, will be determined by the operating conditions.

Neglecting diffusion for now, the concentration in the boundary layer will be pushed into the bulk of the hollow fibre, forming an area of high concentration with a width comparable to the width of the boundary layer and a length equal to the length of the membrane. This area is convected away from membrane surface and downstream tangential to the membrane surface. Between the membrane and the highly concentrated area, the concentration is zero, due to the pure solvent flux into the hollow fibre. This is illustrated in figure 5.7. When the pressure is reversed the concentration field will be given by $c(x, y, t_{bs})$ and the area of high concentration will be convected towards the membrane and downstream tangential to the membrane until the area of high concentration has contact with the membrane surface. From here on the concentration polarization will build up on the membrane surface. This is illustrated in figure 5.8.

An upper estimate for the most beneficial set of parameters is then given when the path-line from $(0, 0)$ pass through $(L_m, 0)$. Notice, that path-lines from $(0, 0)$ that passes through $(\hat{L}_m, 0)$, where $\hat{L}_m > L_m$ will have been moved further away from the membrane surface, i.e., a larger amount of solvent is needed to be flushed into the hollow fibre during the back-shock period. This extra amount, however, will not result in any gain during forward pressure period, since the highly concentrated area will not have any contact with the membrane surface. Hence, this is an upper estimate.

### 5.3.1 Analytical calculations of path-lines

The tangential velocity component close to the membrane surface is approximated by a linear function

$$v_x(x,y) = ky\,. \tag{5.29}$$

Here, $k$ is given by the first order Taylor expansion presented in equation (5.6). I.e,

$$k = \frac{4u_{in,av}}{R} \tag{5.30}$$

During the back-shock period the velocity component perpendicular to the membrane surface close to the membrane is given by

$$v_y(x,y,t) = \begin{cases} A(p_{bs} - \tilde{p}(x) + \pi(c(x,0,t))) & \text{for} \quad 0 \le t \le t_{bs} \\ -A(p_{tmp} + \tilde{p}(x) - \pi(c(x,0,t))) & \text{for} \quad t_{bs} < t \le t_{bs} + t_{bbs}\,. \end{cases} \tag{5.31}$$

Here, $\tilde{p}(x)$ is the pressure drop needed to obtain a velocity tangential to the membrane surface, i.e., equation (5.13).

At the instance where the back-shock is applied the osmotic pressure will have an influence on the velocity. The concentration boundary layer is, however, removed fast compared to the back-shock time. Therefore, the osmotic pressure is neglected during back-shocking. When the pressure is reversed the concentration on the membrane surface is clean under the highly concentrated area until the time $T$, $t_{bs} < T < t_{bs} + t_{bbs}$, where the highly concentrated area is convected to the membrane surface. Since, we are interested in times less than or equal to this time, $t \le T$ the osmotic pressure can be neglected in equation (5.31). Hence,

$$v_y(x,y,t) = \begin{cases} A(p_{bs} - \tilde{p}(x)) & \text{for} \quad 0 \le t \le t_{bs} \\ -A(p_{tmp} + \tilde{p}(x)) & \text{for} \quad t_{bs} < t \le T\,. \end{cases} \tag{5.32}$$

From equation (5.13) we have

$$\tilde{p}(x) = \frac{8\eta_s L_m u_{in,av}}{R^2}\left(\frac{1}{2} - \frac{x}{L_m}\right) = \beta\left(\frac{1}{2} - \frac{x}{L_m}\right)\,. \tag{5.33}$$

Inserting this into equation (5.32) and rearranging we get

$$v_y(x,y) = \begin{cases} \frac{A\beta x}{L_m} + (Ap_{bs} - \frac{A\beta}{2})) & \text{for} \quad 0 \le t \le t_{bs} \\ \frac{A\beta x}{L_m} - (A(p_{tmp} + \frac{A\beta}{2})) & \text{for} \quad t_{bs} < t \le T\,. \end{cases} \tag{5.34}$$

Denoting $\gamma = \frac{A\beta}{L_m}$, $C_1 = (Ap_{bs} - \frac{A\beta}{2})$, and $C_2 = -(A(p_{tmp} + \frac{A\beta}{2})$, equation (5.34) can be written as

$$v_y(x,y) = \begin{cases} \gamma x + C_1 & \text{for} \quad 0 \le t \le t_{bs} \\ \gamma x + C_2 & \text{for} \quad t_{bs} < t \le T\,. \end{cases} \tag{5.35}$$

Using the expressions for the velocity given in equation (5.29) and equation (5.35) the path-line from (0,0) can be calculated. During back-shocking, $0 \le t \le t_{bs}$, the path-line is determined by the solution to the system of ordinary differential equations given in equation (5.36)

$$\begin{pmatrix} \dot{x} \\ \dot{y} \end{pmatrix} = \begin{pmatrix} 0 & k \\ \gamma & 0 \end{pmatrix} + \begin{pmatrix} 0 \\ C_1 \end{pmatrix}. \tag{5.36}$$

Here, the dot represents the derivative with respect to time. From standard ODE-theory[10] the solution is given by a solution to the homogeneous equation plus a particular solution to the inhomogeneous equation.

The solution to the homogeneous equation is given by

$$\begin{pmatrix} x_h(t) \\ y_h(t) \end{pmatrix} = c_1 \begin{pmatrix} 1 \\ \sqrt{\gamma/k} \end{pmatrix} e^{\sqrt{k\gamma}t} + c_2 \begin{pmatrix} 1 \\ -\sqrt{\gamma/k} \end{pmatrix} e^{-\sqrt{k\gamma}t}. \tag{5.37}$$

A particular solution to the inhomogeneous equation is given by

$$\begin{pmatrix} x_p(t) \\ y_p(t) \end{pmatrix} = \begin{pmatrix} -C_1/\gamma \\ 0 \end{pmatrix}. \tag{5.38}$$

The solution to equation (5.36) is then given by the sum of equation (5.37) and equation (5.38). Thus,

$$\begin{pmatrix} x(t) \\ y(t) \end{pmatrix} = c_1 \begin{pmatrix} 1 \\ \sqrt{\gamma/k} \end{pmatrix} e^{\sqrt{k\gamma}t} + c_2 \begin{pmatrix} 1 \\ -\sqrt{\gamma/k} \end{pmatrix} e^{-\sqrt{k\gamma}t} - \begin{pmatrix} C_1/\gamma \\ 0 \end{pmatrix}. \tag{5.39}$$

Since we are interested in the path-line from (0,0) the constants $c_1$ and $c_2$ are determined from $(x(0), y(0)) = (0,0)$. Hence,

$$c_1 = c_2 = \frac{C_1}{2\gamma}\,. \tag{5.40}$$

Inserting the values from equation (5.40) into equation (5.39) we have

$$\begin{pmatrix} x(t) \\ y(t) \end{pmatrix} = \frac{C_1}{2\gamma} \left[ \begin{pmatrix} 1 \\ \sqrt{\gamma/k} \end{pmatrix} e^{\sqrt{k\gamma}t} + \begin{pmatrix} 1 \\ -\sqrt{\gamma/k} \end{pmatrix} e^{-\sqrt{k\gamma}t} - \begin{pmatrix} 2 \\ 0 \end{pmatrix} \right]. \tag{5.41}$$

Especially, we have at the end of the back-shock period

$$\begin{pmatrix} x(t_{bs}) \\ y(t_{bs}) \end{pmatrix} = \frac{C_1}{2\gamma}\left[\begin{pmatrix} 1 \\ \sqrt{\gamma/k} \end{pmatrix} e^{\sqrt{k\gamma}t_{bs}} + \begin{pmatrix} 1 \\ -\sqrt{\gamma/k} \end{pmatrix} e^{-\sqrt{k\gamma}t_{bs}} - \begin{pmatrix} 2 \\ 0 \end{pmatrix}\right]. \tag{5.42}$$

When the pressure is reversed, $t > t_{bs}$ we define a new variable $\tau = t - t_{bs}$. The system of ordinary differential equations written from equation (5.29) and equation (5.35) is given by

$$\begin{pmatrix} \dot{x} \\ \dot{y} \end{pmatrix} = \begin{pmatrix} 0 & k \\ \gamma & 0 \end{pmatrix} + \begin{pmatrix} 0 \\ C_2 \end{pmatrix}. \tag{5.43}$$

Here, the dot represents differentiation with respect to $\tau$. This has the same functional form as equation (5.36) and therefore the general solution is the same. Thus,

$$\begin{pmatrix} x(\tau) \\ y(\tau) \end{pmatrix} = c_3 \begin{pmatrix} 1 \\ \sqrt{\gamma/k} \end{pmatrix} e^{\sqrt{k\gamma}\tau} + c_4 \begin{pmatrix} 1 \\ -\sqrt{\gamma/k} \end{pmatrix} e^{-\sqrt{k\gamma}\tau} + \begin{pmatrix} -C_2/\gamma \\ 0 \end{pmatrix}. \tag{5.44}$$

The constants $c_3$ and $c_4$ are to be determined from $(x(\tau = 0), y(\tau = 0)) = x(t_{bs}, y(t_{bs}))$. Calculations reveal that

$$c_3 = \frac{C_1\left(e^{\sqrt{k\gamma}t_{bs}} - 1\right) + C_2}{2\gamma} \tag{5.45}$$

and

$$c_4 = \frac{C_1\left(e^{-\sqrt{k\gamma}t_{bs}} - 1\right) + C_2}{2\gamma}. \tag{5.46}$$

Hence, the solution as a function of $\tau$ is given by

$$\begin{aligned}\begin{pmatrix} x(\tau) \\ y(\tau) \end{pmatrix} = \frac{1}{2\gamma}\Bigg\{&\left[C_1\left(e^{\sqrt{k\gamma}t_{bs}} - 1\right) + C_2\right]\begin{pmatrix} 1 \\ \sqrt{\gamma/k} \end{pmatrix} e^{\sqrt{k\gamma}\tau} \\ &+ \left[C_1\left(e^{-\sqrt{k\gamma}t_{bs}} - 1\right) + C_2\right]\begin{pmatrix} 1 \\ -\sqrt{\gamma/k} \end{pmatrix} e^{-\sqrt{k\gamma}\tau} - \begin{pmatrix} 2C_2 \\ 0 \end{pmatrix}\Bigg\}.\end{aligned} \tag{5.47}$$

We now seek the path-line that as a function of the parameter $t_{bs}$ passes through the point $(L_m, 0)$. Denoting the time it takes to reach the point as $\tau_0$ we solve

the system of equations

$$\begin{pmatrix} L_m \\ 0 \end{pmatrix} = \frac{1}{2\gamma}\left\{\left[C_1\left(e^{\sqrt{k\gamma}t_{bs}}-1\right)+C_2\right]\begin{pmatrix} 1 \\ \sqrt{\gamma/k} \end{pmatrix} e^{\sqrt{k\gamma}\tau_0} + \left[C_1\left(e^{-\sqrt{k\gamma}t_{bs}}-1\right)+C_2\right]\begin{pmatrix} 1 \\ -\sqrt{\gamma/k} \end{pmatrix} e^{-\sqrt{k\gamma}\tau_0} - \begin{pmatrix} 2C_2 \\ 0 \end{pmatrix}\right\}. \tag{5.48}$$

Solving the equation for $y(\tau_0) = 0$ gives

$$\tau_0 = \frac{1}{2\sqrt{k\gamma}}\left[\ln\left(\frac{C_1\left(e^{-\sqrt{k\gamma}t_{bs}}-1\right)+C_2}{C_1\left(e^{\sqrt{k\gamma}t_{bs}}-1\right)+C_2}\right)\right] \tag{5.49}$$

Inserting this in the equation $x(\tau_0) = L_m$ and solving for $t_{bs}$, tedious calculations reveal there are several solutions. We are, however, only interested in the one solution that gives a positive real number. This solution is given by

$$t_{bs} = \frac{1}{\sqrt{k\gamma}} 2\ln\left[\frac{1}{\sqrt{2}}\left(\frac{\xi+\sqrt{\chi}}{C_1\left(C_1-C_2\right)}\right)^{1/2}\right], \tag{5.50}$$

where

$$\xi = -\left(L_m\gamma\right)^2 - 2C_2L_m\gamma + 2C_1 - C_1C_2 \tag{5.51}$$

and

$$\chi = \left(L_m\gamma\right)\left(L_m\gamma+2C_2\right)\left(L_m\gamma+2C_1\right)\left(L_m\gamma-2C_1+2C_2\right). \tag{5.52}$$

This relatively simple expression gives an upper estimate for the optimal back-shock time needed to maximize the volumetric flux. Hence, given the parameters $R$, $L_m$, $A$, $p_{tmp}$, $p_{bs}$, $\eta_s$ and $u_{in,av}$ the back-shock time can be calculated.

### 5.3.2 Results

In this section the back-shock times calculated from equation (5.50) are presented. We will vary one parameter at a time and show how the path-line and the back-shock time vary when this parameter is varied, and all other parameters are constant. Notice, however, that in principle the estimate for the back-shock time is a hyper-surface in $\mathbb{R}^n$, where $n$ is the number of parameters allowed to be varied. In the end of this section a back-shock estimate for the parameters used in the simulations presented in section 5.2.3 will be calculated and related to the simulations.

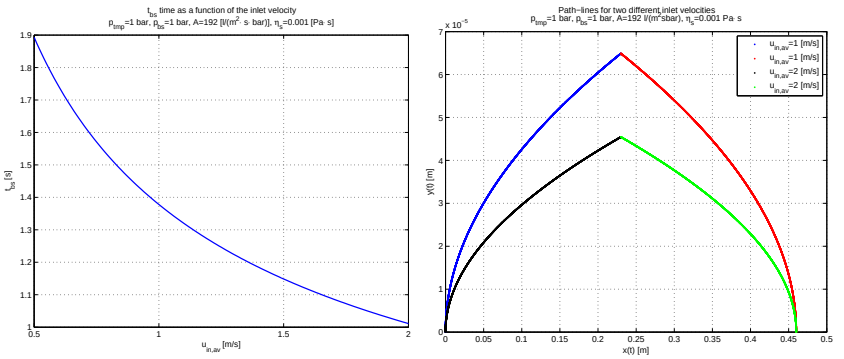


(a) Estimate of the back-shock time as a function of the inlet velocity.

(b) Path-lines for two different inlet velocities.

Figure 5.17: Estimate for the back-shock time and path-lines for different inlet velocities.

In figure 5.17a is shown how the estimate for the back-shock time varies as a function of the inlet velocity.

As seen in figure 5.17a the back-shock time decreases as the inlet velocity is increased. This is because the velocity component tangential to the membrane surface is increased. Hence, the path-line from $(0, 0)$ to $(L_m, 0)$ reaches a smaller $y$-value, i.e., perpendicular to the membrane surface. Hence, a smaller back-shock time is needed. This is illustrated in figure 5.17b.

In figure 5.18a the estimate for the back-shock time is shown for different transmembrane pressures. As seen a higher transmembrane pressure requires a higher back-shock time. Again this can be explained by looking at the path-lines. In figure 5.18b the path-lines are shown for two different transmembrane pressures. When the transmembrane pressure is higher, the path-line towards the membrane after back-shocking is steeper. Hence, a higher back-shock time is needed for the path-line to coincide with the membrane surface at $(L_m, 0)$. Also, it is seen that the path-lines follows the same path during back-shocking. The path-line for the lowest transmembrane pressure is, however, extended further due to the increased back-shock time.

In figure 5.19a the estimate for the back-shock time is shown for different back-shock pressures. As seen the back-shock time decreases when the back-shock pressure is increased. This is because the velocity away from the membrane is higher when the back-shock pressure is higher. Hence, the path-line moves faster away from the membrane surface. Thus, a shorter back-shock time is needed. This is illustrated in figure 5.19b.

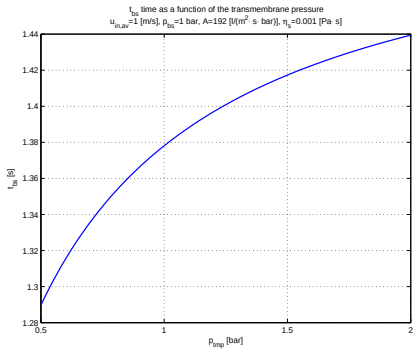


(a) Estimate of the back-shock time as a function of the transmembrane pressure.

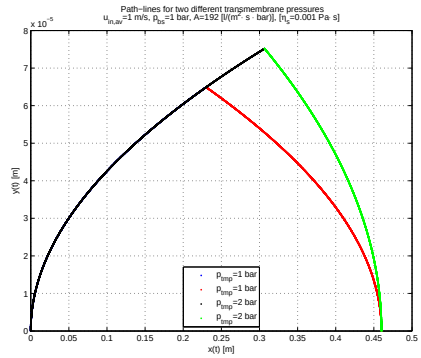


(b) Path-lines for two different transmembrane pressures.

Figure 5.18: Estimate for the back-shock time and path-lines for different transmembrane pressures.

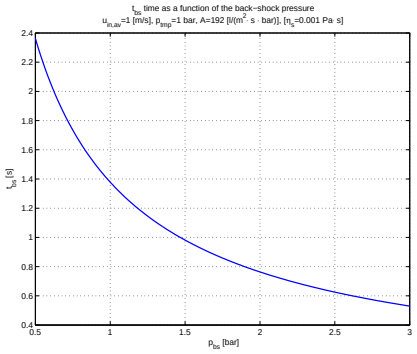


(a) Estimate of the back-shock time as a function of the backshock pressure.

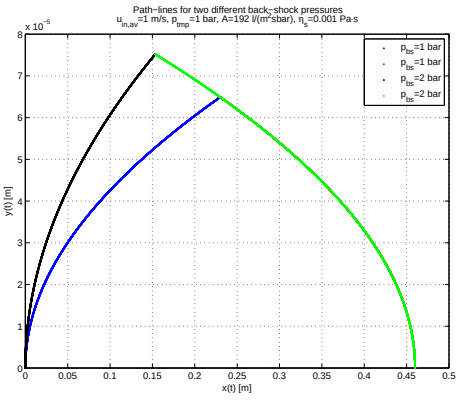


(b) Path-lines for two different back-shock pressures.

Figure 5.19: Estimate for the back-shock time and path-lines for different back-shock pressures.

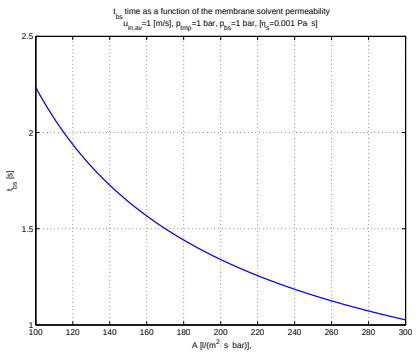


(a) Estimate of the back-shock time as a function of membrane permeability.

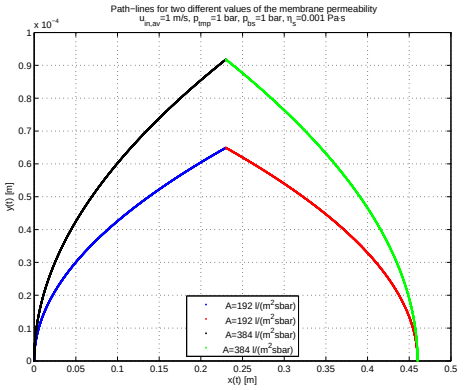


(b) Path-lines for two different solvent permeabilities.

Figure 5.20: Estimate for the back-shock time and path-lines for differerent membrane permeabilities.

In figure 5.20a the estimate for the back-shock time is shown for different values of the solvent permeability.

As seen the back-shock time decreases when the solvent permeability increases. Again this is due to the increased velocities both during back-shock and during forward separation. Two path-lines with different values of the solvent permeability is shown in figure 5.20b.

In figure 5.21a we show the estimate for the back-shock time as a function of the viscosity.

As compared to solving the Navier-Stokes equation the viscosity does not appear directly in the equations that govern the velocity field. It does, however, appear implicitly in the pressure drop down the axial length of the hollow fibre. Hence, a higher solvent viscosity requires a larger pressure drop in order to maintain a given average inlet velocity. Since the pressure drop is symmetric around $L_m/2$ an increased pressure drop implies a smaller velocity away from the membrane during back-shocking and a smaller velocity towards the membrane during forward separation. Hence, longer back-shock times are needed. This is indeed also what is seen in figure 5.21a. The longer back-shock time implies that the path-lines travel further away from the membrane, i.e., to larger values of $y$. This is illustrated for two different viscosities in figure 5.21b.

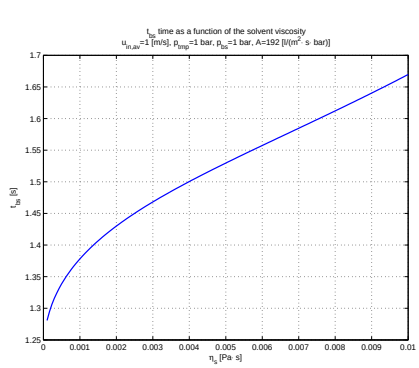


(a) Estimate of the back-shock time as a function of solvent viscosity.

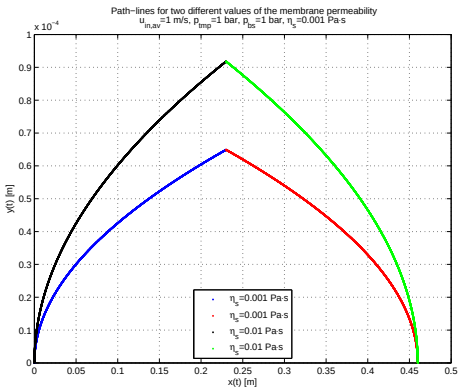


(b) Path-lines for two different solvent viscosities.

Figure 5.21: Estimate for the back-shock time and path-lines for different solvent vicosities.

## 5.4 Simplified analytical calculations

For the parameter values used in this thesis, the axial pressure drop needed to maintain a given average inlet velocity into the hollow fibre, is small compared to both the transmembrane pressure and the back-shock pressure. Therefore, it is a reasonable approximation to neglect this pressure. This greatly simplifies the solution to the path-lines from $(0, 0)$ to $(L_m, 0)$. With this approximation we have the velocity component tangential to the membrane given by equation (5.29)

$$v_x(x, y) = ky\,, \tag{5.53}$$

and the velocity component perpendicular to the membrane surface given by

$$v_y(x, y, t) = \begin{cases} Ap_{bs} & \text{for} \quad 0 \leq t \leq t_{bs} \\ -Ap_{tmp} & \text{for} \quad t_{bs} < t \leq T\,. \end{cases} \tag{5.54}$$

Hence, during back-shocking the $y$-coordinate is simply given by

$$y(t) = Ap_{bs}t\,, \tag{5.55}$$

and the $x$-coordinate is given by

$$x(t) = \frac{1}{2}kAp_{bs}t^2\,. \tag{5.56}$$

Especially, the position after the back-shock is given by

$$\begin{pmatrix} x(t_{bs}) \\ y(t_{bs}) \end{pmatrix} = Ap_{bs} \begin{pmatrix} \frac{k}{2}t_{bs}^2 \\ t_{bs} \end{pmatrix} . \tag{5.57}$$

Again we define the variable $\tau = t - t_{bs}$. When the pressure is reversed the $y$-coordinate as a function of $\tau$ is given by

$$y(\tau) = y(t_{bs}) + \int_0^\tau v_y ds = A(p_{bs}t_{bs} - p_{tmp}\tau) . \tag{5.58}$$

Furthermore, the $x$-component as a function of $\tau$ is given by

$$x(\tau) = x(t_{bs}) + k\int_0^\tau y(s)ds = \frac{kA}{2}\left(p_{bs}t_{bs}^2 - p_{tmp}\tau^2 + 2p_{bs}t_{bs}\tau\right) . \tag{5.59}$$

Thus, we have

$$\begin{pmatrix} x(\tau) \\ y(\tau) \end{pmatrix} = A \begin{pmatrix} \frac{k}{2}\left(p_{bs}t_{bs}^2 - p_{tmp}\tau^2 + 2p_{bs}t_{bs}\tau\right) \\ p_{bs}t_{bs} - p_{tmp}\tau \end{pmatrix} . \tag{5.60}$$

We seek the time $\tau_0$ such that $(x(\tau_0), y(\tau_0)) = (L_m, 0)$. Hence,

$$\tau_0 = \frac{p_{bs}}{p_{tmp}}t_{bs} , \tag{5.61}$$

and

$$\frac{Ak}{2}\left(p_{bs}t_{bs}^2 - p_{tmp}\left(\frac{p_{bs}}{p_{tmp}}t_{bs}\right)^2 + 2p_{bs}t_{bs}\frac{p_{bs}}{p_{tmp}}t_{bs}\right) - L_m = 0 . \tag{5.62}$$

Calculations reveal

$$t_{bs}^2 = \frac{2L_m}{kAp_{bs}\left(1 + {}^{p_{bs}}/_{p_{tmp}}\right)} , \tag{5.63}$$

and since we are only interested in the positive root

$$t_{bs} = \sqrt{\frac{2L_m}{kAp_{bs}\left(1 + {}^{p_{bs}}/_{p_{tmp}}\right)}} . \tag{5.64}$$

The time it takes for the fluid parcel starting at $(0, 0)$ and following the path-line described above will be given by $T = t_{bs} + \tau_0$. Hence, from equation (5.61) we have

$$T = \left(1 + \frac{p_{bs}}{p_{tmp}}\right)t_{bs}, \tag{5.65}$$

inserting the expression for $t_{bs}$, equation (5.64), we have

$$T = \sqrt{\frac{2L_m\left(1 + {}^{p_{bs}}/_{p_{tmp}}\right)}{kAp_{bs}}}\,. \tag{5.66}$$

The total time is obviously decreasing for increasing values of $k$ and $A$ and decreasing for decreasing values of $L_m$. It is, however, also decreasing for increasing values of $p_{tmp}$ and $p_{bs}$ which can be seen from

$$\frac{\partial T}{\partial p_{tmp}} = \frac{-L_m}{kAp_{tmp}^2}\frac{1}{\sqrt{\frac{2L_m\left(1+{}^{p_{bs}}/_{p_{tmp}}\right)}{kAp_{bs}}}} < 0\,, \tag{5.67}$$

and

$$\frac{\partial T}{\partial p_{bs}} = \frac{-L_m kA}{\sqrt{\frac{2L_m\left(1+{}^{p_{bs}}/_{p_{tmp}}\right)}{kAp_{bs}}}} < 0\,. \tag{5.68}$$

### 5.4.1 Flux regain

If diffusion is neglected one can give an estimate of the amount of solvent that is regained as pure solvent flux during a period of back-shocking.

Since there is a flux of pure solvent into the hollow fibre during back-shocking, the concentration of the fluid between the membrane surface and the highly concentrated area during back-shocking is zero (see, e.g. figure 5.8). When the pressure is reversed there will be a pure solvent flux through the membrane as long as there is no concentration on the membrane. Essentially, this means that the area underneath a given path-line returns through the membrane as pure solvent flux.

The amount of pure solvent that flows into the hollow fibre during back-shocking is well approximated by

$$\phi_l = L_m A p_{bs} t_{bs}\,. \tag{5.69}$$

The regain as pure solvent flux given by the area under the path-line, i.e.,

$$\phi_g = \int_0^{L_m} y(x)dx\,. \tag{5.70}$$

As shown in appendix D the ratio between the gain and the loss when the velocity field is given by equation (5.53) and equation (5.54) is given by

$$\frac{\phi_g}{\phi_l} \leq \frac{2}{3}\,. \tag{5.71}$$

Here, the equality holds when the back-shock time is given by equation (5.64).

Essentially, this means that in order to have a positive effect during a back-shock cycle, the remaining one third must be recovered during the concentration build up on the membrane surface.

So far the diffusion has been neglected. In the next section we will discuss the effect of diffusion in relation to the estimate.

### 5.4.2 Diffusion

Essentially the diffusion takes place in two dimensions. The diffusion, however, depends on the concentration gradients which are much larger in the direction perpendicular to the membrane. Therefore, the diffusion can be expected to be reasonably explained by diffusion of a point mass in one direction.

As shown in appendix C the diffusion of a point mass in one dimension with with constant velocity $u$ is given by

$$\hat{c}(\hat{y},\hat{t}) = \frac{\hat{M}}{\sqrt{4\pi\frac{1}{\mathrm{Pe}_{bl}}\hat{t}}}\exp\left(-\frac{\left(\hat{y}-\hat{J}_v\hat{t}\right)^2}{4\frac{1}{\mathrm{Pe}_{bl}}\hat{t}}\right). \tag{5.72}$$

Here

$$\hat{c}(0,0) = M\delta(\hat{y}), \tag{5.73}$$

where $\delta(\hat{y})$ is the Kronecker delta function.

At steady-state the concentration profile perpendicular to the membrane surface is reasonably approximated by the solution to the one dimensional continuity equation for the solvent with average values used as boundary conditions and for the velocity component perpendicular to the membrane surface,

$$\frac{d\hat{c}_{ss}}{d\hat{y}} + \frac{1}{\mathrm{Pe}_{bl}J_{v,ss}}\frac{d^2\hat{c}_{ss}}{d\hat{y}^2} = 0\,. \tag{5.74}$$

with the boundary conditions $c_{ss}(0,\hat{x}) = \hat{c}_{m,av}$ and $\lim_{y\to\infty} c_{ss}(\hat{y},\hat{x}) = 1$. Here, $J_{v,ss}$ is the average solvent flux and $\hat{c}_{m,av}$ is the average concentration on the membrane surface.

The solution to equation (5.74) with the boundary conditions described above is given by

$$\hat{c}_{ss}(\hat{y}) = 1 + (\hat{c}_{m,av}-1)\exp\left(-\frac{\hat{y}}{\mathrm{Pe}_{bl}J_{v,ss}}\right) \tag{5.75}$$

The extra mass within the boundary layer due to the concentration polarization can then be approximated by

$$\hat{M} \approx \int_0^\infty (\hat{c}_s s(\hat{y}) - 1) d\hat{y} = (\hat{c}_{m,av} - 1)\mathrm{Pe}_{bl} J_{v,ss} \,. \tag{5.76}$$

Inserting equation (5.76) into equation (5.72) we have

$$\hat{c}(\hat{y}, \hat{t}) = \frac{(\hat{c}_{m,av} - 1)}{\sqrt{4\pi \mathrm{Pe}_{bl} J_{v,ss} \hat{t}}} \exp\left( - \frac{\left(\hat{y} - \hat{J}_v \hat{t}\right)^2}{4 \frac{1}{\mathrm{Pe}_{bl}} \hat{t}} \right) . \tag{5.77}$$

Taking $J_v = A p_{bs}$ during back-shocking and $-A p_{tmp}$ during forward filtration we can relate this expression to the simulations.

This is done for a the simulation with Re = 900, $p_{tmp} = p_{bs} = 2$bar, and $t_{bs} = 0.6$s. From the simulations the steady-state average concentration on the membrane surface and the steady-state average solvent flux is calculated to be $\hat{c}_{m,av} = 109$ and $\hat{J}_{v,ss} = 2.84$. Notice that the average volumetric flux can be measured, and the average concentration can be found given a known expression for the osmotic pressure, in an experiment.

In figure 5.22 we show the analytical estimate given here compared to the result from the simulation perpendicular to the membrane at $\hat{x} = 1$. Because of the influx of pure solvent during back-shocking the concentration distribution in the simulations tends to zero towards the membrane and to one away from the membrane. The expression for the diffusion given here tends to same value on both sides. Therefore, in figure 5.22a the calculated distribution that tends to zero is shown, i.e., equation (5.77), and in figure 5.22b the distribution that tends to one is shown, i.e., the expression in equation (5.77) plus one.

As seen there is a reasonable agreement between the analytical result and the simulations. It seems, however, as if the diffusion is slightly faster in the simulation compared to the analytic expression. This is probably due to two things. Firstly, the simulations are done in a two dimensional domain, and small gradients could be present in the direction parallel to the membrane. This is definitely the case for the concentration in the fluid parcel that has position (0,0) just before back-shocking. Secondly, some shear induced diffusion is present.

Nevertheless, it is seen that the concentration remains more located for shorter times. This indicates that the estimate of the back-shock time will be a better approximation when the path-line is completed in short time compared to longer times. I.e., small times in equation (5.66). As mentioned short times will

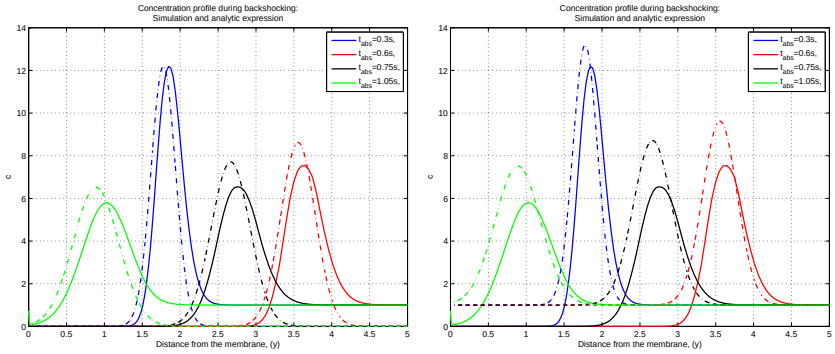


(a) Concentration from the simulation against analytical expression. The analytical expression tends to one on both sides.

(b) Concentration from the simulation against analytical expression. The analytical expression tends to one on both sides.

Figure 5.22: Analytical expression for the diffusion against simulation. The full lines are results of the simulation whereas the dotted lines are the analytical expression. The simulation used has the parameter values Re = 900, $p_{tmp} = p_{bs} = 2$bar, and $t_{bs} = 0.6$s, and the concentration is shown perpendicular to the membrane at $\hat{x} = 1$. In both figures $t_{abs}$ is the time after the back-shock is applied.

corresponds to to high back-shock pressure, high transmembrane pressure, and high inlet velocities.

## 5.5 Relation between the back-shock estimate and the simulations

In this section the estimate for the back-shock time is given for the simulations made in section 5.2.3.2. Here the inlet velocity was given by 0.8661 and 1.2992 $^{m}/_{s}$, corresponding to a Reynolds number of 600 and 900 respectively. For each inlet velocity the transmembrane pressure was given by $p_{tmp} = (0.5, 1, 2)$bar and the back-shock pressure was given by $p_{bs} = (0.5, 1, 2, 3)$bar.

Therefore we present two tables, one for each time estimate. In both tables, we present two tables, one for each inlet velocity. For all four tables, the back-shock pressure is increasing in the vertical direction and the transmembrane pressure is increasing in the horizontal direction. In the centre of the table is given the back-shock estimate.

The back-shock time estimate from equation (5.50) is given in table 5.1.

When comparing table 5.2a with table 5.1a, and table 5.2b with table 5.1b, it is seen that there is almost no difference between the two estimates. As mentioned, this is because the pressure drop needed to maintain a tangential velocity is small compared to both the transmembrane pressures and the back-shock pressures used in the simulations. It should be noted, however, that the estimate from equation (5.64) is smaller than the estimate from equation (5.64). This is because, when we neglect the pressure drop in the axial direction there is a larger lift for $x < {}^{L_m}/_{2}$ during backshocking. Moreover, there is a larger velocity towards the membrane for $x > {}^{L_m}/_{2}$. Both contribute to a smaller estimate for the back-shock time.

Since, the two estimates are so close to each other the relation to the simulations

| $p_{bs}$ \ $p_{tmp}$ | 0.5 | 1 | 2 |
|---|---|---|---|
| 0.5 | 1.92 | 2.21 | 2.42 |
| 1 | 1.09 | 1.34 | 1.54 |
| 2 | 0.60 | 0.77 | 0.94 |
| 3 | 0.41 | 0.54 | 0.69 |

(a) Estimate of $t_{bs}$ from equation (5.50), $u_{in,av} = 0.8661^{m}/_{s}$ (Re=600).

| $p_{bs}$ \ $p_{tmp}$ | 0.5 | 1 | 2 |
|---|---|---|---|
| 0.5 | 1.59 | 1.83 | 2.00 |
| 1 | 0.90 | 1.10 | 1.27 |
| 2 | 0.49 | 0.63 | 0.77 |
| 3 | 0.34 | 0.44 | 0.56 |

(b) Estimate of $t_{bs}$ from equation (5.50), $u_{in,av} = 1.2992^{m}/_{s}$ (Re=900).

Table 5.1: Estimate for the back-shock time from equation (5.50) using the parameters used in section 5.2.3.2.

| $p_{bs}$ \ $p_{tmp}$ | 0.5 | 1 | 2 |
|---|---|---|---|
| 0.5 | 1.87 | 2.16 | 2.36 |
| 1 | 1.08 | 1.32 | 1.52 |
| 2 | 0.59 | 0.76 | 0.93 |
| 3 | 0.41 | 0.54 | 0.68 |

(a) Estimate of $t_{bs}$ from equation (5.64), $u_{in,av} = 0.8661^{\mathrm{m}}/_{\mathrm{s}}$ (Re=600).

| $p_{bs}$ \ $p_{tmp}$ | 0.5 | 1 | 2 |
|---|---|---|---|
| 0.5 | 1.52 | 1.76 | 1.93 |
| 1 | 0.88 | 1.08 | 1.24 |
| 2 | 0.48 | 0.62 | 0.77 |
| 3 | 0.33 | 0.44 | 0.56 |

(b) Estimate of $t_{bs}$ from equation (5.64), $u_{in,av} = 1.2992^{\mathrm{m}}/_{\mathrm{s}}$ (Re=900).

Table 5.2: Estimate for the back-shock time from equation (5.2.3.2) using the parameters used in section 5.64.

can be done as one.

In figure 5.13a it is seen that the back-shock time increases as a function of transmembrane pressure as predicted by the estimate. Moreover, the optimal back-shock time is slightly lower than the estimate. It should, however, be remembered that it is an upper estimate. Therefore, this is in good agreement with the predictions. Furthermore, the optimal back-shock time and the upper estimate are comparable. Moreover, it can be argued that a decrease should be seen for back-shock times larger than the upper estimate. In fact the decrease should be proportional to the additional back-shock time. This is because back-shock times larger than the estimate, will correspond to an influx into the hollow fibre that has no effect on the forward filtration, and this extra influx is proportional to the back-shock time. This is also seen in figure 5.13a. Furthermore, a similar argument holds for the solute flux. For back-shock times larger than the estimate, the total amount of solute that passes through the membrane during forward filtration is a constant, $C_1$. Hence, the time averaged concentration would be given by

$$\langle J_s \rangle = \frac{C_1}{t_{bbs} + t_{bs,e} + t_{additonal}}\,, \tag{5.78}$$

where, $t_{bs,e}$ is the back-shock estimate and $t_{additional}$ is additional back-shock time. Since, $t_{additional}$ is small compared to $t_{bbs} + t_{bs,e}$ a first order expansion will give a linearity in the time averaged solute flux.

$$\langle J_s \rangle \approx \frac{C_1}{t_{bbs} + t_{bs,e}} - \frac{C_1}{(t_{bbs} + t_{bs,e})^2} t_{additonal}\,. \tag{5.79}$$

This is also seen in figure 5.13b.

In figure 5.14 the effect of different back-shock pressures was investigated. The optimal time was decreasing for increasing back-shock pressures. This is also

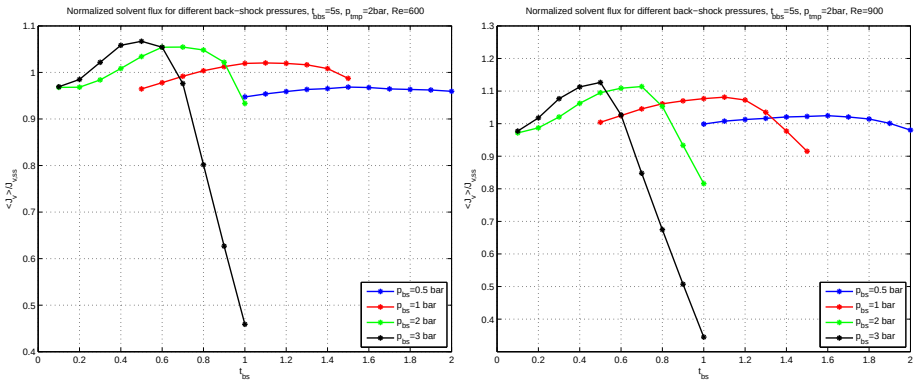


(a) Normalized solvent flux for different back-shock pressures as a function of back-shock time, Re = 600.

(b) Normalized solvent flux for different back-shock pressures as a function of back-shock time, Re = 900.

Figure 5.23: Normalized flux as a function of back-shock times for different back-shock pressures, $p_{tmp} = 2\text{bar}$, $t_{bbs} = 5s$. The figures shows the effect for two different inlet velocities: (a) Re = 600, (b) Re = 900.

predicted by the back-shock time estimate. As argued the estimate should be more precise for high back-shock pressures. This is also seen; the simulation showed an optimal back-shock time of 0.3s using a back-shock pressure of 1bar and an inlet velocity corresponding to Re = 900. For these values the upper estimate is 0.44s. Moreover, the linearly decreasing effect in both solute and solvent flux is seen for back-shock times higher than the estimated back-shock times.

In figure 5.16 the effect of different inlet velocities was investigated. As predicted by the back-shock time seems decreasing for increasing velocities. Furthermore, the characteristic straight lines are seen for back-shock times higher than the back-shock estimate.

The knowledge obtained from the analysis made so far in this chapter gives a reasonable idea as to where the optimal back-shock time is to be found. I.e., use the estimate and go to smaller back-shock times. To illustrate this additional simulations have been made, where the transmembrane pressure is 2bar and the inlet velocity and the back-shock pressure is varied. Using the back-shock estimates the maximum is easily found. This can be seen in figure 5.23.

Lastly, it should be mentioned that it has been observed that when combining the parameters $t_{bs}$ and $p_{bs}$ into a single parameter $\alpha = p_{bs}t_{bs}$ an approximate collapse of the curves has been observed. The parameter $\alpha$ is a measure of the

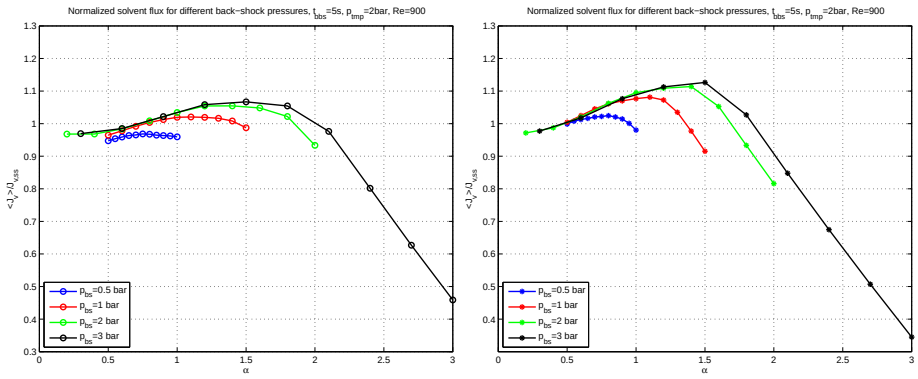


(a) Normalized solvent flux as a function of $\alpha$, Re = 600.

(b) Normalized solvent flux as a function of $\alpha$, Re = 900.

Figure 5.24: Normalized flux as a function of $\alpha$, $p_{tmp} = 2\text{bar}$, $t_{bbs} = 5s$. The figures show the effect for two different inlet velocities: (a) Re = 600, (b) Re = 900.

total solvent flux into the hollow fibre during the back-shock period. This is illustrated by scaling the figures in figure 5.23 and seen in figure 5.24. As seen there is an excellent collapse for Re = 900 whereas for Re = 600 the collapse is a bit less obvious. This tendency has been observed throughout the simulations.

It should be noted that the shape of the curves presented in figure 5.24 is similar to those showing the effect of changing the transmembrane pressure presented in figure 5.13a.

## 5.6 Discussion and conclusions on the 2D-model

The 2-dimensional model presented here was a relatively simple model. We approximated the velocity tangential to the membrane surface as linearly increasing as a function of distance. Moreover, we defined the velocity field perpendicular to the membrane such that it only depended on the pressure and the concentration on the membrane. Neither of these two things are expected to be true in a model that solves the full Navier-Stokes equation.

The model was able to produce a positive effect on both the volumetric flux and the observed rejection when measured against the steady-state solution. It was seen that the greatest effect was obtained for high back-shock pressures,

high transmembrane pressures, high inlet velocities. Moreover, the optimal back-shock time decreased for increasing inlet velocities, increasing back-shock pressures and increasing transmembrane pressure. Furthermore, when combining the back-shock time and the back-shock pressure into a single variable, $\alpha$, the curves of the flux seemed to follow the same curve. On this curve, however, smaller values of the transmembrane pressure would bend of earlier, giving the highest effect for high transmembrane pressures.

Furthermore, it was possible to conclude that an increase in time between back-shocking had very little effect on the average solvent flux and the optimal back-shock time. It did, however, have a significant decreasing effect on the observed rejection. From this it could be deduced that already after a time between back-shocking of 5s the concentration field is close to the concentration field of the steady-state solution. We can, however, not say if a higher effect could be obtained for smaller values of the time between back-shocking.

Moreover, an analytical expression that predicts an estimate for the optimal back-shock time was introduced. This estimate was build on the assumption that the back-shock time should be chosen such that the path-line, that a fluid parcel in $(0, 0)$ at the initiation of the back-shock, would return to the membrane at $(L_m, 0)$. It could be argued that this is an upper estimate, since longer times would result in an additional loss due to transport of pure solvent through the outlet. It was seen that this estimate was most accurate when the time it took to follow the path-line was smallest.

This could be understood by looking at the diffusion. The diffusion of the highly concentrated solute area was reasonably described by diffusion of a point mass in one dimension, when the point mass was calculated from the steady-state solution. Therefore, the concentrated area is more confined and having a higher peak-value when returning to the membrane for shorter times compared to longer times.

## 5.7 3D model

In the 3D-model the incompressible Navier-Stokes equation is solved along with the continuity equation for the solute and the solvent, where axial symmetry is assumed. Moreover, the viscosity will be allowed to depend on the concentration. Because of the increased computational effort it has been necessary to restrict ourselves to a hollow fibre with a membrane length of 14 cm. In addition to this we model an inlet and an outlet of 3.5cm. An illustration of a single hollow fibre in the $rz$-plane is shown in figure 5.25, where $z_1 = 3.5$cm and $z_2 = 17.5$cm.

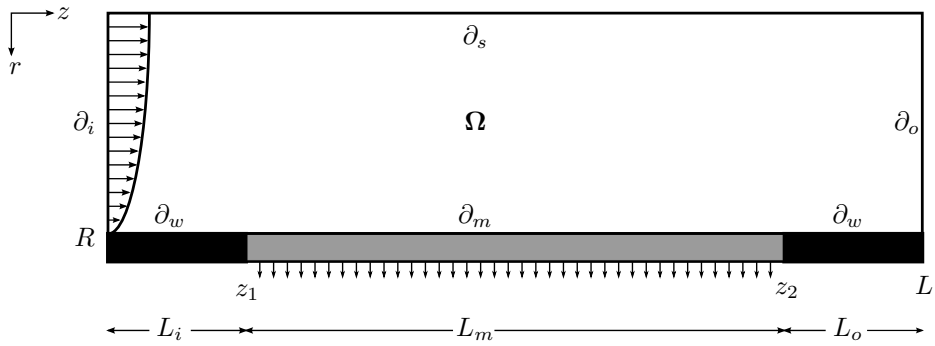


Figure 5.25: Illustration the hollow fibre tube. The tube has radius $R$ and the permeable membrane is situated between $z_1$ and $z_2$. The impermeable inlet is situated between 0 and $z_1$. And, the impermeable outlet is situated between $z_2$ and $L$.

Furthermore, it has been necessary to confine ourselves to simulating only one back-shock period. Therefore, we will solve the steady-state equation and use this result as the initial condition for the time-dependent study. Hence, these simulations are an approximation to the periodic solution that will occur after a few back-shock cycles. This approximation is best when the time between back-shock is so long that the concentration field just before a back-shock is applied, in the periodic solution, is close to the steady-state solution. From the 2D-model it was shown that a for a time between back-shocking of $t_{bbs} = 5s$ this seemed to be the case. Hence, all simulations in this section have been done with this value of the time between back-shocking.

### 5.7.1 Equations of motion

Within the bulk of the hollow fibre the equations of motion are the continuity equation of solute and solvent and the momentum equation. The continuity equation for the solvent is

$$\nabla \cdot \boldsymbol{v} = 0\,. \tag{5.80}$$

The continuity equation for the solute is

$$\frac{\partial c}{\partial t} + \boldsymbol{v} \cdot \nabla c = D\nabla^2 c\,, \tag{5.81}$$

where $D$ is the diffusion coefficient of the solute.

The momentum equation is

$$\rho\left(\frac{\partial \boldsymbol{v}}{\partial t}+\boldsymbol{v}\cdot\nabla\boldsymbol{v}\right)=\nabla\cdot\boldsymbol{\Pi}\,, \tag{5.82}$$

where $\rho$ is the density of the solvent and $\boldsymbol{\Pi}$ is the total stress tensor and is given by

$$\boldsymbol{\Pi}=p\boldsymbol{I}+\eta(c)\left(\nabla\boldsymbol{v}+(\nabla\boldsymbol{v})^{T}\right)\,, \tag{5.83}$$

where $\boldsymbol{I}$ is the $3\times3$ unit matrix and $\eta(c)$ is the concentration-dependent viscosity of the fluid.

The concentration-dependent viscosity will be given by equation (2.5), presented in section 2.1.1 using a molecular weight of 500 kDa. I.e.,

$$\eta=\eta_s\left(1+\alpha_v\left(K'M_w^a c+k'\left(K'M_w^a\right)^2c^2\right)\right)\,. \tag{5.84}$$

Here, $\alpha_v=\{0,1\}$ and is used to simulate either a concentration dependent viscosity or a constant viscosity. I.e., when $\alpha_v=0$ the viscosity is constant and equal to the solvent viscosity, and for $\alpha_v=1$ the viscosity is concentration dependent.

## 5.7.2 Boundary conditions

The boundary conditions in the hollow fibre can be divided into five distinctive boundaries.

### 5.7.2.1 The inlet

At the inlet of each hollow fibre there is essentially a plug flow with an average velocity $u_{in,av}$. The flow then gradually develops into a Poiseuille flow. As in the stationary model presented in chapter 4 we assume a fully developed Poiseuille flow at the inlet. Hence, at the inlet, $\partial_i=\{r,z\,|z=0\}$, the boundary condition on the velocity will be a fully developed Poiseuille flow with a known average velocity, $u_{in,av}$. I.e.,

$$\boldsymbol{v}(r,0,t)=2u_{in,av}\left(1-\left(\frac{r}{R}\right)^2\right)\,. \tag{5.85}$$

Furthermore, the boundary condition on the concentration will be uniform and equal to the inlet concentration, i.e.,

$$c(r,0,t)=c_{in}\,. \tag{5.86}$$

#### 5.7.2.2 The outlet

At the outlet, $\partial_o = \{r, z \,|z = L\}$, there will be a condition on the pressure

$$p(r, L, t) = p_{out}\,. \tag{5.87}$$

Moreover, the boundary condition on the concentration will be

$$\nabla c \cdot \boldsymbol{n} = 0 \tag{5.88}$$

where $\boldsymbol{n}$ is the outward normal vector.

#### 5.7.2.3 The edge of the hollow fibre

The edge of the hollow fibre $\partial_e = \{r, z \,|r = R\}$ consists of three different domains. The inlet $\partial_w = \{r, z \,|r = R \wedge 0 \leq z < z_1\}$, the membrane $\partial_m = \{r, z \,|r = R \wedge z_1 \leq z \leq z_2\}$, and the outlet $\partial_w = \{r, z \,|r = R \wedge z_2 < z \leq L\}$. At all boundaries $v_z = 0$. At the inlet and the outlet all velocity components are zero. Furthermore, the normal derivative of the concentration is equal to zero, i.e., for $\{r, z \,|r = R \wedge 0 \leq z < z_1\}$ and $\{r, z \,|r = R \wedge z_2 < z \leq L\}$

$$\boldsymbol{v} = 0 \tag{5.89a}$$

$$\boldsymbol{n} \cdot \nabla c = 0\,. \tag{5.89b}$$

At the membrane the radial velocity component, $v_r$, is given by the solvent flux and the concentration flux is given by the solute flux. Thus,

$$\begin{aligned}
&\boldsymbol{v}(r, z, t) \cdot \boldsymbol{n} = \\
&A\left[p(R, z, t) - p_{perm} - (p_{bs} + p_{tmp} - p_{perm})\Phi(t) - \pi(c(R, z, t))\right] &\text{(5.90a)}\\
&\left(\boldsymbol{v}(r, z, t)c(r, z, t) - D\nabla c(r, z, t)\right) \cdot \boldsymbol{n} = Bc(R, z, t)\,, &\text{(5.90b)}
\end{aligned}$$

where $\boldsymbol{n}$ is the outward unit normal vector and $\Phi(t)$ is a smooth hat function defined as

$$\Phi(t) = \begin{cases} 0 & \text{for} \quad t \leq \epsilon/2 \\ 1 & \text{for} \quad 3\epsilon/2 \leq t \leq T_{bs} - \epsilon/2 \\ 0 & \text{for} \quad t \leq t_{bs} + \epsilon/2 \end{cases} \tag{5.91}$$

where $\epsilon$ is small compared to $t_{bs}$. In the interval $t \in (\epsilon/2; 3\epsilon/2)$ there is a smooth transition from one to zero. Similarly, there is a smooth transition from zero to one in the interval $t \in (t_{bs} - \epsilon/2; t_{bs} + \epsilon/2)$ To avoid discontinuities at $z = z_1$ and $z = z_2$, however, a continuous hat function, $\Psi(z) : z \mapsto [0; 1]$, is introduced. This function has a smooth transition from zero to one around $z_1$ and a smooth

transition from 1 to zero around $z_2$. The transition takes place over a length equal to the radius of the hollow fibre, $R$. Hence,

$$\Psi(z) = \begin{cases} 0 & \text{for} \quad 0 \leq z \leq z_1 - R/2 \\ 1 & \text{for} \quad z_1 + R/2 \leq z \leq z_2 - R/2 \\ 0 & \text{for} \quad z_2 + R/2 \leq z \leq L \end{cases} . \tag{5.92}$$

In the interval $z \in (z_1 - R/2; z_1 + R/2)$ there is a smooth transition from zero to one. Similarly, there is a smooth transition from one to zero in the interval $z \in (z_2 - R/2; z_2 + R/2)$.

With this function the boundary conditions, equation (5.89) and equation (5.90), for $\{r, z \,|r = R \wedge 0 \leq z \leq L\}$ can be written as

$$\boldsymbol{v}(R,z,t) \cdot \boldsymbol{t} = 0 \tag{5.93a}$$

$$\boldsymbol{v}(R,z,t) \cdot \boldsymbol{n} = A\left(p(R,z,t) - p_{perm} - (p_{bs} + p_{tmp} - p_{perm})\Phi(t) - \pi(c(R,z,t))\right)\Psi(z) \tag{5.93b}$$

$$\left(\boldsymbol{v}(R,z,t)c(R,z,t) - D\nabla c(R,z,t)\right) \cdot \boldsymbol{n} = Bc(R,z,t)\Psi(z)\,, \tag{5.93c}$$

where $\boldsymbol{n}$ is the outward unit normal vector, and $\boldsymbol{t}$ the unit vector tangential to the surface. Taking into account, the high length to radius ratio of the hollow fibre tube, the introduction of the smoothing function $\Psi$, should not influence the results significantly. The same argument holds for the function $\Phi(t)$ when $\epsilon$ is small compared to the back-shock time.

### 5.7.3 Transmembrane pressure

In order to relate the results to a given transmembrane pressure the boundary condition at the outlet $p_{out}$ is calculated assuming that there is a fully developed Poiseuille flow, with the viscosity of the solvent, within the hollow fibre. For a fully developed Poiseuille flow the average velocity can be expressed as

$$u_{in,av} = \frac{R^2}{8\eta_s}\frac{p_{in} - p_{out}}{L}\,. \tag{5.94}$$

Hence,

$$p_{in} - p_{out} = \frac{8\eta_s L u_{in,av}}{R^2}\,. \tag{5.95}$$

Furthermore, from the definition of the transmembrane pressure, we have

$$p_{tmp} = \frac{p_{in} + p_{out}}{2} - p_{perm}\,. \tag{5.96}$$

Combining equation (5.95) and equation (5.96) an expression for the pressure at the outlet can be found

$$p_{out} = p_{tmp} + p_{perm} - \frac{4\eta_s L u_{in,av}}{R^2}\,. \tag{5.97}$$

This pressure is used as the boundary condition at the outlet, see equation (5.87).

### 5.7.4 Observed rejection

The observed rejection is given by the expression

$$R_{obs} = \left(1 - \frac{\bar{c}_p}{c_{in}}\right) 100\%\,. \tag{5.98}$$

where $\bar{c}_p$ is the average concentration on the permeate after separation.The average concentration on the permeate side is given by the ratio between the total solute flux, and the total solvent flux through the membrane. That is,

$$\bar{c}_p = \frac{\int_0^{t_{bs}+t_{bbs}} \int_0^L \int_0^{2\pi} J_s(z,t) d\theta dz dt}{\int_0^{t_{bs}+t_{bbs}} \int_0^L \int_0^{2\pi} J_v(z,t) d\theta dz dt} = \frac{\int_0^{t_{bs}+t_{bbs}} \int_0^L \int_0^{2\pi} Bc(R,z,t) d\theta dz dt}{\int_0^{t_{bs}+t_{bbs}} \int_0^L \int_0^{2\pi} v_r(R,z,t) d\theta dz dt}\,. \tag{5.99}$$

### 5.7.5 Non dimensional groups, variables and equations of motion

Introducing the scaled variables

$$\hat{\boldsymbol{x}} = \frac{\boldsymbol{x}}{R}\,, \quad \hat{\boldsymbol{v}} = \frac{\boldsymbol{v}}{u_{in,av}}\,, \quad \hat{p} = \frac{p - p_{perm}}{u_{in,av}\rho}\,, \quad \hat{c} = \frac{c}{c_{in}}\,. \tag{5.100}$$

The continuity equation of the solvent can be written as

$$\nabla \cdot \hat{\boldsymbol{v}} = 0\,. \tag{5.101}$$

The continuity equation of the solvent can be written as

$$\hat{\boldsymbol{v}} \cdot \nabla \hat{c} = \frac{1}{Pe} \nabla^2 \hat{c}\,, \tag{5.102}$$

where the Péclet number is given by

$$Pe = \frac{u_{in,av} R}{D}\,. \tag{5.103}$$

The momentum equation can be written as

$$\hat{\boldsymbol{v}} \cdot \nabla \boldsymbol{v} = \nabla \cdot \hat{\mathbf{\Pi}}\,, \tag{5.104}$$

where, the non-dimensional total stress tensor is given by

$$\hat{\mathbf{\Pi}} = \hat{p}\boldsymbol{I} + \frac{1}{Re}\hat{\eta}(\hat{c})\left[\nabla\hat{\boldsymbol{v}} + (\nabla\hat{\boldsymbol{v}})^T\right]\,. \tag{5.105}$$

Here the Reynolds number is defined by

$$Re = \frac{u_{in,av} R\rho}{\eta_s}\,, \tag{5.106}$$

where $\eta_s$ is the viscosity of the solvent. Furthermore, $\hat{\eta}(\hat{c})$ is given by

$$\hat{\eta}(\hat{c}) = 1 + \alpha_v\left(K' M_w^a c_{in}\hat{c} + k'\left(K' M_w^a\right)^2 c_{in}^2 \hat{c}^2\right) \tag{5.107}$$

### 5.7.6 Mesh

The mesh used in the 3D-model is a mapped mesh. The dimensionless length between the nodes in the axial direction is $\hat{z}_m = 0.02$. In the radial direction there are 40 elements that decrease exponentially in size towards the membrane with an element ratio of 0.0006. The mesh used in shown in figure 5.26 for a total length of 3 times the radius. When simulating the hollow fibre with $L_{in} = L_{out} = 3.5$cm and $L_m = 14$cm the mesh consists of 600000 domain elements and 30160 boundary elements. The system has 2460164 degrees of freedom.

As compared to the two dimensional model no analysis of mesh dependence on the solution has been made. The number of degrees of freedom is so large that the simulation time with this mesh is approximately three days, running in parallel on 8 nodes on the hpc-cluster. Therefore, it was simply not possible to do any comparison between different meshes. By trial and error this is the coarsest mesh that does not show oscillations in the concentration. Such oscillations occur when the mesh is not fine enough where large gradients exist. Furthermore, the solutions have been tested for physical properties such as volume conservation.

### 5.7.7 Simulations

Due to the large computational effort of solving the equations of motion for both the solvent and the solute it is important to confine ourselves to a minor part of

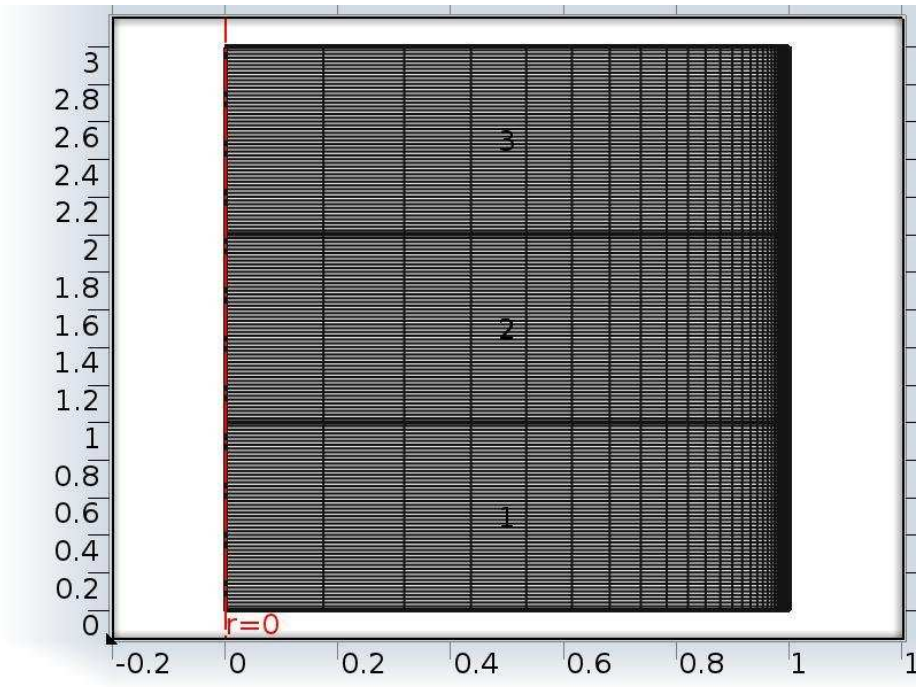


Figure 5.26: The mesh used in the simulations of the 3D-model.

| | $t_{bs}$ |
|---|---|
| Re = 600 | 0.38 s |
| Re = 900 | 0.31 s |

Table 5.3: Upper estimates for the backshock time.

the parameter space. To do this we use the results from the 2D-model. Here we found that the positive effect on the volumetric flux was highest for high transmembrane pressures, high back-shock pressures, and high inlet velocities. Moreover, the effect on a concentration dependent viscosity will be highest for high transmembrane pressures as the concentration polarization is highest in this limit.

Therefore, we choose $p_{tmp} = 2$bar and $p_{bs} = 3$bar, and inlet velocities corresponding to Reynolds numbers of 600 and 900.

As in the 2D-model we investigate the effect of changing the back-shock time. We will use the estimate for the back-shock time given in equation (5.64) with the changed length of the membrane and the parameter values given above. This gives the upper estimates for the optimal back-shock time given in table 5.3.

Since this is a upper estimate we start the simulations with $t_{bs} = 0.37$s for Re = 600 and $t_{bs} = 0.3$s for Re = 900 and do simulations for decreasing values of the back-shock time. For all the simulations made the viscosity has been allowed to depend on the concentration. Hence, for each different back-shock time there is a simulation with $\alpha_v = 0$ and a simulation with $\alpha_v = 1$. The time after the back-shock period is 5 seconds in all simulations. For Re = 600 the investigated back-shock times are $t_{bs} = (0.25, 0.3, 0.37)$s and for Re = 900 the back-shock times are $t_{bs} = (0.2, 0.25, 0.3)$. Moreover, it has been necessary to compute two additional simulations. These are with $\alpha_v = 1$ and $t_{bs} = 0.4$ for Re = 600 and $t_{bs} = 0.33$ for Re = 900 in order to illustrate that the maximum was found when the viscosity depends on the concentration.

## 5.8 Results

In order to relate the 3D-model to the 2D-model a set of simulations have been made with the 2D-model where the length of the membrane is set at 14 cm. It is of course only possible to relate the 2D-model to the 3D-model when the viscosity is concentration independent. In figure 5.27 the average flux is plotted using the same back-shock time. To compare the simulations the results have

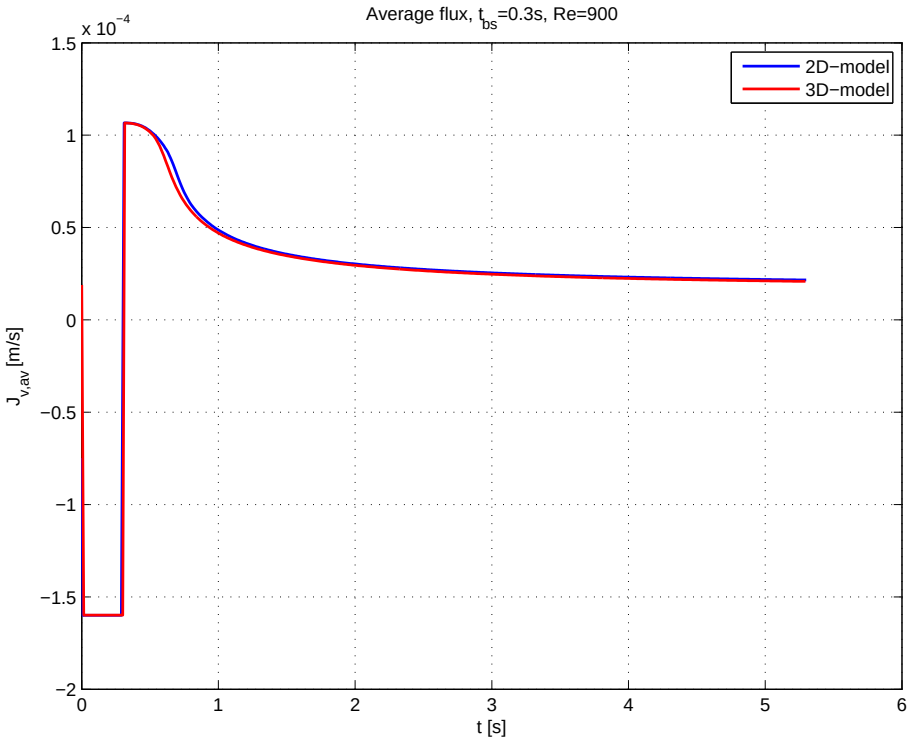


Figure 5.27: Comparison between the solution of the 2D-model and the 3D-model, $t_{bs} = 0.3$s and $\mathrm{Re} = 900$.

been rescaled into real dimensions. For the 2D-model only the last period is plotted and the time has been scaled such that both graphs start at 0. As seen there is a good agreement between the two models.

In figure 5.28 the normalized average flux is shown for the 2D-model and the 3D-model

There is a reasonable agreement between the two models. It does, however, look as if the normalized average flux is shifted slightly towards higher back-shock times for the 2D-model. Moreover, it is seen that the optimal back-shock time estimate is good approximation to the optimal time back-shock time seen in the simulations. Hence, there is no reason to believe that the tendencies presented regarding the 2D-model should not hold for the 3D-model in case the viscosity is concentration independent. Therefore, the next part of the results will concern the effect of the viscosity being concentration dependent.

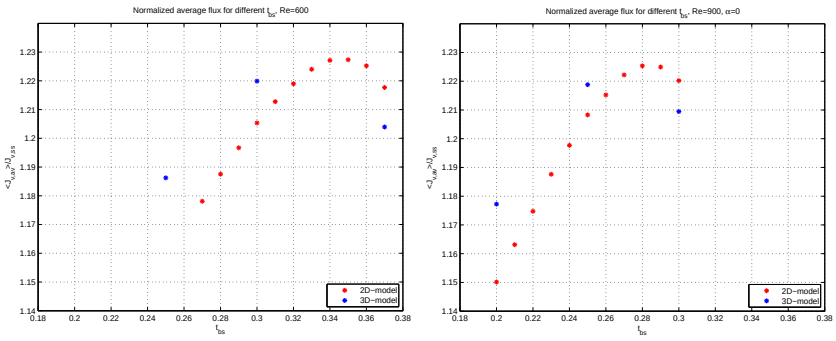


(a) Normalized flux as a function of back-shock time, Re = 600.

(b) Normalized flux as a function of back-shock time, Re = 900.

Figure 5.28: Normalized flux as a function of back-shock time for the 2D-model and the 3D-model and for Re = 600 and Re = 900.

In figure 5.29 the non-dimensional solvent flux through the membrane is shown with and without a concentration dependent viscosity.

As seen the the curves follow each other during the back-shock and initially after the pressure is reversed. When the concentration builds up on the membrane the concentration dependent viscosity makes the flux decrease more rapidly, due to the decrease in axial velocity in the boundary layer. Hence, the average flux when the viscosity is concentration dependent is lower. This is seen in all simulations but the effect is larger for small back-shock times as illustrated as the difference between figure 5.29a and figure 5.29b

The steady-state flux, however, is also lower when the viscosity depends on the concentration. Therefore, the normalized average flux is higher when the viscosity depends on the concentration. This is seen in figure 5.30a and 5.30b. As compared to the steady-state solution an increase of 22% is seen for Re = 600 and a concentration independent viscosity. The increase in solvent flux for the same value of the inlet velocity and a concentration dependent viscosity is 36%. For Re = 900 there is an increase in solvent flux compared the steady-state solution of 22% when the viscosity is constant. Whereas there is an increase of 42.5 % when the viscosity depends on the concentration.

Moreover, it is seen that the back-shock time that gives the maximum solvent flux when the viscosity does not depend on the concentration is lower than the estimated time as expected. When the viscosity depends on the concentration this time increases. This can be understood since, a higher viscosity decreases the axial velocity when the concentration is higher than the bulk concentration.

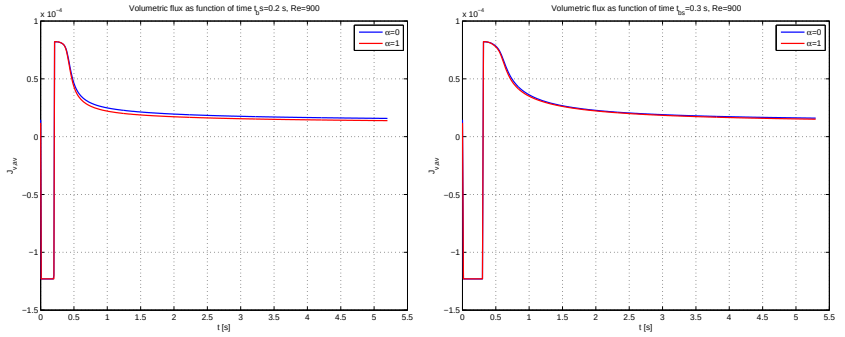


(a) Dimensionless flux as a function of time with Re = 900 and $t_{bs} = 0.2s$.

(b) Dimensionless flux as a function of time with Re = 900 and $t_{bs} = 0.3s$.

Figure 5.29: Dimensionless flux as a function of time, Re = 900.

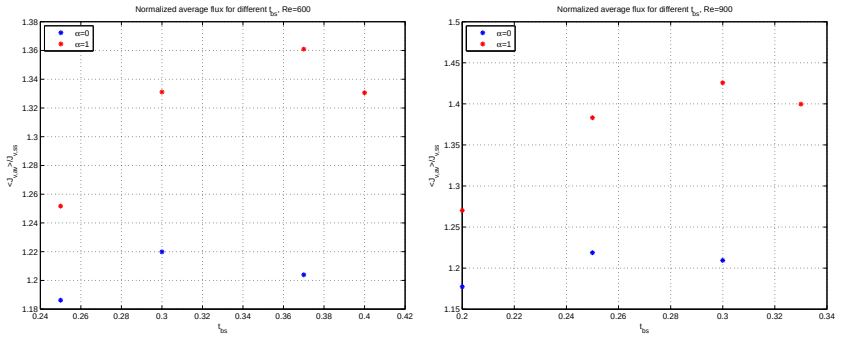


(a) Normalized flux as a function of back-shock time, Re = 600.

(b) Normalized flux as a function of back-shock time, Re = 900.

Figure 5.30: Normalized flux as a function of back-shock time.

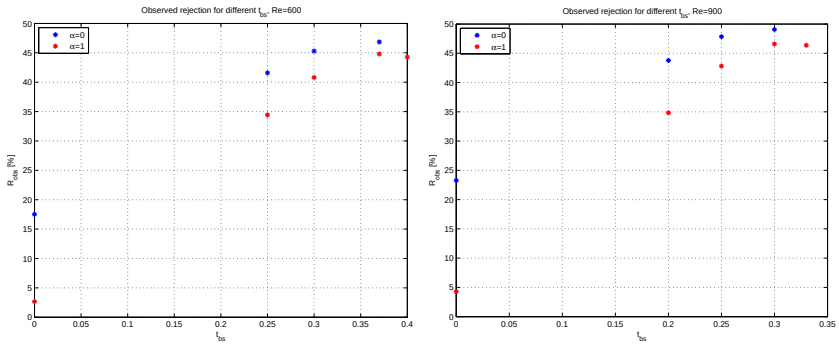


(a) Observed rejection as a function of back-shock time, Re = 600.

(b) Observed rejection as a function of back-shock time, Re = 900.

Figure 5.31: Observed rejection a function of back-shock time.

Therefore, a higher back-shock time would be expected in order to move the highly concentrated area down the length of the membrane.

In figure 5.31 the observed rejection is shown as a function of back-shock pressure. As seen in figure 5.31 the there is a significant increase in the observed rejection when back-shocking is applied as compared to the steady-state solution. This increase is more pronounced when the viscosity depends on the concentration. There is an increase in observed rejection of approximately 40 % when the viscosity depends on the concentration, whereas the increase is approximately 25 % when the viscosity does not depend on the concentration. Moreover, the highest values of the observed rejection are found for the highest inlet velocities.

## 5.9 Conclusions on the 3D-model

Because of the long computational times needed to solve the 3D-model it was important to know where in the parameter space a positive effect should be found. This and the fact that it was not possible to simulate the full hollow fibre made the back-shock estimate presented in the 2D-model the point of reference in the simulations.

Using this approach it was possible to find the optimal back-shock time given the parameters of the problem. The optimal back-shock time is higher when the viscosity depends on the concentration, as compared to a constant viscosity. This can be explained by a decrease in axial velocity due to an increase in viscosity.

A substantial increase in observed rejection was found when applying back-shock as compared to the steady-state solution. This increase is highest when the viscosity depends on the concentration.

## 5.10 Relating the results to the literature

Relating the model to the literature has been somewhat difficult. There are plenty of examples on the effect of back-shocking in the literature. Many are for microfiltration where the models presented to explain the flux all build upon the formation of a cake layer. Since this model does not consider cake formation a relation to these results seems irrelevant.

Different papers consider back-shocking in ultrafiltration [30, 20, 54, 33, 52, 59, 7]. Relations between the model and the results presented in these papers are given below.

In [30] dextran with a molecular weight of 10000 kDa was fractionized from hemoglobin in a hollow fibre module. Here an increase in flux was reported and a decrease in rejection coefficient of dextran was observed. This is, however, not contrary to what is reported here since hemoglobin was acting as a secondary membrane, and the molecular weight cutoff of the membrane used was 30000 kDa. Hence, the membrane would have little or no rejection to a solution containing only dextran molecules. Therefore, the rejection for hemoglobin would have been of more interest when comparing to this model. Unfortunately, these data are not reported.

In [20] bovine serum albumin filtered in cross-flow. An increase in flux is observed when using back-shocking as compared to not using back-shocking. The effect was seen to increase as a function of transmembrane pressure. In this model an increasing effect of increasing transmembrane pressure is observed. The back-shock time and time between back-shocking was 2 min. Remaining parameters such as the membrane dimensions and the cross-flow velocity is not reported, which makes it hard to relate. It should, however, be said that obtaining a positive effect using back-shock times of 2 min seems to be highly unlikely in this model.

In [54] wastewater treatment was investigated. An increase of 17 % on the flux through the membrane was observed when applying back-shocking as compared to not applying back-shocking. An increase of this magnitude is within what is observed in this model. Furthermore, a back-shock time of 0.5 s every min is comparable to the results in this model. Moreover, they used a tubular membrane

with an inner diameter of 7 mm and a lenght of 25 cm which is comparable to the hollow fibre modelled here. Moreover, a transmembrane pressure of 1.8 bar was used, which is within the range of what has been investigated here. They do, however, operate the system under turbulent conditions which decreases the degree of comparison between the experimental results and this model. Furthermore, a decrease in retention was observed when applying back-shocking. As explained that is not possible in this model. The decrease in retention could, however, be explained by the amount of different solutes (six main wastewater components) which could behave as secondary membranes.

In [33] transmembrane pressure of 1 bar and a back-shock pressure of 4 bar, a back-shock time of 1s every 2 min gave the largest increase in permeate flux. There is, however, no reference steady-state flux given, nor is the membrane length given. Moreover, a Reynolds numbers in the range 27000-38500 was used.

In [52] pressure pulsing was used to enhance the flux. A very good description of the experimental method allows to calculate the back-shock estimate. The estimate calculated is of the order 10s. The pulse duration used is, however, of the order $10^{-1}$s. Furthermore, a pulse frequency in the interval 0.5-5 Hz is used. Surely, the order of magnitude of both the frequency and the pulse duration does not reflect that the boundary layer concentration is transported down the length of the membrane, nor is the concentration polarization close to the steady-state when back-shocking is applied. Rather the concentration build up is disturbed and maintains a value low enough such that a positive gain is seen. A very interesting observation and one that this model would be capable of investigating. This has, however, not been done.

In [59] a tubular membrane with inner diameter of 7 mm and a length of 250 mm was operated at a transmembrane pressure and a back-shock pressure of 3 bar, and an inlet velocity of 0.94 m/s, assuming that the pure water permeability is similar to the one given in the model, the back-shock times should be similar to the ones given by the model. The optimal back-shock operating conditions was found to be 1 min of forward filtration, which should be long enough that the concentration profile is close to fully developed, and a back-shock time of 0.7 s. These times are comparable to the back-shock times predicted by the model.

In [7] apple juice clarification was investigated. Here, the filtration was made in two different tubular membranes with inner diameter of 3 mm and 2.8 mm. All the variables needed to calculate the back-shock time estimate as approximately 1.8 s for both membranes. The time between back-shocks was 2 to 5 min, which must be considered long enough to be relatively close to a fully developed concentration polarization. Back-shock time for both membranes was 2-5 s. A positive effect on the permeate flux was obtained for the first membrane, whereas no effect was observed for the second membrane. the observed effect was 50 %

higher with back-shocking as compared to no back-shocking This is in reasonable agreement with the model.

For the reasons given above no experimental results found in the literature can verify, nor can they falsify the model. Therefore, experimental results would be highly appreciable.

## 5.11 Conclusions

Two models concerning back-shocking in a hollow fibre were presented. Both models assumed that the decrease in flux due to concentration polarization was caused only by the osmotic pressure. In both models a positive effect as compared to the steady-state solution was obtained.

In the two dimensional model an estimate for the back-shock time was deduced from the hypothesis that the path-lines gave an upper limit for the back-shock time.

This upper limit was used in the three dimensional model to predict the back-shock time. A good agreement between the estimate and the optimal back-shock time was found.

As a consequence of the model an increase in solvent flux would automatically lead to an increase in observed rejection. It was, however, also found that the observed rejection could increase even with solvent fluxes lower than the steady-state solvent flux.

In the three dimensional model, simulations were done with a constant viscosity and a concentration dependent viscosity. The solvent flux was highest when the viscosity was constant. The ratio between the average flux and the steady-state flux was, however, substantially higher when the viscosity depended on the concentration.

It has been hard to find literature which can either confirm the validity of the model, or falsify the approach.

Appendix A

# The equations of motion in non-dimensional form

## A.1 Incompressibility

The equation for incompressibility of a fluid is given by

$$\nabla \cdot \boldsymbol{v} = 0\,. \tag{A.1}$$

Introducing the scaled variables

$$x_i' = \frac{x_i}{L} \quad v_i' = \frac{v_i}{U}\,, \tag{A.2}$$

and inserting these into equation (A.1) gives

$$\frac{U}{L}\nabla' \cdot \boldsymbol{v}' = 0 \Leftrightarrow \nabla' \cdot \boldsymbol{v}' = 0\,. \tag{A.3}$$

### A.1.1 The incompressible Navier-Stokes equation

The Navier-Stokes equation for an incompressible fluid is given by

$$\rho\frac{\partial \boldsymbol{v}}{\partial t} + \rho\boldsymbol{v} \cdot \nabla\boldsymbol{v} = -\nabla p + \eta\nabla^2\boldsymbol{v}\,. \tag{A.4}$$

In order to give the equation in non-dimensional form, we introduce the non-dimensional scaled variables

$$t' = \frac{t}{\bar{t}} \quad x_i' = \frac{x_i}{L} \quad v_i' = \frac{v_i}{U} \quad p' = \frac{p - p_0}{\bar{p}}\,. \tag{A.5}$$

Inserting these variables into equation (A.4) gives

$$\rho \frac{U}{\bar{T}} \frac{\partial \boldsymbol{v}'}{\partial t'} + \rho \frac{U^2}{L} \boldsymbol{v} \cdot' \nabla' \boldsymbol{v}' = -\frac{\bar{p}}{L} \nabla' p' + \eta \frac{U}{L^2} \nabla'^2 \boldsymbol{v}'\,. \tag{A.6}$$

Choosing $\bar{T} = {}^{L}/_{U}$, and dividing through with ${}^{\rho U^2}/_{L}$ in equation (A.6) gives

$$\frac{\partial \boldsymbol{v}'}{\partial t'} + \boldsymbol{v}' \cdot \nabla' \boldsymbol{v}' = -\frac{\bar{p}}{\rho U^2} \nabla' p' + \frac{\eta}{\rho L U} \nabla'^2 \boldsymbol{v}'\,. \tag{A.7}$$

Thus, choosing $\bar{p} = \rho U^2$ gives

$$\frac{\partial \boldsymbol{v}'}{\partial t'} + \boldsymbol{v}' \cdot \nabla' \boldsymbol{v}' = -\nabla' p' + \frac{\eta}{\rho L U} \nabla'^2 \boldsymbol{v}'\,. \tag{A.8}$$

The Reynolds number is defined as $Re = {}^{\rho L U}/_{\eta}$. Hence, equation (A.8) can be written as

$$\frac{\partial \boldsymbol{v}'}{\partial t'} + \boldsymbol{v}' \cdot \nabla' \boldsymbol{v}' = -\nabla' p' + \frac{1}{Re} \nabla'^2 \boldsymbol{v}'\,. \tag{A.9}$$

### A.1.2 The continuity equation

The continuity equation where the diffusion coefficient is assumed independent of the concentration is given by

$$\frac{\partial c}{\partial t} + \boldsymbol{v} \cdot \nabla c = D \nabla^2 c\,. \tag{A.10}$$

Again, choosing the scaled variables as

$$t' = \frac{t}{{}^{L}/_{U}} \quad x_i' = \frac{x_i}{L} \quad v_i' = \frac{v_i}{U} \quad c' = \frac{c}{c_0}\,, \tag{A.11}$$

and inserting into equation (A.10) we have

$$\frac{c_0 U}{L} \frac{\partial c'}{\partial t'} + \frac{c_0 U}{L} \boldsymbol{v}' \cdot \nabla' c' = \frac{D c_0}{L^2} \nabla'^2 c'\,. \tag{A.12}$$

Dividing through with $\frac{c_0 U}{L}$, in equation (A.12), gives

$$\frac{\partial c'}{\partial t'} + \boldsymbol{v}' \cdot \nabla' c' = \frac{D}{UL} \nabla'^2 c'\,. \tag{A.13}$$

The Péclet number is defined as $Pe = {}^{UL}/_{D}$. Hence, equation (A.13) can be written as

$$\frac{\partial c'}{\partial t'} + \boldsymbol{v}' \cdot \nabla' c' = \frac{1}{Pe} \nabla'^2 c' \,. \tag{A.14}$$

Thus, the equations of motion in non-dimensional form is given by the equation (A.3), equation (A.9), and equation (A.14).

## A.2 Using multiple scales

In this section the incompressible, steady state, and viscous, Navier-Stokes equation and the continuity equation, will be scaled using different length scales, in cylindrical coordinates.

In cylindrical coordinates the incompressible, viscous, Navier-Stokes equation is given by

$$v_z \frac{\partial v_z}{\partial z} + v_r \frac{\partial v_z}{\partial r} + \frac{v_\phi}{r} \frac{\partial v_z}{\partial \phi} = \frac{-1}{\rho} \frac{\partial p}{\partial z} + \nu \nabla^2 v_z \tag{A.15a}$$

$$v_z \frac{\partial v_r}{\partial z} + v_r \frac{\partial v_r}{\partial r} + \frac{v_\phi}{r} \frac{\partial v_r}{\partial \phi} = \frac{-1}{\rho} \frac{\partial p}{\partial r} + \nu \left( \nabla^2 v_r - \frac{v_r}{r^2} - \frac{2}{r^2} \frac{\partial v_\phi}{\partial \phi} \right) \tag{A.15b}$$

$$v_z \frac{\partial v_\phi}{\partial z} + v_r \frac{\partial v_\phi}{\partial r} + \frac{v_\phi}{r} \frac{\partial v_\phi}{\partial \phi} + \frac{v_r v_\phi}{r} = \frac{-1}{\rho r} \frac{\partial p}{\partial \phi} + \nu \left( \nabla^2 v_\phi + \frac{2}{r^2} \frac{\partial v_r}{\partial \phi} - \frac{v_\phi}{r^2} \right) . \tag{A.15c}$$

The incompressibility is given by

$$\nabla \cdot \boldsymbol{v} = \frac{\partial v_z}{\partial z} + \frac{v_r}{\partial r} + \frac{v_r}{r} + \frac{1}{r} \frac{\partial v_\phi}{\partial \phi} = 0 \,. \tag{A.16}$$

The Laplace operator is given by

$$\nabla^2 = \frac{\partial^2}{\partial z} + \frac{1}{r} \frac{\partial}{\partial r} + \frac{\partial^2}{\partial r^2} + \frac{1}{r^2} \frac{\partial^2}{\partial \phi^2} \,. \tag{A.17}$$

The continuity equation is given by

$$v_z \frac{\partial c}{\partial z} + v_r \frac{\partial c}{\partial r} + \frac{v_\phi}{r} \frac{\partial c}{\partial \phi} = \nabla \cdot \left[ \begin{pmatrix} D & 0 & 0 \\ 0 & D & 0 \\ 0 & 0 & D \end{pmatrix} \begin{pmatrix} \frac{\partial c}{\partial z} \\ \frac{\partial c}{\partial r} \\ \frac{1}{r} \frac{\partial c}{\partial \phi} \end{pmatrix} \right] . \tag{A.18}$$

For tubular separation $v_\phi$ and $\frac{\partial}{\partial\phi}$ vanishes. Hence, equation (A.15c) vanishes and equation (A.15a) and equation (A.15b) reduces to

$$v_z\frac{\partial v_z}{\partial z}+v_r\frac{\partial v_z}{\partial r}=\frac{-1}{\rho}\frac{\partial p}{\partial z}+\nu\nabla^2 v_z \tag{A.19a}$$

$$v_z\frac{\partial v_r}{\partial z}+v_r\frac{\partial v_r}{\partial r}=\frac{-1}{\rho}\frac{\partial p}{\partial r}+\nu\left(\nabla^2 v_r-\frac{v_r}{r^2}\right). \tag{A.19b}$$

Equation (A.16) reduces to

$$\nabla\cdot\boldsymbol{v}=\frac{\partial v_z}{\partial z}+\frac{v_r}{\partial r}+\frac{v_r}{r}=0\,. \tag{A.20}$$

The Laplace operator reduces to

$$\nabla^2=\frac{\partial^2}{\partial z}+\frac{1}{r}\frac{\partial}{\partial r}+\frac{\partial^2}{\partial r^2}\,. \tag{A.21}$$

And the continuity equation reduces to

$$v_z\frac{\partial c}{\partial z}+v_r\frac{\partial c}{\partial r}=\nabla\cdot\left[\begin{pmatrix} D & 0\\ 0 & D\end{pmatrix}\begin{pmatrix}\frac{\partial c}{\partial z}\\ \frac{\partial c}{\partial r}\end{pmatrix}\right]. \tag{A.22}$$

## A.3 Scaling the equations of motion with two different lengths

In this section the equation of motion will be scaled using two different lengths in the axial and radial direction. Hence, we introduce the non-dimensional variables presented in equation (A.23)

$$\hat r=\frac{r}{R}\,,\quad \hat z=\frac{z}{L}\,,\quad \hat v_r=\frac{v_r}{U}\,,\quad \hat v_z=\frac{v_z}{U}\quad \hat p=\frac{p}{P}\,,\quad \hat c=\frac{c}{C}\,. \tag{A.23}$$

Inserting these vaariables into equation (A.19a) and equation (A.19b) one obtains

$$\frac{U^2}{L}\hat v_z\frac{\partial\hat v_z}{\partial\hat z}+\frac{U^2}{R}\hat v_r\frac{\partial\hat v_z}{\partial\hat r}=\frac{-P}{\rho L}\frac{\partial\hat p}{\partial\hat z}+\nu\left(\frac{U}{R^2}\frac{1}{\hat r}\frac{\partial}{\partial\hat r}\left(\hat r\frac{\partial\hat v_z}{\partial\hat r}\right)+\frac{U}{L^2}\frac{\partial^2\hat v_z}{\partial\hat z^2}\right) \tag{A.24a}$$

$$\frac{U^2}{L}\hat v_z\frac{\partial\hat v_r}{\partial\hat z}+\frac{U^2}{R}\hat v_r\frac{\partial\hat v_r}{\partial\hat r}=\frac{-P}{\rho R}\frac{\partial\hat p}{\partial\hat r}+\nu\left(\frac{U}{R^2}\frac{1}{\hat r}\frac{\partial}{\partial\hat r}\left(\hat r\frac{\partial\hat v_r}{\partial\hat r}\right)+\frac{U}{L^2}\frac{\partial^2\hat v_r}{\partial\hat z^2}-\frac{U}{R^2}\frac{\hat v_r}{\hat r^2}\right). \tag{A.24b}$$

Dividing through be $^{U^2}/_R$ on obtains

$$\frac{R}{L}\hat{v}_z\frac{\partial\hat{v}_z}{\partial\hat{z}}+\hat{v}_r\frac{\partial\hat{v}_z}{\partial\hat{r}}=\frac{-P}{\rho U^2}\frac{R}{L}\frac{\partial\hat{p}}{\partial\hat{z}}+\frac{\nu}{UR}\left(\frac{1}{\hat{r}}\frac{\partial}{\partial\hat{r}}\left(\hat{r}\frac{\partial\hat{v}_z}{\partial\hat{r}}\right)+\frac{R^2}{L^2}\frac{\partial^2\hat{v}_z}{\partial\hat{z}^2}\right) \tag{A.25a}$$

$$\frac{R}{L}\hat{v}_z\frac{\partial\hat{v}_r}{\partial\hat{z}}+\hat{v}_r\frac{\partial\hat{v}_r}{\partial\hat{r}}=\frac{-P}{\rho U^2}\frac{\partial\hat{p}}{\partial\hat{r}}+\frac{\nu}{UR}\left(\frac{1}{\hat{r}}\frac{\partial}{\partial\hat{r}}\left(\hat{r}\frac{\partial\hat{v}_r}{\partial\hat{r}}\right)+\frac{R^2}{L^2}\frac{\partial^2\hat{v}_r}{\partial\hat{z}^2}-\frac{\hat{v}_r}{\hat{r}^2}\right). \tag{A.25b}$$

Defining the non-dimensional groups and $P$ as

$$\lambda=\frac{R}{L}\,,\quad Re=\frac{UR}{\nu}\,,\quad P=\rho U^2\,. \tag{A.26}$$

And inserting these into equation (A.25a) and equation (A.25b) one gets

$$\lambda\hat{v}_z\frac{\partial\hat{v}_z}{\partial\hat{z}}+\hat{v}_r\frac{\partial\hat{v}_z}{\partial\hat{r}}=-\lambda\frac{\partial\hat{p}}{\partial\hat{z}}+\frac{1}{Re}\left(\frac{1}{\hat{r}}\frac{\partial}{\partial\hat{r}}\left(\hat{r}\frac{\partial\hat{v}_z}{\partial\hat{r}}\right)+\lambda^2\frac{\partial^2\hat{v}_z}{\partial\hat{z}^2}\right) \tag{A.27a}$$

$$\lambda\hat{v}_z\frac{\partial\hat{v}_r}{\partial\hat{z}}+\hat{v}_r\frac{\partial\hat{v}_r}{\partial\hat{r}}=-\frac{\partial\hat{p}}{\partial\hat{r}}+\frac{1}{Re}\left(\frac{1}{\hat{r}}\frac{\partial}{\partial\hat{r}}\left(\hat{r}\frac{\partial\hat{v}_r}{\partial\hat{r}}\right)+\lambda^2\frac{\partial^2\hat{v}_r}{\partial\hat{z}^2}-\frac{\hat{v}_r}{\hat{r}^2}\right). \tag{A.27b}$$

Similarly equation (A.20) becomes

$$\lambda\frac{\partial\hat{v}_z}{\partial\hat{z}}+\frac{\hat{v}_r}{\partial\hat{r}}+\frac{\hat{v}_r}{\hat{r}}=0\,. \tag{A.28}$$

Equation (A.22) in the scaled variables becomes

$$\lambda\hat{v}_z\frac{\partial\hat{c}}{\partial\hat{z}}+\hat{v}_r\frac{\partial\hat{c}}{\partial\hat{r}}=\frac{D}{UR}\left[\frac{1}{\hat{r}}\frac{\partial\hat{c}}{\partial\hat{r}}+\frac{\partial^2\hat{c}}{\partial\hat{r}^2}\right]+\frac{DR}{UL^2}\frac{\partial\hat{c}}{\partial\hat{z}}\,. \tag{A.29}$$

Defining the Péclet number as $Pe=^{UR}/_D$, equation (A.29) can be written as

$$\lambda\hat{v}_z\frac{\partial\hat{c}}{\partial\hat{z}}+\hat{v}_r\frac{\partial\hat{c}}{\partial\hat{r}}=\frac{1}{Pe}\left[\frac{1}{\hat{r}}\frac{\partial\hat{c}}{\partial\hat{r}}+\frac{\partial^2\hat{c}}{\partial\hat{r}^2}\right]+\frac{\lambda^2}{Pe}\frac{\partial\hat{c}}{\partial\hat{z}}\,. \tag{A.30}$$

Let the gradient, the divergence, and the Laplace operator in the scaled variables be defined as follows

$$\hat{\nabla}\boldsymbol{u}=\left[\frac{\partial u_r}{\partial\hat{r}},\frac{\partial u_z}{\partial\hat{z}}\right]^T,\quad \hat{\nabla}\cdot\boldsymbol{u}=\frac{1}{\hat{r}}\frac{\partial}{\partial\hat{r}}\left(\hat{r}u_r\right)+\frac{\partial u_z}{\partial\hat{z}}\,,\quad \hat{\nabla}^2\boldsymbol{u}=\frac{1}{\hat{r}}\frac{\partial}{\partial\hat{r}}\left(\hat{r}\frac{\partial u_r}{\partial\hat{r}}\right)+\frac{\partial^2u_z}{\partial\hat{z}^2}\,. \tag{A.31}$$

Appendix B

# The maximal length of a chord in an ellipse

Given two points on an ellipse

$$P = \boldsymbol{\gamma}(s) = (r_2 \sin(s), -r_1 \cos(s))\,, \tag{B.1}$$

and

$$P = \boldsymbol{\gamma}(\hat{s}) = (r_2 \sin(\hat{s}), -r_1 \cos(\hat{s}))\,. \tag{B.2}$$

The vector joining the two points is given by

$$\bar{\gamma}(s, \hat{s}) = \boldsymbol{\gamma}(s) - \boldsymbol{\gamma}(\hat{s})\,. \tag{B.3}$$

The length of this vector is the length of the chord between the two points and is given by

$$\|\bar{\boldsymbol{\gamma}}(s, \hat{s})\| = \sqrt{r_2^2 \left(\sin(s) - \sin(\hat{s})\right)^2 + r_1^2 \left(\cos(s) - \cos(\hat{s})\right)^2}\,. \tag{B.4}$$

Thus for a fixed $s$ the maximal length of the chord is given by solving the equation

$$\frac{d}{d\hat{s}} \|\bar{\boldsymbol{\gamma}}(\hat{s})\| = 0\,. \tag{B.5}$$

As we shall see this equation can have up to three solutions. However, the trivial solution that gives the minimal length, $s = \hat{s}$ is of no interest. Therefore, the

assumption that $s \neq \hat{s}$ will be used in the following. Reducing the number of possible solutions to two.

$$0 = \frac{d}{d\hat{s}} \left\| \bar{\gamma}(\hat{s}) \right\| \Leftrightarrow \tag{B.6a}$$

$$0 = \frac{-r_2^2 \left[\sin(s) - \sin(\hat{s})\right] \cos(\hat{s}) + r_1^2 \left[\cos(s) - \cos(\hat{s})\right] \sin(\hat{s})}{\left\| \bar{\gamma}(\hat{s}) \right\|} \Leftrightarrow \tag{B.6b}$$

$$0 = -\left[\sin(s) - \sin(\hat{s})\right] \cos(\hat{s}) + \left(\frac{r_1}{r_2}\right)^2 \left[\cos(s) - \cos(\hat{s})\right] \sin(\hat{s}) \,. \tag{B.6c}$$

Using the relation

$$\sin(s - \hat{s}) = \sin(s)\cos(\hat{s}) - \cos(s)\sin(\hat{s}) \tag{B.7}$$

in equation (B.6c) one obtains

$$\begin{aligned} &\sin(s - \hat{s}) + \cos(s)\sin(\hat{s}) - \sin(\hat{s})\cos(\hat{s}) \\ &\qquad = \left(\frac{r_1}{r_2}\right)^2 \left[\cos(s) - \cos(\hat{s})\right] \sin(\hat{s}) \Leftrightarrow \end{aligned} \tag{B.8a}$$

$$\sin(s - \hat{s}) = \left(\left(\frac{r_1}{r_2}\right)^2 - 1\right) \left[\cos(s) - \cos(\hat{s})\right] \sin(\hat{s}) \Leftrightarrow \tag{B.8b}$$

$$\sin(\hat{s} - s) = \left(1 - \left(\frac{r_1}{r_2}\right)^2\right) \left[\cos(s) - \cos(\hat{s})\right] \sin(\hat{s}) \Leftrightarrow \tag{B.8c}$$

$$\sin(\hat{s} - s) = k^2 \left[\cos(s) - \cos(\hat{s})\right] \sin(\hat{s}) \tag{B.8d}$$

A few special situations can be mentioned.

If $r_1 = r_2$, meaning that $k^2 = 0$ equation (B.8d) reduces to

$$\sin(\hat{s} - s) = 0 \,. \tag{B.9}$$

When $\hat{s} \neq s$ the solution is $\hat{s} - s = \pi$ as expected.

If $s = 0$ equation (B.8d) reduces to

$$\sin(\hat{s}) = k^2 \left[1 - \cos(\hat{s})\right] \sin(\hat{s}) \,. \tag{B.10}$$

Since $k^2 \leq 0$ this equation has only one solution, namely $\hat{s} = \pi$. This is of course expected as this represents the major axis of the ellipse.

If $s = \pi/2$ equation (B.8d) reduces to

$$\cos(\hat{s}) = k^2 \sin(\hat{s})\cos(\hat{s}) \Leftrightarrow \cos(\hat{s}) \left[1 - k^2 \sin(\hat{s})\right] = 0 \,. \tag{B.11}$$

This special case has one solution for $-1 \leq k^2 \leq 0$ that is $\hat{s} = {}^{3\pi}/_{2}$. For $k^2 < -1$ there are two solutions. Namely the two solutions that fulfil the equation

$$\sin(\hat{s}) = \frac{1}{k^2}\,. \tag{B.12}$$

There will be two solutions to this equation. One in the third quadrant and one in the fourth quadrant. This is expected because of the symmetry in the x-axis.

Appendix C

# Diffusion of a point mass in one dimension with constant velocity

The derivation of diffusion of a point mass can be found in many textbooks on fluid dynamics (see, e.g., [14, 34]). Here, the solution to the one dimensional continuity equation for solute with velocity $u = 0$,

$$\frac{\partial c}{\partial t} = D\frac{\partial^2 c}{\partial x^2}\,, \tag{C.1}$$

is given by

$$c(x,t) = \frac{C_0}{\sqrt{4\pi D t}} \exp\left(-\frac{x^2}{4Dt}\right) \tag{C.2}$$

Assuming that a mass $M$ of solute is placed at origin at time $t = 0$. I.e.,

$$c(0,0) = M\delta(x), \tag{C.3}$$

the constant $C_0$ is determined from the conservation of mass,

$$\int_{-\infty}^{\infty} c(x,t) = M\,. \tag{C.4}$$

Hence, $C_0 = M$.

In the case of a constant velocity, $u$, the continuity equation can be written as

$$\frac{\partial c}{\partial t} + u\frac{\partial c}{\partial x} = D\frac{\partial^2 c}{\partial x^2}\,, \tag{C.5}$$

one can introduce the scaled variable

$$\eta = x - ut\,, \tag{C.6}$$

and change variables from $x, t$ to $\eta, t$ Using the chain rule one has

$$\frac{\partial c}{\partial t} = \frac{\partial c}{\partial t} + \frac{\partial c}{\partial \eta}\frac{\partial \eta}{\partial t} = \frac{\partial c}{\partial t} - u\frac{\partial c}{\partial \eta}\,, \tag{C.7}$$

and

$$\frac{\partial c}{\partial x} = \frac{\partial c}{\partial \eta} \tag{C.8}$$

Hence, equation (C.5) can be written as

$$\frac{\partial c}{\partial t} = D\frac{\partial^2 c}{\partial \eta^2}\,. \tag{C.9}$$

Again, solution is the given by

$$c(\eta, t) = \frac{M}{\sqrt{4\pi D t}}\exp\left(-\frac{\eta^2}{4Dt}\right) \tag{C.10}$$

Substituting the expression for $\eta$

$$c(x, t) = \frac{M}{\sqrt{4\pi D t}}\exp\left(-\frac{(x-ut)^2}{4Dt}\right)\,. \tag{C.11}$$

Scaling the variables reduces equation (C.1) to

$$\frac{\partial \hat{c}}{\partial \hat{t}} + \hat{u}\frac{\partial \hat{c}}{\partial \hat{x}} = \frac{1}{\mathrm{Pe}}\frac{\partial^2 \hat{c}}{\partial \hat{x}^2}\,, \tag{C.12}$$

Obviously $1/\mathrm{Pe}$ enters equation (C.12) in the same way as $D$ does in equation (C.5). Therefore, the solution presented above can be repeated and the solution to equation (C.12) is given by

$$\hat{c}(\hat{x}, \hat{t}) = \frac{\hat{M}}{\sqrt{4\pi\frac{1}{\mathrm{Pe}}\hat{t}}}\exp\left(-\frac{\left(\hat{x}-\hat{u}\hat{t}\right)^2}{4\frac{1}{\mathrm{Pe}}\hat{t}}\right)\,. \tag{C.13}$$

Appendix D

# Integration under path-lines

In this appendix the ratio between the gain and the loss of pure water flux during a back-shock cycle is calculated. The ratio is calculated for a back-shock time given by equation (5.64), corresponding to the path-line from $(0, 0)$ to $(L_m, 0)$. Thereafter, it is possible to argue that this is the supremum of this ratio.

The amount of pure solvent injected into the hollow fibre during back-shocking is well approximated by

$$\phi_l = L_m A p_{bs} t_{bs} \,. \tag{D.1}$$

The regain as pure solvent flux is given by the area under the path-line, i.e.,

$$\phi_g = \int_0^{L_m} y(x) dx \,. \tag{D.2}$$

During back-shocking the $x$ and $y$-coordinate as a function of time is given by

$$y(t) = A p_{bs} t \,, \tag{D.3}$$

and the $x$-coordinate is given by

$$x(t) = \frac{1}{2} k A p_{bs} t^2 \,. \tag{D.4}$$

Since, we are looking at positive $t$, during back-shocking $y(x)$ can be expressed by

$$y(x) = \sqrt{\frac{2x}{kAp_{bs}}}\,. \tag{D.5}$$

Hence, the integral under the path-line during back-shocking is given by

$$\int_0^{x(t_{bs})} \sqrt{\frac{2x}{kAp_{bs}}}dx = \frac{1}{3}\sqrt{\frac{8Ap_{bs}}{k}}\left(x(t_{bs})\right)^{3/2} = \frac{1}{3}k\left(Ap_{bs}\right)^2 t_{bs}^3\,. \tag{D.6}$$

Here, the last equality arrives using equation (5.57), i.e.,

$$x(t_{bs}) = \frac{k}{2}Ap_{bs}t_{bs}^2\,. \tag{D.7}$$

When the pressure is reversed $x(\tau)$ is given by equation (5.59)

$$x(\tau) = x(t_{bs}) + \frac{kA}{2}\left(-p_{tmp}\tau^2 + 2p_{bs}t_{bs}\tau\right)\,. \tag{D.8}$$

Hence,

$$\frac{2}{kA}\left(x - x(t_{bs})\right) + p_{tmp}\tau^2 - 2p_{bs}t_{bs}\tau = 0\,. \tag{D.9}$$

Thus,

$$\tau(x) = \frac{2p_{bs}t_{bs} \pm \sqrt{\left(2p_{bs}t_{bs}\right)^2 - 4p_{tmp}\frac{2}{kA}\left(x - x(t_{bs})\right)}}{2p_{tmp}}\,. \tag{D.10}$$

Since $\tau(x(t_{bs})) = 0$ we have

$$\tau(x) = \frac{2p_{bs}t_{bs} - \sqrt{\left(2p_{bs}t_{bs}\right)^2 - 4p_{tmp}\frac{2}{kA}\left(x - x(t_{bs})\right)}}{2p_{tmp}}\,. \tag{D.11}$$

Inserting this into the equation for $y(\tau)$, equation (5.60), it follows that

$$\begin{aligned} y(x) &= Ap_{bs}t_{bs} - Ap_{tmp}\left(\frac{2p_{bs}t_{bs} - \sqrt{\left(2p_{bs}t_{bs}\right)^2 - 4p_{tmp}\frac{2}{kA}\left(x - x(t_{bs})\right)}}{2p_{tmp}}\right) \\ &= \frac{A}{2}\sqrt{\left(2p_{bs}t_{bs}\right)^2 - 4p_{tmp}\frac{2}{kA}\left(x - x(t_{bs})\right)} = \frac{A}{2}\sqrt{\alpha - \beta x} \end{aligned} \tag{D.12}$$

Hence,

$$\int_{x(t_{bs})}^{L_m} y(x)dx = \int_{x(t_{bs})_m^L} \frac{A}{2}\sqrt{\alpha - \beta x}dx \tag{D.13}$$

$$= -\frac{A}{3\beta}\left(\alpha - \beta x\right)^{3/2}\,|_{x(t_{bs})}^{L_m}\,. \tag{D.14}$$

From equation (D.12) it is clear that

$$\alpha - \beta x(t_{bs}) = (2p_{bs}t_{bs})^2 \,. \tag{D.15}$$

In order to evaluate the other limit we use equation (5.64)

$$L_m = \frac{k}{2} A p_{bs} \left(1 + \frac{p_{bs}}{p_{tmp}}\right) t_{bs}^2 \,, \tag{D.16}$$

Inserting the expression from equation (D.7) and equation (D.16) into D.12 we have

$$\begin{aligned}
\alpha - \beta L_m &= (2p_{bs}t_{bs})^2 - 4p_{tmp}\frac{2}{kA}\left(L_m - x(t_{bs})\right) \\
&= (2p_{bs}t_{bs})^2 - 4p_{tmp}\frac{2}{kA}\left(\frac{k}{2}Ap_{bs}\left(1 + \frac{p_{bs}}{p_{tmp}}\right)t_{bs}^2 - \frac{k}{2}Ap_{bs}t_{bs}^2\right) \\
&= (2p_{bs}t_{bs})^2 - 4p_{bs}^2 t_{bs}^2 = 0 \,.
\end{aligned} \tag{D.17}$$

Inserting the values in the limit into equation (D.14) we have

$$\int_{x(t_{bs})}^{L_m} y(x)dx = \frac{A}{3}\frac{kA}{8p_{tmp}}(2p_{bs}t_{bs})^3 = \frac{k}{3}\frac{p_{bs}}{p_{tmp}}\left(Ap_{bs}\right)^2 t_{bs}^3 \,. \tag{D.18}$$

We can now evaluate $\phi_g$

$$\begin{aligned}
\phi_g = \int_0^{L_m} y(x)dx &= \int_0^{x(t_{bs})} y(x)dx + \int_{x(t_{bs})}^{L_m} y(x)dx \\
&= \frac{1}{3}k\left(1 + \frac{p_{bs}}{p_{tmp}}\right)\left(Ap_{bs}\right)^2 t_{bs}^3 \,.
\end{aligned} \tag{D.19}$$

Using equation (D.16) $\phi_g$ can be written as

$$\phi_g = \frac{2}{3} L_m A p_{bs} t_{bs} \,. \tag{D.20}$$

This means that the ratio between the gain and the loss is given

$$\frac{\phi_g}{\phi_l} = \frac{2}{3} \tag{D.21}$$

That this is the highest ration that can be achieved can be deduced by the following two geometric arguments.

The ratio presented in this section is essentially the the ration between the area under the path-line from $(0,0)$ to $(\tilde{L}_m, 0)$ and the area of the square $y(t_{bs})L_m$. In this section we have solved for $\tilde{L}_m = L_m$.

In the case where the back-shock time is shorter than the time given in equation (5.64), then $\tilde{L}_m < L_m$ Hence, the area under this path-line will be $\frac{2}{3}\tilde{L}_m A p_{bs} t_{bs}$. The loss, however, will still be $L_m A p_{bs} t_{bs}$. Thus, the ratio decreases.

In the case of back-shock times longer than the one presented here. The loss will increase increasing the gain. This is because no gain will be achieved for path-lines that hit the membrane at $\tilde{L}_m > L_m$.

Hence, one can conclude that

$$\frac{\phi_g}{\phi_l} \leq \frac{2}{3}, \tag{D.22}$$

for all values of the back-shock time.

# Bibliography


[1] A.L. Ahmad, M.F. Chong, and S. Bhatia. Mathematical modeling and simulation of the multiple solutes system for nanofiltration process. *Journal of Membrane Science*, 253(1-2):103 – 115, 2005.

[2] Eleftheria Antoniou and Marina Tsianou. Solution properties of dextran in water and in formamide. *Journal of Applied Polymer Science*, 125(3):1681–1692, 2012.

[3] J.K. Armstrong, R.B. Wenby, H.J. Meiselman, and T.C. Fisher. The hydrodynamic radii of macromolecules and their effect on red blood cell aggregation. *Biophysical Journal*, 87(6):4259 – 4270, 2004.

[4] Richard J. Bearman. On the linear phenomenological equations. *The Journal of Chemical Physics*, 28(4):662–664, 1958.

[5] Richard J. Bearman. On the linear phenomenological equations. ii. the linear statistical mechanical theory. *The Journal of Chemical Physics*, 31(3):751–755, 1959.

[6] Richard J. Bearman and John G. Kirkwood. Statistical mechanics of transport processes. xi. equations of transport in multicomponent systems. *The Journal of Chemical Physics*, 28(1):136–145, 1958.

[7] R. BEN AMAR, B.B. GUPTA, and M.Y. JAFFRIN. Apple juice clarification using mineral membranes: Fouling control by backwashing and pulsating flow. *Journal of Food Science*, 55(6):1620–1625, 1990.

[8] R. Byron Bird, Robert C. Armstrong, and Ole Hassager. *Dynamics of Polymeric Liquids*. John Wiley & Sons, 1977.

[9] W. Richard Bowen and Julian S. Welfoot. Predictive modelling of nanofiltration: membrane specification and process optimisation. *Desalination*, 147(1-3):197 – 203, 2002.

[10] Martin Braun. *Differential Equations and Their Applications, Fourth Edition*. Springer, 1993.

[11] J. Cakl, I. Bauer, P. Dolecek, and P. Mikulásek. Effects of backflushing conditions on permeate flux in membrane crossflow microfiltration of oil emulsion. *Desalination*, 127(2):189 – 198, 2000.

[12] Petr Dolecek. Mathematical modelling of permeate flow in multichannel ceramic membrane. *Journal of Membrane Science*, 100(2):111 – 119, 1995.

[13] C. Elata. The determination of the intrinsic characteristics of reverse osmosis membranes. *Desalination*, 6(1):1 – 12, 1969.

[14] Lawrence C Evans. Partial differential equations. graduate studies in mathematics. *American mathematical society*, 2, 1998.

[15] William Eykamp. Microfiltration and ultrafiltration. *Membrane Science and Technology*, 2:1–43, 1995.

[16] Eva M. Fahner, Georg H. Grossmann, and Klaus H. Ebert. Elastic and quasielastic light scattering studies on the branching characteristics of dextrans. *Die Makromolekulare Chemie*, 185(10):2205–2212, 1984.

[17] Elzbieta Gabrus and Daniela Szaniawska. Application of backflushing for fouling reduction during microfiltration of yeast suspensions. *Desalination*, 240(1-3):46 – 53, 2009. The Third Membrane Science and Technology Conference of Visegrad Countries (PERMEA); part 1, The Third Membrane Science and Technology Conference of Visegrad Countries (PERMEA).

[18] Kirsti A. Granath and Berit E. Kvist. Molecular weight distribution analysis by gel chromatography on sephadex. *Journal of Chromatography A*, 28(0):69 – 81, 1967.

[19] Etienne Guyon, Jean-Pierre Hulin, Luc Petit, and Catalin D. Mitescu. *Physical Hydrodynamics*. Oxford University Press, 2010.

[20] SC Hargrove, H Parthasarathy, and Shamsuddin Ilias. Flux enhancement in cross-flow membrane filtration by flow reversal: A case study on ultrafiltration of bsa. *Separation science and technology*, 38(12-13):3133–3144, 2003.

[21] W.C.M. Henkens and J.A.M. Smit. Salt rejection and flux in reverse osmosis with compactible membranes. *Desalination*, 28(1):65 – 85, 1979.

[22] Kuo-Jen Hwang and Tsung-Ting Lin. Effect of morphology of polymeric membrane on the performance of cross-flow microfiltration. *Journal of Membrane Science*, 199(1-2):41 – 52, 2002.

[23] Catalina E. Ioan, Thomas Aberle, and Walther Burchard. Structure properties of dextran. 2. dilute solution. *Macromolecules*, 33(15):5730–5739, 2000.

[24] J. Jagur-Grodzinski and O. Kedem. Transport coefficients and salt rejection in unchanged hyperfiltration membranes. *Desalination*, 1(4):327 – 341, 1966.

[25] Semant Jain and Sharad K. Gupta. Analysis of modified surface force pore flow model with concentration polarization and comparison with spiegler-kedem model in reverse osmosis systems. *Journal of Membrane Science*, 232(1-2):45 – 62, 2004.

[26] G. Jonsson. Overview of theories for water and solute transport in9 uf/ro membranes. *Desalination*, 35(0):21 – 38, 1980.

[27] G. Jonsson. Boundary layer phenomena during ultrafiltration of dextran and whey protein solutions. *Desalination*, 51(1):61 – 77, 1984.

[28] G. Jonsson and C.E. Boesen. Water and solute transport through cellulose acetate reverse osmosis membranes. *Desalination*, 17(2):145 – 165, 1975.

[29] O. Kedem and A. Katchalsky. A Physical Interpretation of the Phenomenological Coefficients of Membrane Permeability. *The Journal of General Physiology*, 45(1):143–179, 1961.

[30] BS Kim and HN Chang. Effects of periodic backflushing on ultrafiltration performance. *Bioseparation*, 2(1):23, 1991.

[31] Hyun-Gi Kim, Chulhwan Park, Jeongmok Yang, Byunghwan Lee, Sung-Soo Kim, and Sangyong Kim. Optimization of backflushing conditions for ceramic ultrafiltration membrane of disperse dye solutions. *Desalination*, 202(1-3):150–155, 2007. Wastewater Reclamation and Reuse for Sustainability.

[32] Vinod Kuberkar, Piotr Czekaj, and Robert Davis. Flux enhancement for membrane filtration of bacterial suspensions using high-frequency backpulsing. *Biotechnology and bioengineering*, 60(1):77–87, 1998.

[33] Niina Laitinen, Antero Luonsi, Erkki Levänen, and Marianne Nyström. Effect of backflushing conditions on ultrafiltration of board industry wastewaters with ceramic membranes. *Separation and purification technology*, 25(1):323–331, 2001.

[34] L.D. Landau and E.M. Lifshitz. *Course of Theoretical Physics Volume 6, Fluid Mechanics 2nd Edition.* ©Reed Educational and Professional Publishing Ltd., 1998.

[35] L.D. Landau and E.M. Lifshitz. *Course of Theoretical Physics Volume 5, Statistical Physics 3rd Edition Part 1.* Copyright ©1980, Elsevier Ltd, 2008.

[36] Laurent Lebrun and Guy-Alain Junter. Diffusion of dextran through microporous membrane filters. *Journal of Membrane Science*, 88(2-3):253 – 261, 1994.

[37] Takeshl Matsuura and S. Sourlrajan. Reverse osmosis transport through capillary pores under the influence of surface forces. *Ind. Eng. Chem. Process Des. Dev.*, 20:273–282, 1981.

[38] DS McLachlan, D Koen, and RD Sanderson. Flux flow and cleaning enhancement in a spiral membrane element, using continuous infrasonic backpulsing. *Water SA*, 36(4):0–0, 2010.

[39] H. Mehdizadeh and J.M. Dickson. Theoretical modification of the surface force-pore flow model for reverse osmosis transport. *Journal of Membrane Science*, 42(1-2):119 – 145, 1989.

[40] Wendy D Mores, Christopher N Bowman, and Robert H Davis. Theoretical and experimental flux maximization by optimization of backpulsing. *Journal of Membrane Science*, 165(2):225–236, 2000.

[41] Wendy D Mores and Robert H Davis. Direct observation of membrane cleaning via rapid backpulsing. *Desalination*, 146(1):135–140, 2002.

[42] Wendy D Mores and Robert H Davis. Yeast foulant removal by backpulses in crossflow microfiltration. *Journal of membrane science*, 208(1):389–404, 2002.

[43] Wendy D Mores and Robert H Davis. Yeast-fouling effects in cross-flow microfiltration with periodic reverse filtration. *Industrial & engineering chemistry research*, 42(1):130–139, 2003.

[44] N Mugnier, JA Howell, and M Ruf. Optimisation of a back-flush sequence for zeolite microfiltration. *Journal of Membrane Science*, 175(2):149–161, 2000.

[45] Marcel Mulder. *Basic Principles of Membrane Technology.* Kluwer Academic Puplishers, 2003.

[46] M.H.V. Mulder. Chapter 2 polarization phenomena and membrane fouling. In Richard D. Noble and S. Alexander Stern, editors, *Membrane Separations Technology Principles and Applications*, volume 2 of *Membrane Science and Technology*, pages 45 – 84. Elsevier, 1995.

[47] Pharmacosmos. Physical properties of dextran. `http://dextran.net/dextran-physical-properties.html`, 2013. [Online; accessed 19-March-2013].

[48] Barry N. Preston, Wayne D. Comper, Anthony E. Hughes, Ian Snook, and William van Megen. Diffusion of dextran at intermediate concentrations. *J. Chem. Soc., Faraday Trans. 1*, 78:1209–1221, 1982.

[49] Guy Ramon, Yehuda Agnon, and Carlos Dosoretz. Dynamics of an osmotic backwash cycle. *Journal of Membrane Science*, 364(1):157–166, 2010.

[50] Sanjeev Redkar, Vinod Kuberkar, and Robert H Davis. Modeling of concentration polarization and depolarization with high-frequency backpulsing. *Journal of membrane science*, 121(2):229–242, 1996.

[51] Sanjeev G Redkar and Robert H Davis. Cross-flow microfiltration with high-frequency reverse filtration. *AIChE journal*, 41(3):501–508, 1995.

[52] VGJ Rodgers and RE Sparks. Effect of transmembrane pressure pulsing on concentration polarization. *Journal of membrane science*, 68(1):149–168, 1992.

[53] E. Rotureau, E. Dellacherie, and A. Durand. Viscosity of aqueous solutions of polysaccharides and hydrophobically modified polysaccharides: Application of fedors equation. *European Polymer Journal*, 42(5):1086 – 1092, 2006.

[54] Annarita Salladini, Marina Prisciandaro, and Diego Barba. Ultrafiltration of biologically treated wastewater by using backflushing. *Desalination*, 207(1-3):24 – 34, 2007.

[55] Mohammad N. Sarbolouki and Irving F. Miller. On pore flow models for reverse osmosis desalination. *Desalination*, 12(3):343 – 359, 1973.

[56] R Sondhi, Y.S Lin, and F Alvarez. Crossflow filtration of chromium hydroxide suspension by ceramic membranes: fouling and its minimization by backpulsing. *Journal of Membrane Science*, 174(1):111 – 122, 2000.

[57] Rishi Sondhi and Ramesh Bhave. Role of backpulsing in fouling minimization in crossflow filtration with ceramic membranes. *Journal of Membrane Science*, 186(1):41–52, 2001.

[58] K.S. Spiegler and O. Kedem. Thermodynamics of hyperfiltration (reverse osmosis): criteria for efficient membranes. *Desalination*, 1(4):311 – 326, 1966.

[59] P Srijaroonrat, E Julien, and Y Aurelle. Unstable secondary oil/water emulsion treatment using ultrafiltration: fouling control by backflushing. *Journal of Membrane Science*, 159(1-2):11–20, 1999.

[60] Charles Tanford. *Physical Chemistry of Macromolecules*. Copyright ©1961 John Wiley & Sons, Inc., 1967.

[61] Shih-Chieh Tu, Varadarajan Ravindran, and Massoud Pirbazari. A pore diffusion transport model for forecasting the performance of membrane processes. *Journal of Membrane Science*, 265(1-2):29 – 50, 2005.

[62] GB Van den Berg and CA Smolders. Flux decline in ultrafiltration processes. *Desalination*, 77:101–133, 1990.

[63] J. G. Wijmans and R. W. Baker. The solution-diffusion model: a review. *Journal of Membrane Science*, 107(1-2):1 – 21, 1995.

[64] Mehdi Yazdanshenas, Mohammad Soltanieh, Seyyed Ali Reza Tabatabaei Nejad, and Luc Fillaudeau. Cross-flow microfiltration of rough non-alcoholic beer and diluted malt extract with tubular ceramic membranes: Investigation of fouling mechanisms. *Journal of Membrane Science*, 362(1-2):306 – 316, 2010.

[65] H. M. Yeh and C. H. Chen. Solvent extraction in cross-flow multipass parallel-plate membrane modules of fixed configuration. *Journal of Membrane Science*, 194(2):197 – 206, 2001.